

© 2016 Jorge E. San Juan Blanco.

RADIAL AND TANGENTIAL VELOCITY PROFILES IN AN ANNULAR FLUME
WITH GRANULAR BED

BY

JORGE E. SAN JUAN BLANCO

THESIS

Submitted in partial fulfillment of the requirements
for the degree of Master of Science in Environmental Engineering in Civil Engineering
in the Graduate College of the
University of Illinois at Urbana-Champaign, 2016

Urbana, Illinois

Adviser:

Professor Marcelo H. García

Abstract

Annular flumes become convenient facilities to produce undisturbed flows to study eco-hydraulic and cohesive sediment transport, among others. These flumes are ring-shape channels that produce curved flow by rotating their lid and/or tank. Thus, momentum in the tangential direction is transferred along the water column by the lid rotation. Because of the circular motion, centrifugal acceleration makes the flow helical rather than tangential and unidirectional. The objective of this work was to assess the applicability of the Engelund's formulation (Engelund, 1975) on the Ven Te Chow Annular Flume at the University of Illinois Urbana-Champaign. In order to accomplish this goal, tangential and radial velocity profiles were measured under three flow depths and five lid rotation conditions using Ultrasound Velocity Profiler (UVP-DUO). Later, they were contrasted with those computed using the Engelund's formulation. Despite some similarities of the measured tangential profile with the one computed using the Engelund's formulation, it was found that the formulation is not suitable for the Ven Te Chow Annular Flume. The strong curvature of the flume and the large depth-to-width ratio played a major role on defining the interaction of the secondary flow with the tangential velocity profile.

A Mónica y las meninas.

Acknowledgments

This work would not have been possible without the support of many people in Colombia, Puerto Rico, and Urbana-Champaign. I would like to say thank you to my adviser, Prof. Marcelo Garcia, for his support through this journey and giving me the opportunity to pursue this goal at UIUC. I would also would like to say thanks to all the staff and grad students at the Ven Te Chow Hydrosystem Laboratory. Esteban Lacunza, Oswaldo Torres, and Roberto Takahashi were valuable friends and officemates along this process. An special acknowledgment for David Waterman because of sharing some ideas and material regarding secondary flow in curved flows. Also thanks to many others for making this lab a nice place to work.

Besides all the academic support, much of this work was possible thanks to the support of my family. Thanks to Mónica, my daily motivation and example, for her unconditional help day and night. Also thank you to Mom, Mague, Vangie, and all the family in Colombia and Puerto Rico that followed my journey through this Master and stayed close besides the distance.

Table of Contents

List of Tables	vii
List of Figures	viii
List of Symbols	x
Chapter 1 Introduction	1
Chapter 2 Literature Revision and Theoretical Framework	5
2.1 Introduction	5
2.2 Annular Flume	6
2.2.1 Description	7
2.2.2 Advantages and Disadvantages	10
2.2.3 Previous Studies	13
2.3 Couette Flow	24
2.3.1 Basics of 2D planar Couette flow	25
2.3.2 Basics of 3D polar Couette flow	30
2.4 Summary	32
Chapter 3 Laboratory Experiments: Materials and Methodology	35
3.1 Introduction	35
3.2 The Annular Flume	36
3.3 The Ultrasound Velocity Profiler	38
3.3.1 Physics of an Ultrasound Velocity Profiler: Doppler Effect	39
3.3.2 Hardware and Software Description of the Ultrasound Velocity Profiler	46
3.3.3 Computation of Velocity Profile	49
3.4 Experimental Setup	55
3.5 Data Processing and Analysis	58
3.5.1 Processing of raw data	59
3.5.2 Englund's Formulation	62
Chapter 4 Results and Discussions	65
4.1 Introduction	65
4.2 Tangential Velocity Distribution	66
4.2.1 Measured Data	66

4.2.2	Engelund's formulation	73
4.3	Radial Velocity Distribution	83
4.3.1	Measured Data	83
4.3.2	Engelund's formulation	87
Chapter 5	Final Remarks	90
References	94

List of Tables

2.1	Summary of annular flumes used in: experimental and in situ work.	9
3.1	Evaluated cases in the annular flume at Ven Te Chow Hydrosystem Laboratory.	58
4.1	Shear velocity from measured data, Engelund's formulation, and adjusted by minimum squared error.	81

List of Figures

2.1	Sketch of an annular flume.	8
2.2	Secondary cells formed by only lid rotation and both lid and tank rotation. .	8
2.3	Dimensionless velocity distributions according to Engelund (1975).	23
2.4	Dimensionless radial velocity for several bed roughness according to Falcon (1979).	24
2.5	2D planar Couette flow.	26
2.6	Three-dimensional Couette flow.	30
3.1	Annular flume at the Ven Te Chow Hydrosystem Laboratory.	37
3.2	Schematic illustration of an UVP system.	39
3.3	Wavelength of a monochromatic wave.	40
3.4	Doppler effect as result of moving observer or wave source.	41
3.5	Sketch of a traveling ultrasound signal and its echo after it hits a moving particle.	44
3.6	Main components of a transducer.	48
3.7	Measurement window along a ultrasound beam.	50
3.8	Illustraion of a pulse (several cycles) passing through a channel (measuring volume).	50
3.9	Illustration of a UVP-DUO system measuring velocity profiles in an open channel flow.	55
3.10	Ensemble of the UVP holder into the lid and transducer arrangements for measureing radial and tangential velocity profiles.	56
3.11	Sketch of the experimental setup.	57
3.12	Velocity decomposition of moving transducer for tangential velocity measurements.	61
4.1	Mean tangential velocity profiles for flow depth $h = 5cm$	67
4.2	Shear velocity variation as function of lid rotation velocity for $h = 5cm$. . .	68
4.3	Depth-averaged mean velocity variation as function of lid rotation velocity for $h = 5cm$	69
4.4	Mean tangential velocity profiles for flow depth $h = 10cm$	70
4.5	Shear velocity variation as function of lid rotation velocity for $h = 10cm$. . .	71
4.6	Depth-averaged mean velocity variation as function of lid rotation velocity for $h = 10cm$	71
4.7	Mean tangential velocity profiles for flow depth $h = 15cm$	73
4.8	Shear velocity variation as function of lid rotation velocity for $h = 15cm$. . .	74

4.9	Depth-averaged mean velocity variation as function of lid rotation velocity for $h = 15cm$	74
4.10	Summary of hydraulic parameters of tangential velocity profiles as function of lid rotation for all flow depths.	75
4.11	Shear velocity u_* estimated from data (log-law distribution) and according to Engelund (1975) formulation.	76
4.12	Modeled and measured tangential velocity profiles for all flow conditions. Cases (flow depth) were organized by columns and lid rotation velocity were 0.5, 1, 2, 3, and 4rpm from top to bottom.	80
4.13	Measured data along with tangential velocity profiles using Engelund's formulation and adjusted shear velocity $h = 5cm$	82
4.14	Mean radial velocity profiles for flow depth $h = 5cm$	84
4.15	Mean radial velocity profiles for flow depth $h = 10cm$	86
4.16	Mean radial velocity profiles for flow depth $h = 15cm$	88
4.17	Modeled and measured radial velocity profiles for all flow conditions. Cases (flow depth) were organized by columns and lid rotation velocity were 0.5, 1, 2, 3, and 4rpm from top to bottom.	89

List of Symbols

r	Radial coordinate.
z	Vertical coordinate (elevation).
E_c	Specific kinetic energy.
A	Cross-sectional area.
v_θ	Tangential velocity component.
v_r	Radial velocity component.
v_z	Vertical velocity component.
R_{KE}	Ratio of secondary flow kinetic energy to kinetic energy of the tangential flow.
R_V	Ratio of maximum secondary flow velocity to the maximum tangential velocity.
M	Torque on a wall of the flume.
s	Longitudinal location along a wall of the flume.
τ	Shear stress.
τ_w	Shear stress at a wall of the flume.
τ_b	Tangential bed shear stress.
τ_r	Radial bed shear stress.
D	Water depth.
B	Flume width.
R_{in}	Inner radius of the annular flume.
R_{out}	Outer radius of the annular flume.
R	Mean radius of the annular flume.

ω_B	Bottom (tank) rotation speed.
Ω_T	Angular velocity of the top (lid).
c_t	Empirical constant of Booij (1994) formulation to compute bed shear stress.
h	Piezometric level.
ρ	Fluid density.
ϵ	Scalar eddy viscosity.
g	Gravitational acceleration.
κ	Von Karman constant.
u_*	Shear velocity.
ζ	Dimensionless vertical coordinate (z/h).
k_B	Equivalent roughness height of the bottom (tank).
k_T	Equivalent roughness height of the top (lid).
n	Exponent of the power-law velocity distribution.
f	Darcy-Weisbach friction factor.
u	Streamwise component of velocity in rectangular coordinates.
v	Lateral component of velocity in rectangular coordinates.
w	Vertical component of velocity in rectangular coordinate system.
x	Coordinate in the streamwise direction in rectangular coordinate system.
y	Coordinate in the lateral direction in rectangular coordinate system.
z	Coordinate in the vertical direction in rectangular and polar coordinate systems.
g_x	Streamwise component of gravitational acceleration.
g_y	Lateral component of gravitational acceleration.
g_z	Vertical component of gravitational acceleration.
v_s	Velocity of sound source
v_o	Velocity of observer
λ	Wavelength
v	Speed of sound

v'	Relative velocity between the wave and the observer or source.
f	Wave frequency
f'	Apparent wave frequency perceived by an observer when sound source or observer are moving.
T	Wave period
t_d	Delay time between sending an ultrasound signal and receiving its echo
x_p	Distance between transducer and moving particle
v_p	Velocity of moving particle
v_t	Velocity of moving transducer
Δf	Doppler shift
w_{ch}	Measure channel width of and ultrasound beam
d_{ch}	Channel distance
n_p	Number of cycles per pulse
W	Window distance
N_{ch}	Number of channels in a measuring window
W_{start}	Start position of the measuring window
W_{end}	End position of the measuring window
$W_{end\ max}$	Maximum end position of the measuring window
P_{max}	Maximum measurable depth
T_{prf}	Pulse repetition period
F_{prf}	Pulse repetition frequency
Δf_{max}	Maximum detectable Doppler shift frequency
V_{range}	Maximum velocity range
$v_{p\ max}$	Maximum measurable particle velocity
ΔV	Particle velocity resolution
N_{DU}	Number of possible velocity values for a 8-bit word digital signal processor
$C_{Doppler}$	Doppler coefficient
C_{sound}	Sound coefficient
V	Flow velocity component of interest

Chapter 1

Introduction

Reproducing natural environments in laboratory facilities is an effort-demanding task for scientists. For instance, experimental research on sediment transport and hydraulics has always to overcome space limitations. Both take place over a wide range of time and spatial scales. Bedload transport occurs over a significantly larger time scale than the downhill development of a turbidity current. Also, rivers can convey water and sediments along hundreds of miles. Even though scaling and similarity theory provide a tool to address this kind of limitations, researcher's experience plays a major role in choosing the right parameters to guarantee a correct physical representation. Therefore, scientists have developed laboratory flumes along with measuring instruments in order to reproduce natural processes in the laboratory under controlled conditions. Typical laboratory flumes are straight channels furnished with recirculating pumps. This is a convenient facility for open channel studies, where the focus might be hydraulic measurements and non-cohesive sediment transport. However, this kind of flumes become no longer suitable when the objective is to provide non-affected and infinite streams to study eco-hydraulics and cohesive sediment transport. Partheniades et al. (1966) developed the first annular flume in order to study deposition of cohesive sediments. It was a ring-shape flume that causes a flow by the rotation of its tank and/or lid. Thus, the water column is not disturbed by any recirculating pump. It provides a suitable environment to study cohesive sediment, bed erosion, sediment deposition, hydraulic of curved flows, and aquatic ecosystems.

The circular motion of the flume accelerates the mass of water in the radial direction (centrifugal acceleration) besides the tangential direction. Thus, it causes the flow to become

helical. Engelund (1975) and Falcon (1984) explained that the outward effect produced by the centrifugal acceleration is counterbalanced by means of the pressure gradient and the shear stress in the radial direction. The induced radial and vertical velocities constitute the so called secondary flow in curve flows. It can become undesired depending on the experiment purpose. For instance, secondary flow may affect settling velocity of suspended particles when the vertical component reduces the falling velocity. Thus, quite a bit of effort has been put on characterizing the secondary flow and calibrating the rotation of annular flumes to minimize its effect on erosion/deposition experiments. Experimental, numerical, and theoretical work have been published for a wide range of annular flume geometry since 1966.

The main objective of this work was to measure the radial and tangential velocity components in the annular flume of the Ven Te Chow Hydrosystem Laboratory and to compare them with the Engelund's formulation. It was intended to understand the hydraulic of this device and to study the validity of the Engelund's formulation on this facility. This flume is a 1.5-diameter flume that has been used for sediment erosion and deposition research as well as in transport of environmental substances. To accomplish this goal an Ultrasound Velocity Profiler (UVP-DUO) was used to measure the radial and tangential component of the flow under several flow conditions. The UVP-DUO system was manufactured by Metflow SA. It is capable of detecting the Doppler Shift Frequency along an ultrasound beam and correlating it with the flow velocity. The physical principle behind this instrument is the apparent change of frequency of a wave due to the relative motion of either an observer or the source. In order to measured the velocity profile, the system considers that particles in the fluid moves with the same velocity as the flow. Acoustic methods conveniently allow scientists to take measurements in dark flows such as oil or waste water. Even velocity measurements can be taken through rigid boundaries like tank walls or pipes.

This document is divided into four more chapters: a Literature Review, Materials and Methodology, Results and Discussion, and Final Remarks. The objective of the literature re-

view is to understand the most relevant aspects of the flow in annular flumes. The Literature Review will cover two aspects: (i) a revision of previous studies conducted in annular flumes such as experimental and theoretical work, and (ii) a revision of the governing equations for the flow in annular flumes, Couette flow. Also, a basic description of an annular flume is presented since it became the study object of this work. Limitations and advantages are shown as well in order to highlight capabilities of this flume. The Literature Review will go through the most important works conducted on understand the hydraulic of annular flumes. Most of them have been motivated by the need to calibrate the lid and tank rotation velocities in order to minimize the secondary flow and obtain an uniform shear stress distribution at the bottom. On the other hand, the theoretical studies have been focused on representing mathematically the secondary flow. Then, the basic 1D and 3D Couette flow is presented as a theoretical framework. Since the flow in annular flumes is brought by shearing at the top and/or bottom, it was found relevant to present the governing equations for this kind of flow. Through the Literature Review, the mathematical formulation used in this study was derived.

The Material and Methodology chapter will focus on describing the annular flume used in these experiments, the acoustic instrument used to measure the tangential and radial component of the flow, and the post-processing treatment of the measured data. The Ven Te Chow Annular Flume is a 1.5m ring-shape flume with a capacity of 370L. It consists on three major components, the tank ensemble, the lid ensemble, the frame structure. It was built in 2000 by *Engineering Laboratory Design, Inc.* Even though lid and tank can rotate in opposite directions, the tank was kept stationary. Flow conditions varied over lid rotation velocity of 0.5rpm to 4.0rpm and flow depth of 5.0cm to 15cm. Two transducers of 1MHz were attached to the lid to measured the tangential and radial components of the flow. Since the UVP-DUO is design to detect the Doppler Shift Frequency when the transducers are stationary, some post-processing computations were needed to obtain the correct velocity values. The Material and Methodology chapter finally presents the Engelund's formulation

as well as the methodology followed to compute the tangential and radial velocity profiles.

The Results and Discussion chapter will analyze the measured and computed tangential and radial velocity profiles. Its purpose was to analyze the measured data and compare them with the computed velocity profiles from Engelund's formulation. The chapter is organized in two sections: (i) the first one is devoted to analyze the measured and modeled tangential velocity profiles, and (ii) a second section will present the measured and computed velocity profiles in the radial direction. Thus, the validity of the formulation for the Ven Te Chow Annular Flume can be evaluated by contrasting the measured and modeled velocity profiles. A special effort was put on understanding flow behavior in this flume because shear velocity is an important parameter for sediment transport experiments and it becomes a sensitive factor in Engelund's formulation. Shear velocity was estimated following two methodologies, first it was determined by fitting a logarithmic profiles to the lower part of the tangential profile; then, it was computed by following Engelund's approach.

Chapter 2

Literature Revision and Theoretical Framework

2.1 Introduction

Dynamic of cohesive sediment becomes a fascinating field but still not very well understood. Flocculation is a natural process that defines much of the transport characteristics of cohesive sediments. It is the result of electro-chemical aggregation of fine-grained sediments in suspension. Therefore, setting experiments in recirculating flumes may be truly challenging; because pump blades would break up the flocs. It means that the flow must be induced by other ways but pumping. Motivated by studying deposition of cohesive sediments, a ring-shape flume was designed and built by Partheniades et al. (1966). The ring-shape or annular flume became a device where flow is caused by rotation of the flume itself. It provided a convenient experimental environment where the water column is not affected by recirculating pumps.

Because of the circular shape of the annular flume, its flow is subject to centrifugal acceleration. In consequence, the flow structure becomes helicoidal. The secondary currents generated by rotation of an annular flume has been identified as a problem for deposition and erosion experiments. Therefore, extensive studies have been conducted to characterize and calibrate the flume rotation in order to minimize the secondary flow effect. For instance, Booij (1994) presents an outstanding experimental work to characterize the flow in an annular flume. He studied the velocity field of an annular flume with a mean radius of $1.85m$ and proposed relationships for optimal flume rotation in terms of the flume geometry.

The purpose of this literature review is to understand the most relevant aspects of the flow

in an annular flume. This chapter is divided into three sections: a revision of previous studies conducted in annular flumes, a theoretical background about Couette flow, and a summary of the most important findings. The first section presents a description of an annular flume and goes through its capabilities and limitations. Thus, an analysis of advantages and disadvantages of usage of these flumes is covered in this section. Also, it contains a review of the experimental and theoretical studies conducted in other annular flumes. It includes the work related to the hydraulic characterization and calibration of these type of flumes. A theoretical framework of Couette flow is presented in the second section. Its purpose is to provide a theoretical background of the type of flow generated in an annular flume. First, the simple, laminar, planar 1D Couette flow is derived from the set of Navier-Stokes equations. In reality, the flow in annular flumes becomes considerable more complex than laminar, planar 1D flow. The helicoidal flow structure introduces an important distribution of radial and vertical velocities. Therefore, the 3D Couette flow is drawn in this section as well. Finally, a summary section presents the most important remarks found in the literature review. It will be concentrated on presenting the applicability of annular flumes and its hydraulic description. Because the major objective of this study was to measure the radial and tangential velocity profiles of an annular flume and to compare them with a mathematical description, the summary section will highlight such mathematical formulation.

2.2 Annular Flume

This section presents a basic description of an annular flume. Also, it discusses some advantages and disadvantages of this type of flumes and previous relevant works. Because an annular flume became the main prototype of this project, it is pertinent to point out the flume characteristics and mechanism that drive its flow. A literature revision of conducted studies in an annular flume may bring insights about the state-of-the-art of its hydrodynamic understanding. Furthermore, it will show actual limitations of annular flumes used

in previous works as well as recommended paths to better understand its flow structure. In a brief subsection, the main features of an annular flume will be introduced. A second subsection will be devoted to present advantages and disadvantages of annular flumes. Finally, a discussion of some experimental and theoretical work conducted in this kind of flumes is presented.

2.2.1 Description

An annular flume is a circular device designed to reproduce a three dimensional Couette flow by rotation of its lid (see fig. 2.1). Thus, the lid shears the fluid underneath and transfers tangential momentum into the vertical direction. This characteristic makes the annular flume an ideal setup to study erosion, deposition, and transport of cohesive sediments. It was initially proposed and built by Partheniades et al. (1966) to study depositional behavior of cohesive sediments. Some other studies have used annular flumes for in situ measurements (e.g., Amos et al., 1992b, 1992a; Maa et al., 1993; Widdows et al., 1998b, 1998a; Amos et al., 2004) and laboratory experiments (e.g., Tait et al., 2003; Cloutier et al., 2006; Neumeier et al., 2006; Cofalla et al., 2010; Yunwei et al., 2011; Cofalla et al., 2012; Huang et al., 2012a, 2012b). Due to the circular shape and rotating operation, the fluid is subject to centrifugal acceleration. Such acceleration is not uniformly distributed along the transversal direction of the cross section because tangential velocity varies with the r - and z -location. Tangential velocity increases outwards and decreases downwards (in case of fixed bottom). Engelund (1975) explains that this gradient of acceleration causes the flow in the annular flume to be helical. Also, such secondary flow will generate some radial shear stress distribution in order to compensate the difference between the pressure gradient and acceleration gradient.

To overcome any undesirable secondary flow, some studies have allowed the tank (bottom and walls) of the annular flume to rotate independently in the opposite direction of the lid. According to Partheniades and Mehta (1971), the secondary current produced by the lid is canceled out by a new secondary cell generated by the tank rotation (see fig. 2.1 and 2.2).

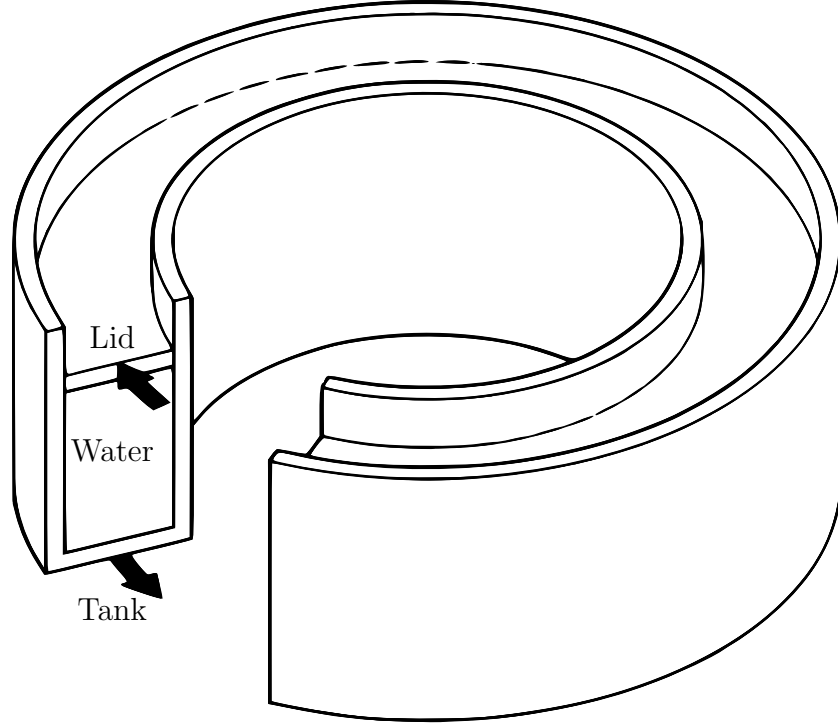


Figure 2.1: Sketch of an annular flume.

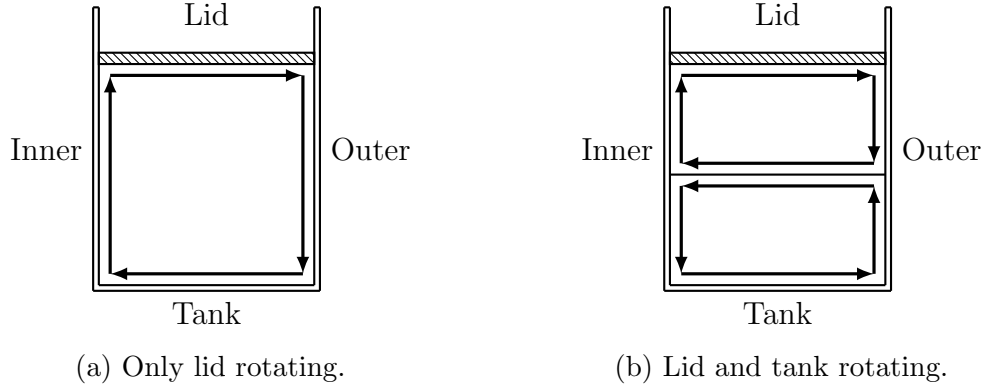


Figure 2.2: Secondary cells formed by only lid rotation and both lid and tank rotation.

Therefore, studies have been concentrated to find the optimal combination of lid and tank rotation in order to minimize the secondary flow and/or obtain an uniform distribution of tangential bed shear stress (e.g., Booij et al., 1993; Krishnappan, 1993; Petersen & Krishnappan, 1994; Cantero et al., 2004; Te Slaa, 2012). However, note that conveniently annular flumes may also provide a suitable prototype of curved flows (e.g. river bends). It may be

argued that helicoidal flow structure would represent the hydrodynamic behavior of curved channels. Accordingly, annular flumes with mobile beds have been used to study scour formation, large-scale bedforms and flow structure of curved streams (Gibson & Cook, 1974; Engelund, 1975; Falcon, 1979; Corney et al., 2006). To summarize some annular flumes used worldwide, table 2.1 shows the geometry and rotation characteristics of some relevant studies with annular flumes; where R_{in} is inner radius, R_{out} outer radius, W is width, and D is depth.

Table 2.1: Summary of annular flumes used in: experimental and in situ work.

Ref.	R_{in} [m]	R_{out} [m]	W [m]	D [m]	Lid	Tank	Location
Partheniades et al. (1966); Partheniades and Mehta (1971)	0.36	0.46	0.10	0.31	Rotate	Rotate	Massachusetts Institute of Technology (USA)
Kuenen (1966)	0.43	0.60	0.17	0.30	Rotate	Fixed	University of Groningen (Netherlands)
Kato and Phillips (1969); Kantha et al. (1977)	0.53	0.76	0.23	0.28	Rotate	Rotate	The John Hopkins University (USA)
Engelund (1975)	0.80	1.00	0.20	0.05	Rotate	Fixed	Technical University of Denmark (Denmark)
Mehta and Partheniades (1982)	0.65	0.85	0.21	0.46	Rotate	Rotate	University of Florida (USA)
Amos et al. (1992b, 1992a, 2004)	0.93	1.07	0.15	0.30	Rotate	Fixed	Geological Survey of Canada (Canada)
Graham et al. (1992)	2.60	3.00	0.40	0.35	Rotate	Fixed	University of Plymouth (UK)
Booij et al. (1993); Booij (1994)	1.70	2.00	0.30	0.47	Rotate	Rotate	Delft University of Technology (Netherlands)

Table 2.1 Continued: Summary of annular flumes used in: experimental and in situ work

Ref.	R_{in} [m]	R_{out} [m]	W [m]	D [m]	Lid	Tank	Location
Krishnappan (1993); Petersen and Krishnappan (1994); Krishnappan and Engel (2004)	2.35	2.65	0.30	0.30	Rotate	Rotate	National Water Research Institute (Canada)
Yang et al. (2000)	0.46	0.88	0.42	0.40	Rotate	Rotate	Center of Coastal Land-Margin Research (USA)
Maa et al. (1993)	1.00	1.15	0.15	0.20	Rotate	Fixed	Virginia Institute of Marine Science (USA)
Briskin et al. (2002); Pedocchi (2005)	0.55	0.75	0.20	0.40	Rotate	Rotate	Ven Te Chow Hydrosystem Laboratory (USA)
Tait et al. (2003)	0.90	1.10	0.20	0.30	Rotate	Rotate	Delft University of Technology (Netherlands)
Cloutier et al. (2003, 2006)	0.85	1.00	0.15	0.45	Rotate	Fixed	Geological Survey of Canada (Canada)
Neumeier et al. (2006)	0.85	1.00	0.15	0.46	Rotate	Fixed	Southampton Oceanography Centre (UK)
Pope et al. (2006)	0.22	0.32	0.10	0.35	Rotate	Fixed	Plymouth Marine Laboratory (UK)
Cofalla et al. (2010, 2012)	1.50	1.75	0.25	0.18	Rotate	Rotate	Institute of Hydraulic Engineering and Water Resources Management (Germany)
Yunwei et al. (2011)	0.54	0.75	0.21	0.41	Rotate	Rotate	Nanjing University (China)
Huang et al. (2012b)	0.30	0.44	0.14	0.14	Rotate	Fixed	Chinese Academy of Science (China)

2.2.2 Advantages and Disadvantages

The objective of this subsection is to highlight some of the most relevant advantages and disadvantages of using annular flumes. Thus, some limitations and prospective future work might be identify through this analysis. Being aware of advantages and disadvantages of

annular flumes is important to motivate improvements on this device. Also, it might be an opportunity of explore new applications for annular flumes. The following list shows the most significant advantages and disadvantages of annular flumes found in literature:

1. Advantages:

- (a) It provides an ideally infinite flow with fully developed boundary layer.
- (b) Because the flow is driven by the moving lid (and/or moving tank), annular flumes do not experience flow entrance effects.
- (c) Unaffected flow by pump blades makes annular flumes ideal to study biogeochemical sediment-flow interaction.
- (d) In cohesive sediment studies, aggregate structures are only affected by flow dynamic, mainly by fluid stresses.
- (e) Bed shear stress is uniform in the tangential direction because of the ideal infinite flow condition.
- (f) Shear stress distribution in the vertical direction is uniform as well.

2. Disadvantages:

- (a) Unbalance between pressure gradient and centrifugal acceleration in the radial direction generate secondary currents.
- (b) In consequence, secondary currents produce uneven radial distribution of bed shear stress.
- (c) Vertical component of secondary currents affects the settling velocity; i.e. it may be significant in resuspension and deposition studies.

Taking into consideration the advantages and disadvantages of annular flumes, it may be argued that these flumes can be used to represent natural environments. Once the secondary

flow is minimized, annular flumes become a versatile device to reproduce straight and curved flows. For instance, curved channels become the most obvious application of annular flumes considering its ring-shape. On the other hand, unaffected flow by recirculation pumps allows researchers to establish temporal aquatic ecosystems in these devices. Even under stratified flow conditions (e.g. fresh and sea water), annular flumes have been used to study turbulence interaction at the interface between two stratified flows.

Annular flumes can be used to study curved flows like bends in meandering rivers. Straight channels are less common than meandering streams in nature. Then, annular flumes are suitable prototypes to study large-scale bedforms in curve flows and its instability (e.g., Gibson & Cook, 1974; Engelund, 1975). After calibration (lid and tank rotation speed), curved and helical flow might be generated over a wide range of flow velocity. Even though annular flumes are limited by having a single curvature radius, dimensional analysis and similarity theory can help researchers in understanding multiple conditions.

Once secondary currents are minimized, the hydraulic behavior of annular flumes may resemble that of flows in straight channels. Therefore, these flumes can reproduce natural streams adequately. For instance, in order to understand the hydro- and bio-dynamic of toxics under flow events, Cofalla et al. (2010) replicated an aquatic ecosystem in an annular flume. They studied the interaction between sediment, hydrodynamic, water quality, and aquatic organisms (fish). Since recirculation pumps are not needed, ideally infinite straight flows are reproducible only by lid/tank rotation; therefore, physical models of aquatic ecosystems are capable of being simulated in annular flumes. Note that even the behavior of contaminated sediments can be studied in this kind of facility because it provides a well controlled closed system.

Interaction of interface between stratified flows have been studied in annular flumes before. Kato and Phillips (1969) and Kantha et al. (1977) studied the behavior of turbulence at the interface of a stratified flow using an annular flume. Stratified flows are common in nature; they are characterized by sharp gradients of density between two fluids. Such

condition can be caused by salinity, temperature, or sediment concentration (M. H. Garcia, 1996). Because of the large density difference, they mix with each other at a considerable low rate; therefore, one fluid may flow practically independently of the other. Due to the advantage of no recirculation pump, interaction at the interface of stratified flows can be studied in annular flumes. Thus, sediment resuspension, deposition, and transport under stratified flow conditions seems to be a prospective research path for application of this device.

2.2.3 Previous Studies

This subsection presents a review of some relevant experimental and theoretical work conducted in annular flumes. Experimental work is related to the hydraulic characterization of annular flumes: flume calibration and bed shear stress. On the other hand, the theoretical work presents the theoretical development of Engelund (1975) for tangential and radial velocities in an annular flume. Additionally, this part is complemented with some annotations made by Falcon (1984) about secondary flows in a curved open channel.

Experimental Work

Since 1971, a quite large amount of effort have been put into experimentally characterizing the complex three-dimensional flow in annular flumes (e.g., Graham et al., 1992; Krishnappan, 1993; Booij et al., 1993; Booij, 1994; Petersen & Krishnappan, 1994; James et al., 1996; Yang et al., 2000; Krishnappan & Engel, 2004; Cantero et al., 2004; Pedocchi, 2005; Pope et al., 2006; Hillebrand & Olsen, 2010; Te Slaa, 2012). Some other work has been conducted on studying erosion, transport, and deposition of both cohesive and non-cohesive sediments using annular flumes (Kuenen, 1966; Partheniades et al., 1966; Kato & Phillips, 1969; Partheniades & Mehta, 1971; Kantha et al., 1977; Mehta & Partheniades, 1982; Villaret & Paulic, 1986; Sheng, 1989; Amos et al., 1992b; Tait et al., 2003; Cloutier et al., 2006; Neumeier et al., 2006; Yunwei et al., 2011). Even, bio-ecological studies have been carried

out in annular flumes as well (Widdows et al., 1998a, 1998b; Briskin et al., 2002; Cofalla et al., 2010, 2012; Huang et al., 2012a, 2012b).

Hydraulic characterization of the three-dimensional flow structure of annular flumes have been motivated by the need of minimizing the secondary flow and obtaining uniform distribution of bed shear stress at the bottom. By the optimal combination of lid and tank rotational speed, several studies have demonstrated that the two generated secondary cells may cancel each other out (e.g., Partheniades et al., 1966; Partheniades & Mehta, 1971; Krishnappan, 1993; Booij et al., 1993; Cantero et al., 2004; Te Slaa, 2012). With respect to the "optimal" lid-tank rotation, two positions were found in the literature. The first position considers that only one calibration curve is enough to minimize undesirable secondary flows and obtain uniform distribution of bed shear stress. Differently, other studies affirm that there must be two calibration curves depending on the experiment's purpose. For example, erosion experiments would required as much uniform bottom shear stress as possible; whilst, secondary flow have to be the minimized for deposition experiments. The later position suggests that both calibration curves, the one for erosion and the one for deposition studies, are not necessarily the same.

Studies, like those by Krishnappan (1993), Partheniades et al. (1966) and Petersen and Krishnappan (1994), assume that a unique calibration curve is enough to reproduce acceptable flow conditions to investigate cohesive sediments. They consider that once the tangential bed shear stress is uniformly distributed in the transversal direction any secondary current practically vanishes. Thus, two subjective and qualitative criteria came out. The first calibration criteria was proposed by Partheniades et al. (1966) and Partheniades and Mehta (1971). They argued that the minimum secondary flow and uniform distribution of bed shear stress is achieved when sediments deposit along the center line of the flume. Partheniades et al. (1966) noted that when the tank was stationary and the lid rotated, some plastic beads deposited along the inner wall of the tank. Contrary, when the lid was stationary and the tank rotated the beads deposited along the outer wall. Intuitively, they stated that

secondary flows are minimized when the plastic sediments deposit along the center line of the flume. Krishnappan (1993) also proposed a qualitative criteria to find a calibration curve. He measured the vertical distribution of tangential velocities and bed shear stress in the cross section using a Laser Doppler Velocimeter and a Preston tube. By subjective evaluation, this study found that the secondary flow is mitigated under conditions of significant uniform distribution of tangential bed shear stress. Petersen and Krishnappan (1994) suggested a method to quantify the intensity of the secondary current. They stated that a secondary current may be controlled by minimizing the specific kinematic energy over the cross-sectional area. Thus, Petersen and Krishnappan (1994) defined such specific energy as:

$$E_c = \frac{1}{A} \int_A (v_r^2 + v_z^2) dA \quad (2.1)$$

Where, E_c is the specific kinetic energy, A is cross-sectional area, v_r is the radial component of flow velocity, and v_z is the vertical component of flow velocity.

Cantero et al. (2004) presented a literature review where they highlighted the criteria used to calibrate annular flumes. They pointed out that the nature of the study in the flume will determine such criteria. Similar to Booij et al. (1993) and Spork et al. (1994), Cantero et al. (2004) stated that two calibration curves must be provided: one for bed erosion experiments and another for sediment deposition experiments. In both erosion or resuspension experiments, an attempt should be made to generate the most uniform distribution of bed shear stress. Thus, preferential scour would be avoided and erosion would be ideally uniform in the radial direction. On the other hand, secondary currents may affect the deposition behavior of sediments. For instance, settling velocity might be hindered when the vertical component of the secondary flow is strong enough to lower the fall velocity of particles. Booij et al. (1993) conducted velocity measurements using a Laser Doppler Velocimeter in an annular flume. He found that even under the optimal condition of lid-tank rotation, vertical component of secondary currents may equal the order-of-magnitude of silt

settling velocity. Yang et al. (2000) also agreed that two calibration curves are necessary. Thus, they proposed two criteria to determine the secondary flow strength: (i) the ratio of secondary flow kinetic energy to the kinetic energy of the tangential flow (see eq. 2.2a) and (ii) the ratio of the maximum secondary flow velocity to the maximum tangential velocity (see eq. 2.2b).

$$R_{KE} = \frac{\int_A (v_r^2 + v_z^2) dA}{\int_A v_\theta^2 dA} \quad (2.2a)$$

$$R_V = \frac{\max \left(\sqrt{v_r^2 + v_z^2} \right)}{\max (|v_\theta|)} \quad (2.2b)$$

Even though they stated that two calibration curves are needed to study erosion and deposition separately, no criteria has been proposed to determine the uniformity of shear velocity. Only Cantero et al. (2004) proposed two methods to estimate mean bed shear stress as function of the experiment nature (erosion or deposition).

Measuring shear stress applied by a fluid does not become an easy task in most cases. It was found in literature that some studies have focused on estimating numerically the bed shear stress and comparing it with laboratory measurements (e.g. Graham et al., 1992; Krishnappan & Engel, 2004). Preston tubes and hot-film probes have been used to measured directly local shear stress. Graham et al. (1992) numerically modeled the flow velocity field and shear stress in an annular flume using HARWELL-FLOW3D. Furthermore, they measured the bed and wall shear stress with hot-film probes. Indirect estimation of bed shear stress have been carried out as well. For example, Pope et al. (2006) evaluated the bed shear stress in an annular flume by means of the turbulent kinetic energy. In addition, they analyzed the advantages and disadvantages of using other indirect methods; such as law of the wall and Reynold stress methods.

It was notable that there is no unique definition for a characteristic mean bed shear stress in an annular flume. Bed shear stress have been defined in terms of the force applied by the lid/tank, as the surface-average of the shear stress variation along the physical boundaries,

and through empirical relationships. Graham et al. (1992) proposed a method to relate the shear stress and the eroded contours of the bed. They were interested on the shear stress at the bottom and walls of the flume; thus, they reported shear stress in terms of the torque impinged by the lid as follows:

$$M = 2\pi \int_{s=s_0}^{s=s_1} r^2 \tau_w(s) ds \quad (2.3)$$

where M is the torque on the wall of interest, τ_w is the tangential component of the wall shear stress, s is measured along the wall of interest, s_0 and s_1 are inside and outside (or top and bottom) boundaries of the wall, and r is the radial location. Following a similar approach, Cantero et al. (2004) found in their literature review that mean bed shear stress has been reported as the summation of the surface-averaged shear stress of bed and walls. For instance, Partheniades et al. (1966) defined the bed shear stress in an annular flume as:

$$\tau_b = \frac{1}{2D + B} \left[\int_0^D \tau_w(R_{in}, z) dz + \int_{R_{in}}^{R_{out}} \tau_w(r, 0) dr + \int_0^D \tau_w(R_{out}, z) dz \right] \quad (2.4)$$

where τ_b is bed shear stress, D is water depth, B is flume width, τ_w is shear stress as function of r and z , R_{in} is inner radius, and R_{out} is outer radius. On the other hand, Petersen and Krishnappan (1994) defined bed shear stress as:

$$\tau_b = \int_{R_{in}}^{R_{out}} \frac{3r^3}{R_{out}^3 - R_{in}^3} \tau_w(r, 0) dr \quad (2.5)$$

Finally, Cantero et al. (2004) proposed two criteria to compute bed shear stress according to the nature of the experiment. For erosion experiments, they stated that bed shear stress has to be represented by the average shear stress only at the bottom:

$$\tau_b = \int_{R_{in}}^{R_{out}} \frac{2r}{R_{out}^2 - R_{in}^2} \tau_w(r, 0) dr \quad (2.6)$$

Meanwhile, bed shear stress for deposition experiments has to consider the effect of the four walls:

$$\tau_b = \frac{1}{(R_{out} - R_{in})D + R_{out}^2 - R_{in}^2} \left[R_{in} \int_0^D \tau_w(R_{in}, z) dz + R_{out} \int_0^D \tau_w(R_{out}, z) dz + \int_{R_{in}}^{R_{out}} r \tau_w(r, 0) dr + \int_{R_{in}}^{R_{out}} r \tau_w(r, D) dr \right] \quad (2.7)$$

In an extensive experimental work, Booij (1994) proposed an empirical relationship to estimate bed shear stress once the optimal conditions are achieved.

$$\tau_b = 0.1 \left(\frac{1.64\omega_B + 3.89}{c_t} \right)^2 \quad (2.8)$$

where ω_B is the bottom (tank) rotation speed (*rpm*) and c_t is an empirical constant. Booij (1994) stated that c_t was equal to 25. Even though empirical formulations tend to be limited to a narrow range of conditions; this one turns out to be remarkable because it collapses the bottom shear stress into a single equation based on the optimal lid rotation. Later, Te Slaa (2012) published a technical report where they calibrated the average bed shear stress of a 0.35m-mean-radius annular flume. They followed most of the relationship developed by Booij (1994). Under the optimal lid to tank rotation combination, they estimated and calibrated the bed shear stress according to equation 2.8, Te Slaa (2012) found that $c_t = 8.42$. Using the Shields diagram and varying the mean grain size of the granular bed, Te Slaa (2012) could estimate an actual bed shear stress. Based on this experimental comparison, Te Slaa (2012) empirically modified equation 2.8 into:

$$\tau_b = 0.1 \left(\frac{1.64\omega_B + 3.88}{8.42} \right)^2 - 0.0183 \quad (2.9)$$

Bed roughness plays a major role in the magnitude of shear stress. Numerically and experimentally studies like Krishnappan and Engel (2004) and Pope et al. (2006) have investigated the effect of bed roughness on bed shear stress. Krishnappan and Engel (2004)

studied the bed shear stress in an annular flume numerical using the PHOENIC CFD software and experimentally with a Preston tube. They found two major differences on the bed shear stress behavior as function of the roughness. First, the flow was found to be two-dimensional at the center of the flume with a fairly well distributed tangential shear stress for smooth bed. On the other hand, bed shear stress was skewed toward the inner radius of the flume. Through numerical modeling, they found that the skewness in bed shear stress can be counteracted by increasing the lid roughness. They were interested on shear stress only at the bottom of the flume. Pope et al. (2006) found that there is a non-linear relationship between bed shear stress and current velocity for rough sediments. Contrary to rough beds, smooth sediment beds showed a linear relationship with the velocity gradient, "enabling estimation of bed shear stress from velocity alone". The objective of this study was to compare bed shear stress and erosion of identical sediments in situ and laboratory.

Theoretical Work

This part of the literature review is based on the theoretical work developed by Engelund (1975) and Falcon (1984) in secondary flow in curved channels. Specifically, it will present the derivation of radial and tangential velocity distribution proposed by Engelund (1975). Such derivation is relevant for this thesis because it was derived for an annular flume. Even though Falcon (1984) addressed curved flows under open channel conditions, he brought pertinent insights with regards to secondary flows. Finally, this part will conclude presenting the two mathematical formulations for radial and tangential vertical distribution of velocity.

In a technical review presented by Falcon (1984) in the Annular Review of Fluid Mechanics, he nicely explains how secondary flows are generated as consequence of the curvature of the main flow. Curved flows are subject of centrifugal accelerations, v_θ^2/r . In open channels, the streamwise flow velocity becomes zero and the maximum at the very bottom and near or at the surface, respectively. Therefore, at a fixed r -location the centrifugal force varies along the water depth. The case of an annular flume with fixed bottom is not much differ-

ent. Theoretically, the flow velocity is zero at the bottom and equals the lid rotation at the lid elevation. It implies that likely centrifugal acceleration will vary along the water depth for a certain radial location. By definition, the centrifugal acceleration will bring water towards the outer part of the curve. Falcon (1984) states that "therefore, a second principal radial force is due to the radial pressure gradient $\partial p/\partial r$ ". This phenomenon leads to the superelevation of the water surface for open channels. If the pressure is assumed to be hydrostatic, it will be constant for a certain r -location. It implies that the net radial force will be negative at a certain flow depth because the centrifugal acceleration is significant variable along the water depth while the radial pressure gradient remains constant. Falcon (1984) and Engelund (1975) agreed that the difference between v_θ^2/r and $\partial p/\partial r$ is balanced by the vertical gradient of radial shear-stress $\partial \tau_r/\partial z$ and the convective inertial force $\rho v_\theta \partial v_r/\partial \theta$.

Under steady-state conditions the flow in an annular flume becomes uniform in the tangential direction. Through a simplified radial dynamic equation, Engelund (1975) stated that the flow can be described in polar coordinates as follows:

$$\frac{\tau_b}{\rho} = \epsilon \frac{\partial v_\theta}{\partial z} \quad (2.10a)$$

$$-\frac{v_\theta^2}{r} = -\frac{\partial}{\partial r}(gh) + \frac{\partial}{\partial z}\left(\epsilon \frac{\partial v_r}{\partial z}\right) = -g\frac{\partial h}{\partial r} + \frac{\partial}{\partial z}\left(\frac{\tau_r}{\rho}\right) \quad (2.10b)$$

Where τ_b is bed shear stress, ρ is fluid density, ϵ is eddy viscosity, v_θ is tangential component of flow velocity, z is elevation, r is radial location, g is gravitational acceleration, h is piezometric level, v_r is radial component of flow velocity, and τ_r is the radial component of shear stress. Engelund (1975) explains that equation 2.10a implies that the bed shear stress is invariant along the water depth as it is transferred from the moving lid to the bottom. On the other hand, equation 2.10b expresses that the difference between the pressure gradient ($g\partial h/\partial r$) and the centrifugal acceleration (v_θ^2/r) is balanced by means of the radial component of shear stress. The aforementioned equations consider that $h/R \ll 1$ and $h/B \ll 1$.

Such conditions allowed Engelund (1975) and later Falcon (1979) to apply a log-law and power-law velocity distribution, respectively. Engelund (1975) did not assume a constant scalar eddy viscosity ϵ ; instead, he considered the Reichardt (1959) expression to define the eddy viscosity ϵ for a Couette flow as follows:

$$\epsilon = \kappa u_* z (1 - z/h) \quad (2.11)$$

Where κ is the Von Karman constant (0.40) and u_* is the shear velocity. Bed shear stress τ_b was defined as:

$$\tau_b = \rho u_*^2 \quad (2.12)$$

By replacing the definition of eddy viscosity and bed shear stress into equation 2.10a and integrating, Engelund (1975) found the tangential velocity follows a logarithmic distribution (see eq. 2.13).

$$\frac{v_\theta}{u_*} = \frac{1}{\kappa} \ln \frac{\zeta}{1 - \zeta} + C \quad (2.13)$$

Where ζ is z/h and C is an integration constant. For a hydraulically rough turbulent flow, tangential velocity v_θ vanishes at $z = k_B/30$; where k_B is the equivalent sand roughness height of the bottom. It leads equation 2.13 to:

$$\frac{v_\theta}{u_*} = \frac{1}{\kappa} \ln \frac{\zeta}{1 - \zeta} + \frac{1}{\kappa} \ln \frac{30h}{k_B} \quad (2.14)$$

Furthermore, considering that the lid rotates with an angular velocity Ω_T and also that flow velocity vanishes at $z = h - k_T/30$ (k_T is lid roughness height); equation 2.13 becomes:

$$\frac{r\Omega_T}{u_*} = \frac{1}{\kappa} \left(\ln \frac{30h}{k_T} + \ln \frac{30h}{k_B} \right) \quad (2.15)$$

Engelund (1975) pointed out that through equation 2.15 shear velocity and bed shear stress can be estimated by means of the angular velocity of the lid. In order to solve for the radial

component of shear stress τ_r , equation 2.14 ($v_\theta = u_* f(\zeta)$) is replaced into equation 2.10b and integrated as follows:

$$\frac{\tau_r}{\rho h} = -\frac{u_*^2}{r} \int_0^\zeta f^2(\xi) d\xi + \zeta g \frac{\partial h}{\partial r} + C \quad (2.16)$$

Where C is an integration constant. To solve for the radial component of flow velocity v_r , Engelund (1975) introduced the following expression,

$$\frac{\tau_r}{\rho} = \kappa u_*^2 \zeta (1 - \zeta) \frac{\partial v_r}{\partial \zeta} \quad (2.17)$$

Note that equation 2.17 comes from replacing equation 2.11 into equation 2.10a for the radial component. Replacing equation 2.17 into equation 2.16 and integrating it was found that,

$$\frac{\kappa v_r}{u_*^2} = -\frac{h}{r} F(\zeta) - \frac{gh}{u_*^2} \frac{dh}{dr} \ln(1 - \zeta) + \frac{Ch}{u_*^2} \ln \frac{\zeta}{1 - \zeta} + C_1 \quad (2.18)$$

Where C_1 is an integration constant and F becomes:

$$F(\zeta) = \int_0^\zeta \frac{d\xi}{\xi(1 - \xi)} \int_0^\xi f^2 d\xi \quad (2.19)$$

Engelund (1975) used two boundary conditions to find the integration constants C and C_1 . First, he applied the approximation proposed by Rozovskii (1957) for rough walls:

$$\frac{\tau_r}{\tau_b} = \frac{v_r}{v_\theta} \quad (2.20)$$

Thus, after some manipulations it was found that:

$$C_1 = \frac{Ch}{u_*^2} \ln \frac{30h}{k_B} \quad (2.21)$$

On the other hand, instead of considering a rough boundary at the lid, a smooth wall was

assumed at the top boundary. Rozovskii (1957) and Kikkawa et al. (1976) found that τ_r is negligible at $\zeta = 1$ for a smooth boundary (Falcon, 1984); leading to the following,

$$C = \frac{u_*^2}{r} \int_0^1 f^2(\zeta) d\zeta - g \frac{dh}{dr} \quad (2.22)$$

Finally, the unknown piezometric gradient dh/dr was determined by Engelund (1975) assuming that the net radial flow at a certain r -location is zero:

$$\int_0^1 v_r d\zeta = 0 \quad (2.23)$$

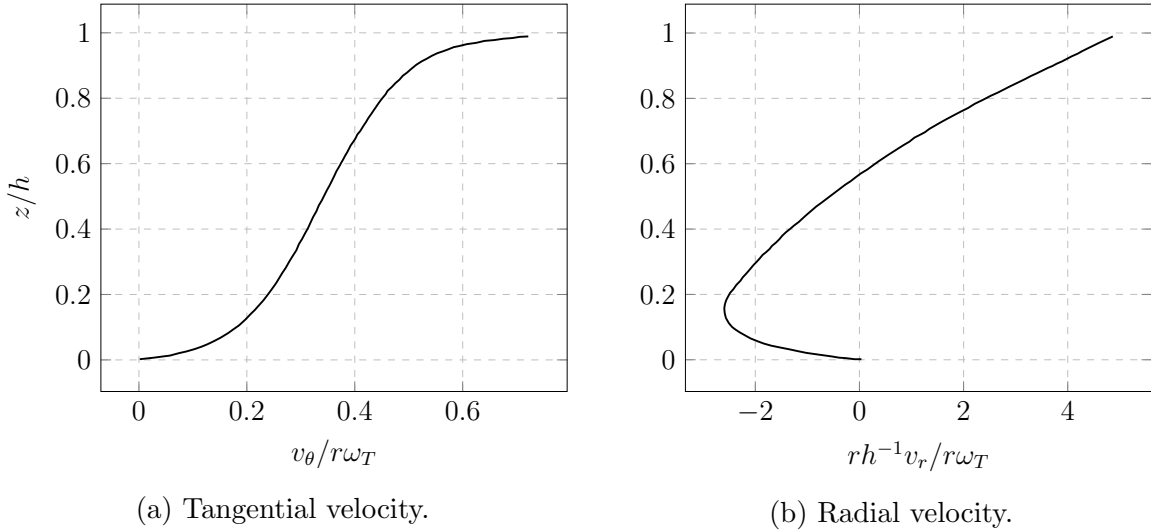


Figure 2.3: Dimensionless velocity distributions according to Engelund (1975).

Radial velocity distribution was developed from a logarithmic distribution of tangential velocity (see eq. 2.14). Motivated by avoiding the singularity solution of the log-law distribution at $z = 0$, Falcon (1979) proposed another velocity distribution for secondary flows considering a power-law approach for the main flow. Under open channel conditions, he considered that the tangential velocity follows the power-law distribution. Falcon (1979) employed the Darcy-Weisbach friction factor of the bed to estimate the exponent n of the

velocity formulation:

$$n = 1/\sqrt{f} \quad (2.24)$$

Thus, the smoother bed, the larger value of n . Contrary to Engelund (1975), Falcon (1979) estimated the eddy-diffusion coefficient from a simplified Boussinesq expression. Then, following the same solution procedure of Engelund (1975) and considering $v_\theta = 0$ at $z = 0$, the integration constants were determined in the Falcon (1979) formulation.

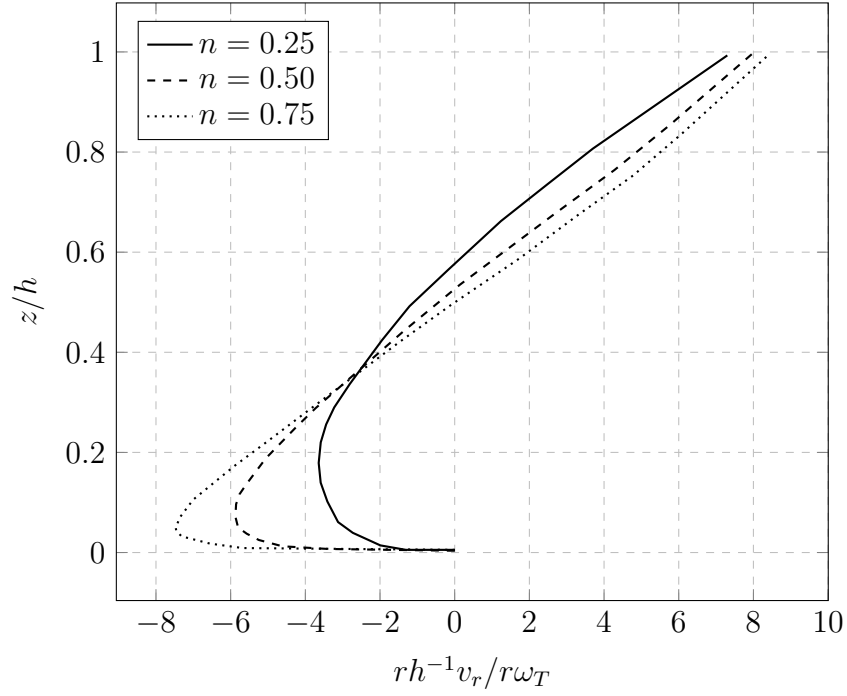


Figure 2.4: Dimensionless radial velocity for several bed roughness according to Falcon (1979).

2.3 Couette Flow

In this section, the basic 2D and 3D Couette flow governing equations are presented in a planar and polar framework system, respectively. It was found important to show them because the Couette flow is the driving mechanism in an annular flume. The first part introduces the Navier-Stokes equations and goes through the solution of a 2D planar Couette

flow. Afterwards, the governing equations for a 3D polar Couette flow are shown. The differences with the simplified dynamic equations proposed by Englund (1975) and Falcon (1979), are remarkable. The later neglects most of the inertial terms in the polar Navier-Stokes equations.

2.3.1 Basics of 2D planar Couette flow

A simple Couette flow is a 2 dimensional flow driven by shearing fluid with an infinitely long and wide plate (Spurk & Aksel, 2008). Consider certain fluid at rest between two infinitely long and wide plates as shown in figure 2.5a. *No slip* condition implies that any viscous fluid touching a surface will stick to that surface; i.e. the fluid will have the same velocity of such surface. If the upper plate is moving to the right with a certain velocity U (see fig. 2.5b), the fluid right below the plate will move accordingly. Because the lower plate has zero velocity, the flow velocity in between necessarily must adjust itself to a certain velocity distribution such as $u(0) = 0$ and $u(D) = U$. Considering a partition of the flow into infinitesimal layers dz -thickness; all the upper layers will have a larger velocity than the fluid layer immediately below (see fig. 2.5c). It means that all the upper layers will exert shear stress on the lower fluid layer due to the velocity difference. In other words, x -momentum is transferred from the moving plate above through the water column as shear stress.

Following Newton's second law, the Navier-Stokes equations express the momentum balance in a infinitesimal control volume of incompressible fluid (see eq. 2.25a to 2.25c).

$$\frac{\partial u}{\partial t} + u \frac{\partial u}{\partial x} + v \frac{\partial u}{\partial y} + w \frac{\partial u}{\partial z} = -\frac{1}{\rho} \frac{\partial p}{\partial x} + \nu \left(\frac{\partial^2 u}{\partial x^2} + \frac{\partial^2 u}{\partial y^2} + \frac{\partial^2 u}{\partial z^2} \right) + g_x \quad (2.25a)$$

$$\frac{\partial v}{\partial t} + u \frac{\partial v}{\partial x} + v \frac{\partial v}{\partial y} + w \frac{\partial v}{\partial z} = -\frac{1}{\rho} \frac{\partial p}{\partial y} + \nu \left(\frac{\partial^2 v}{\partial x^2} + \frac{\partial^2 v}{\partial y^2} + \frac{\partial^2 v}{\partial z^2} \right) + g_y \quad (2.25b)$$

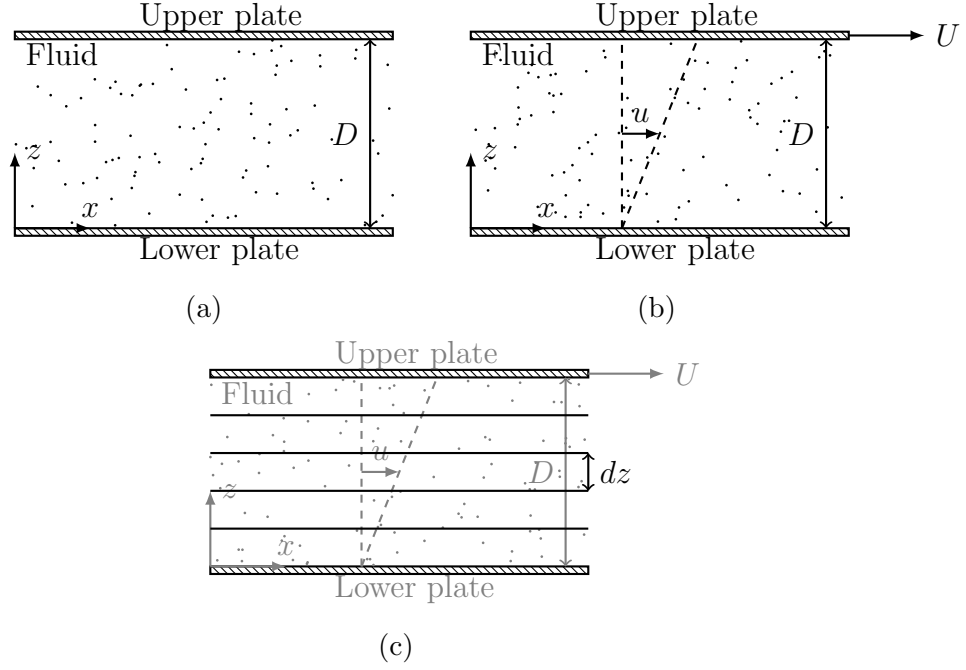


Figure 2.5: 2D planar Couette flow.

$$\frac{\partial w}{\partial t} + u \frac{\partial w}{\partial x} + v \frac{\partial w}{\partial y} + w \frac{\partial w}{\partial z} = -\frac{1}{\rho} \frac{\partial p}{\partial z} + \nu \left(\frac{\partial^2 w}{\partial x^2} + \frac{\partial^2 w}{\partial y^2} + \frac{\partial^2 w}{\partial z^2} \right) + g_y \quad (2.25c)$$

Where u , v , and w are the streamwise, lateral, and vertical components of flow velocity, respectively; ρ is fluid density; p is pressure; g_x , g_y , and g_z are the streamwise, lateral, and vertical components of the gravitational acceleration, respectively; and x , y , and z are the streamwise, lateral, and vertical coordinates, as well; and t is time. The physical meaning

of equations 2.25a to 2.25c:

$$\begin{aligned}
\frac{\partial u_i}{\partial t} &: \text{Time rate of change of momentum per unit mass} \\
\frac{1}{\rho} \frac{\partial p}{\partial x_i} &: \text{Pressure force per unit mass} \\
u_j \frac{\partial u_i}{\partial x_j} &: \text{Net convective inflow of rate of momentum (Inertial force) per unit mass} \\
\nu \frac{\partial^2 u_i}{\partial x_j^2} &: \text{Net diffusive inflow rate of momentum (Viscous force) per unit mass} \\
g_i &: \text{Gravitational acceleration}
\end{aligned} \tag{2.26a}$$

Since the 2D planar Couette flow implies uniformity along the y axis, all the derivative with respect to y becomes zeros in equations 2.25a to 2.25c. There is no flux along y and z because the drive force is only applied by the upper plate in the x direction. Thus, flow velocity components v and w become zero as well. Equations 2.25a to 2.25c turn into:

$$\frac{\partial u}{\partial t} + u \frac{\partial u}{\partial x} + \cancel{v \frac{\partial u}{\partial y}} + \cancel{w \frac{\partial u}{\partial z}} = -\frac{1}{\rho} \frac{\partial p}{\partial x} + \nu \left(\frac{\partial^2 u}{\partial x^2} + \cancel{\frac{\partial^2 u}{\partial y^2}} + \frac{\partial^2 u}{\partial z^2} \right) + 0 \tag{2.27a}$$

$$\cancel{\frac{\partial v}{\partial t}} + \cancel{u \frac{\partial v}{\partial x}} + \cancel{v \frac{\partial v}{\partial y}} + \cancel{w \frac{\partial v}{\partial z}} = -\cancel{\frac{1}{\rho} \frac{\partial p}{\partial y}} + \nu \left(\cancel{\frac{\partial^2 v}{\partial x^2}} + \cancel{\frac{\partial^2 v}{\partial y^2}} + \cancel{\frac{\partial^2 v}{\partial z^2}} \right) + 0 \tag{2.27b}$$

$$\cancel{\frac{\partial w}{\partial t}} + \cancel{u \frac{\partial w}{\partial x}} + \cancel{v \frac{\partial w}{\partial y}} + \cancel{w \frac{\partial w}{\partial z}} = -\frac{1}{\rho} \frac{\partial p}{\partial z} + \nu \left(\cancel{\frac{\partial^2 w}{\partial x^2}} + \cancel{\frac{\partial^2 w}{\partial y^2}} + \cancel{\frac{\partial^2 w}{\partial z^2}} \right) + g \tag{2.27c}$$

Therefore:

$$\frac{\partial u}{\partial t} + u \frac{\partial u}{\partial x} = -\frac{1}{\rho} \frac{\partial p}{\partial x} + \nu \left(\frac{\partial^2 u}{\partial x^2} + \frac{\partial^2 u}{\partial z^2} \right) \tag{2.28a}$$

$$\frac{1}{\rho} \frac{\partial p}{\partial z} = g \tag{2.28b}$$

Note that fluid was considered incompressible by taking the density to be constant. Equation

2.28b is solved for p by integration as follows,

$$dp = g\rho dz \quad (2.29a)$$

$$\int dp = g\rho \int dz \quad (2.29b)$$

$$p = g\rho z + C \quad (2.29c)$$

When $z = 0$, $p = p_0$:

$$p_0 = g\rho * 0 + C \quad \therefore \quad C = p_0 \quad (2.29d)$$

$$p(z) = g\rho z + p_0 \quad (2.29e)$$

According to equation 2.29e, pressure in a 2D planar Couette flow is hydrostatic; i.e. is only function of z . On the other hand, continuity equation of an incompressible fluid states that the divergence of the velocity field is equal to zero:

$$\frac{\partial u}{\partial x} + \frac{\partial v}{\partial y} + \frac{\partial w}{\partial z} = 0 \quad (2.30)$$

Since v and w are equal to zero, the continuity equation is reduced to equation 2.31, i.e. the flow is uniform in the streamwise direction.

$$\frac{\partial u}{\partial x} = 0 \quad (2.31)$$

Momentum balance equation of the 2D planar Couette flow under steady-state conditions may be written, taking into consideration that $\partial u/\partial x = 0$ and p is only function of z as

following:

$$\cancel{\frac{\partial u}{\partial t}} + u \cancel{\frac{\partial u}{\partial x}} = -\cancel{\frac{1}{\rho} \frac{\partial p}{\partial x}} + \nu \left(\cancel{\frac{\partial^2 u}{\partial x^2}} + \frac{\partial^2 u}{\partial z^2} \right) \quad (2.32a)$$

$$0 = \nu \frac{\partial^2 u}{\partial z^2} \quad (2.32b)$$

Because the kinematic viscosity ν cannot be equal to zero:

$$C = \frac{\partial u}{\partial z} \quad (2.32c)$$

So that, u increases linearly with z -elevation. Considering that $u(0) = 0$ and $u(D) = U$,

$$u = U \frac{z}{D} \quad (2.32d)$$

By definition, $\partial u / \partial z$ is the shear strain rate. It expresses the angular velocity deformation of a sheared fluid. In Newtonian fluids, like water, there is a linear connection between the shear strain rate and the shear stress. Such proportionality constant is the dynamic viscosity $\mu = \nu * \rho$. Therefore, equation 2.32c becomes,

$$\frac{\tau}{\rho} = \nu \frac{\partial u}{\partial z} = \nu \frac{U}{D} \quad (2.33)$$

Where τ is shear stress, ρ is fluid density, and ν is kinematic viscosity. Recall that in the fluid layers analogy (see fig. 2.5c), all the upper layers exert shear stress on the lower layer of fluid because of the velocity gradient. Fluid shear stress in Couette flow is constant in the vertical since the velocity gradient is constant. Equation 2.32c shows that a constant scalar is transferred along the fluid depth; such scalar becomes the shear stress over fluid density transferred from the moving plate.

2.3.2 Basics of 3D polar Couette flow

Consider a resting fluid in an annular section confined by two plates as shown in figure 2.6a; a polar reference framework is used conveniently to describe its hydrodynamic behavior. At certain elevation $z = D$, the fluid is sheared by the upper plate following a circular motion (see fig. 2.6b). The tangential velocity of the lid will vary with the radial coordinate as function of the angular velocity:

$$v_T = \Omega_T r \quad (2.34)$$

Where v_T is the tangential velocity of the lid and Ω_T is the angular velocity. Due to the no slip condition the fluid velocity at $z = D$ will have the same tangential velocity as the lid. Considering that the bottom is fixed, the tangential velocity of the fluid will be zero at $z = 0$.

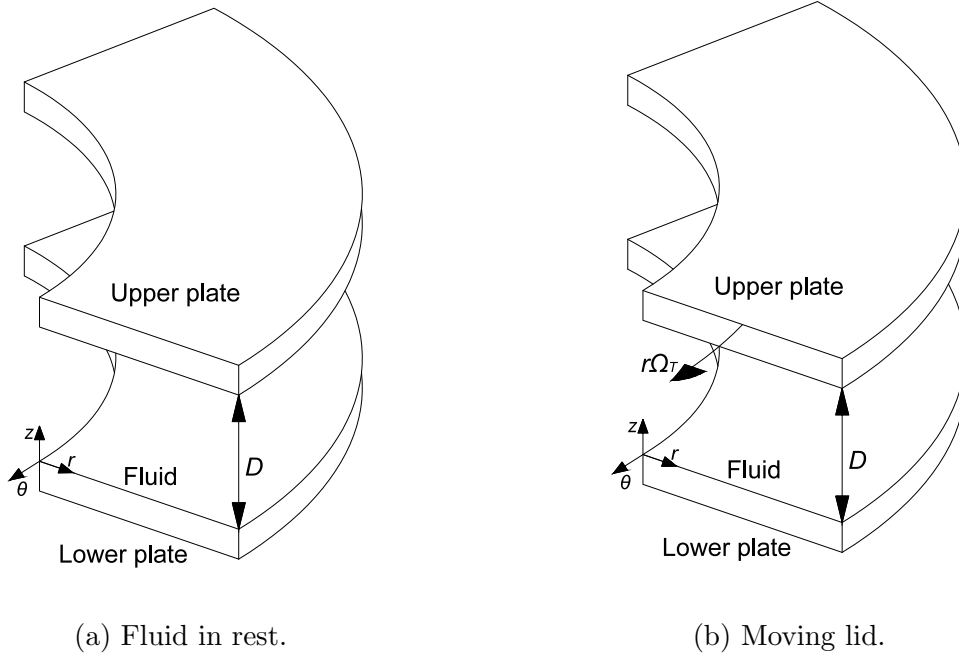


Figure 2.6: Three-dimensional Couette flow.

Considering the angular velocity Ω_T constant and incompressible fluid, the flow becomes steady and the derivative with respect to θ become zero in the Navier-Stokes equations. Booiij

(1994) presents the following set of governing equations for a three-dimensional Couette flow in an annular flume:

$$\frac{\partial}{r\partial r}(rv_\theta v_r) + \frac{\partial}{\partial z}(v_\theta w) + \frac{v_\theta v_r}{r} = \nu \left(\frac{\partial^2 v_\theta}{\partial r^2} + \frac{\partial v_\theta}{r\partial r} + \frac{\partial^2 v_\theta}{\partial z^2} - \frac{v_\theta}{r^2} \right) + g_\theta \quad (2.35a)$$

$$\frac{\partial}{r\partial r}(rv_r^2) + \frac{\partial}{\partial z}(v_r w) + \frac{v_\theta^2}{r} = -\frac{1}{\rho} \frac{\partial p}{\partial r} + \nu \left(\frac{\partial^2 v_r}{\partial r^2} + \frac{\partial v_r}{r\partial r} + \frac{\partial^2 v_r}{\partial z^2} - \frac{v_r}{r^2} \right) + g_r \quad (2.35b)$$

$$\frac{\partial}{r\partial r}(rv_r w) + \frac{\partial}{\partial z}(w^2) = -\frac{1}{\rho} \frac{\partial p}{\partial z} + \nu \left(\frac{\partial^2 w}{\partial r^2} + \frac{\partial w}{r\partial r} + \frac{\partial^2 w}{\partial z^2} \right) + g_z \quad (2.35c)$$

Booij (1994) pointed out that the appropriate boundary conditions at the lid are:

$$v_\theta(r, D) = r\Omega_T \quad (2.36a)$$

$$v_r(r, D) = w(r, D) = 0 \quad (2.36b)$$

On the other hand, when the bottom is fixed, they become:

$$v_\theta(r, 0) = v_r(r, 0) = w(r, 0) = 0 \quad (2.37)$$

Along the Engelund (1975)'s derivation, it was stated that the tangential momentum is transferred by the moving lid in the water depth and radial shear stress results from the imbalance between centrifugal force and pressure gradient. However, note that some other inertial terms were not considered in the simplified dynamic equation of Engelund (1975) and Falcon (1979). Falcon (1984) explained that their dynamic equations may reproduce the hydrodynamic of main and secondary flows for weakly curved and wide.

2.4 Summary

This literature review revised the following points: (i) a basic description of an annular flume, (ii) advantages and disadvantages of using annular flumes, (iii) some previous experimental and theoretical work, and (iv) basis of 2D and 3D Couette flow. An annular flume is a ring-shape flume that generates a three dimensional Couette flow by rotation of its lid and/or itself. Motivated by studying cohesive sediment deposition, it was proposed and built as an annular flume by Partheniades et al in 1966. Due to the centrifugal force, the flow develops a secondary current; therefore, the flow in the annular flume becomes helicoidal. To mitigate the undesirable secondary current, some authors have proposed to rotate the lid and the bottom (tank) independently in opposite directions. Once the secondary flow is minimized, the hydrodynamics in the annular flume may represent an infinite and straight flow. In consequence, annular flumes become a versatile device to reproduce natural streams such as aquatic ecosystems. Furthermore, it was found that annular flumes can be used as prototypes to study stratified flows and bed evolution under curved flows. Even though the secondary current is minimized, studies point out that it may scale back the deposition velocity of sediments. It implies that settling experiments should be conducted being aware of such fact.

Besides the studies that use annular flumes, an important amount of effort has been put into characterizing the hydraulic of annular flumes. Motivated by minimizing the secondary flow and obtaining uniform distribution of bed shear stress at the bottom, most of the hydraulic characterization was focused on the calibration of the flume; i.e. finding a combination of lid and bottom rotation speed that minimized the secondary current. Several studies demonstrated that simultaneous rotation of lid and bottom generates two secondary cells that may cancel each other out. Thus, it was found in literature that there are two positions regards to the calibration criteria. The first one proposes that a unique calibration curve is needed regardless of the purpose of the experiment (bed erosion or suspended

sediment deposition). It considers that once the tangential bed shear stress is uniformly distributed in the transversal direction any secondary current practically vanishes. On the other hand, the second position claims that two calibration curves are needed, one for bed erosion and another for suspended sediment deposition. The earlier should produce a uniform bed shear stress along the cross section; whilst the second calibration curve should minimize the strength of the secondary flow.

In order to make a measurement of the secondary flow strength and bed shear stress, it was found that there are several methodologies as well. To estimate the intensity of the secondary current, three criteria have been proposed: (i) the specific energy of the secondary current (expressed in terms of the vertical and radial component of the flow), (ii) the ratio of secondary flow kinetic energy to the kinetic energy of the tangential flow, and (iii) the ratio of the maximum secondary flow velocity to the maximum tangential velocity. Likewise, it was encountered that there is no unique definition for a characteristic mean bed shear stress. Bed shear stress has been defined: (i) in terms of the force applied by the lid/tank (torque), (ii) as the surface-average of the shear stress variation along the physical boundaries, and (iii) through empirical relationships in terms of the lid/tank rotation.

Finally, it was presented the theoretical development of Engelund (1975) of the radial and tangential velocity distribution in an annular flume. Furthermore, the basic governing equations of a 2D and 3D Couette flow was shown. The Engelund formulation solved the radial and tangential velocity distributions from a shear stress and a simplified dynamic equation. Engelund (1975) stated that the shear stress imposed by the lid is transferred along the water column without changing its magnitude. On the other hand, the simplified dynamic equation expressed that the difference between the centrifugal force and the pressure gradient is balanced by the radial shear stress. Engelund formulations agreed with other authors in: (i) the radial shear stress is negligible at the lid or bed when the surface is smooth, (ii) the net flow at a certain r -location is zero, and (iii) the scalar eddy viscosity is not constant along the z -direction. Thus, Engelund (1975) found a logarithmic distribution

for the tangential velocity and an integral expression for the radial velocity distribution. Comparing initial simplified dynamic equation with the 3D Couette flow, it is notable that most of the inertial terms. However, Falcon (1984) showed that a simplified dynamic equation may work well for weakly curved and wide open channel flows.

Chapter 3

Laboratory Experiments: Materials and Methodology

3.1 Introduction

This chapter will be focused on describing the annular flume used as prototype for this experiment, the acoustic instrument used to measure the tangential and radial component of the flow, and the post-processing treatment of the measured data. The annular flume used is a $1.5m$ ring-shape flume with a capacity of $370L$. Its tank and lid can rotate independently in order to compensate for undesirable secondary flow effect. However, the tank stayed fixed and lid rotated over a rotation velocity of $0.5rpm$ to $4.0rpm$. Tangential and radial velocity profiles were measured using an Ultrasound Velocity Profiler (UVP-DUO). This instrument was capable of measuring the Doppler Frequency Shift along an ultrasound beam and correlating it with the flow velocity. Assuming that particles in the flow moves with the same velocity as the fluid, the UVP-DUO estimates the Doppler Frequency Shift knowing the fluid and ultrasound propagation properties. Internally, the UVP-DUO system is programmed to determine the flow velocity when the measuring probe is stationary. Because the measuring probes were placed at the moving lid, some post-processing computations were needed to obtain the correct tangential velocity measurements. Finally, the methodology followed to compute the radial and tangential velocity profiles from Engelund's formulation is presented.

3.2 The Annular Flume

The annular flume used in this project belongs to the Ven Te Chow Hydrosystem Laboratory at the University of Illinois. It was built by *Engineering Laboratory Design, Inc* (Lake City, MN) in 2000 . In general terms, it is a $1.5m$ ring-shape flume with a capacity of $370L$ and it consists of 5 main parts: (i) a $1.5m$ diameter fiber glass tank, (ii) a rotating plexiglas cover, (iii) a supporting frame, (iv) two drive mechanisms, and (v) two motor controllers.

The flume has $75cm$ and $55cm$ of outer and inner radius, respectively. With $20cm$ width by $45cm$ depth of cross section, the annular tank may carry $370L$ of fluid maximum. An inlet/outlet garden hose male fitting with a ball valve was placed at the bottom for draining and filling of the tank. According to the manufacturer, the flume is fabricated from laminated fiberglass reinforced plastic. Its interior surfaces were painted with glass smooth vinyl-ester gel-coat. However, the bottom of the flume was covered with a fine sand paper in a later study. Even though the roughness of the bottom was change, it was found by Waterman and Garcia (2014) all surfaces may be considered smooth for hydraulic purposes. On the other hand, the exterior surfaces are covered with polyester gel-coat enamel. The tank is provided with a $40cm$ wide by $35cm$ tall observation window to have visual access into the flume. The observation window was fabricated on curved $0.64cm$ plexiglas to match the outer radius of the flume. To bring the flume into rotation, the tank lies on a turntable of high density board attached to a central steel support structure. A drive shaft and a shaft bearing were welded with the steel structure in order to drive the axial flume rotation.

The annular flumes is provided with a $0.64cm$ plexiglas lid attached to a supporting steel frame. It is elevation adjustable and it may rotate independently to the tank. Therefore, the lid fits the flume with edge clearance to allow free rotation. In case of lid alignment, screws with double jam nuts allow some shifting of the plexiglas cover. It may be located at a minimum depth of $20cm$ from the bottom of the tank to a maximum clearance height of $25cm$ above the flange of the flume. The cover assembly vertically moves either upward or

downward along a 5.08cm diameter 5 pitch steel ACME threaded rod. To ensure that the lid will not move during the experiments, the cover may be fixed to the threaded rod with an arrangement of nuts.

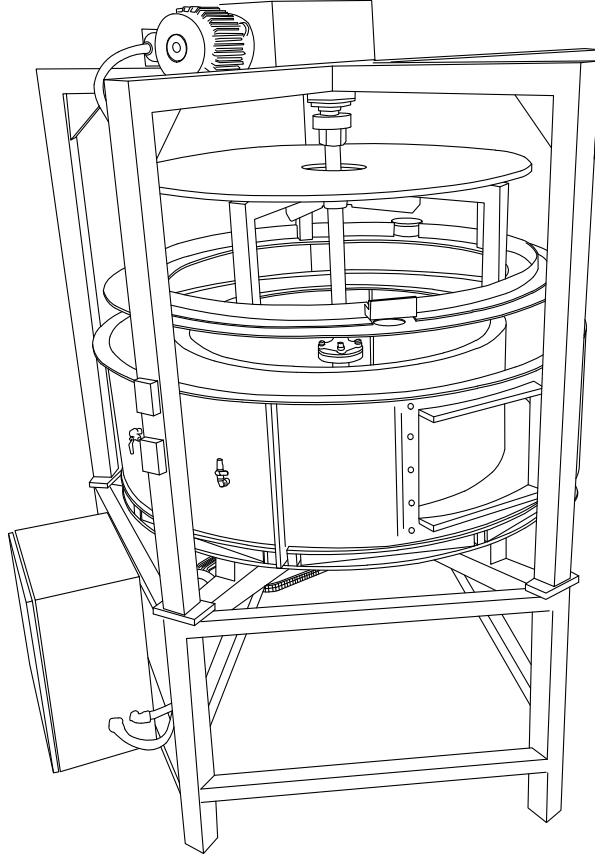


Figure 3.1: Annular flume at the Ven Te Chow Hydrosystem Laboratory.

The tank and lid are supported by an ensemble of two five-leg frames. They are fabricated of structural tubing joined by welding. The upper and lower frames are attached through bolted match plates. The lower legs are provided with adjustable leveling pads in order to level the turntable. The manufacturer points out that there are two sets of bearing at the center of each frame for the upper and lower drive shaft.

Two drive motors bring the lid and tank into rotation, independently. The cover ensemble is allowed to rotate in either direction at 0.2 to 16 rpm. However, the lid was set to rotate

in only one direction. The upper rotation system consists on a 0.5HP TENV 1750RPM AC motor and a worm gear reducer connected to a 3/4" wide timing belt and pulley. Additionally, three piloted flanged ball bearing align the ACME rod with the flume and turntable. On the other hand, the rotation system for the tank consists on 0.5HP TENV 1150RPM AC motor and a worm gear reducer connected to a 1/2" pitch chain and sprockets. It allows the tank to rotate at 0.2 to 9.6 rpm. Each motor has a 0.5HP transistor inverter type, variable speed motor control to set the rotation speed of the motor. In addition, two remote control stations are located on the frame.

3.3 The Ultrasound Velocity Profiler

Acoustic measuring techniques are used in a wide variety of fields and scales. The principle of acoustic measurements is used for medical, geophysics, and fluid mechanics applications, among others. As a general idea, it is based on emitting a sound signal with known frequency through a known medium and acquiring the echo produced by any elements along the signal path. Thus, objects may be shaped virtually in terms of their echo. Also, the speed of a moving element in the medium can be correlated with the characteristics of its echo. Thus, non invasive examinations of internal organs in medicine, sedimentology and stratigraphy exploration in geology, and flow velocity measurements in fluid mechanics are possible through acoustic measuring techniques. This project used an Ultrasonic Velocity Profiler (UVP) to measure the radial and tangential velocity profiles in an annular flume. Therefore, the objective of this section is to present a description of the UVP hardware and the physics behind. To achieve such goal, the main components of the UVP are reported as well as the computations to estimate the flow velocity. This section is divided into three subsections: (i) the physical phenomenon used by the UVP, (ii) a description of the main components of a UVP, and (iii) how the UVP computes the velocity profiles.

3.3.1 Physics of an Ultrasound Velocity Profiler: Doppler Effect

An UVP is an electronic device that consists on a Central Processing Unit, a licensed software to control the system, and one or more transducers. Transducers are cylindrical probes capable to emit an ultrasound beams. Also, transducers may receive the echo produced after the beam hits an obstacle. Figure 3.2 illustrates the concept of an UPV system.

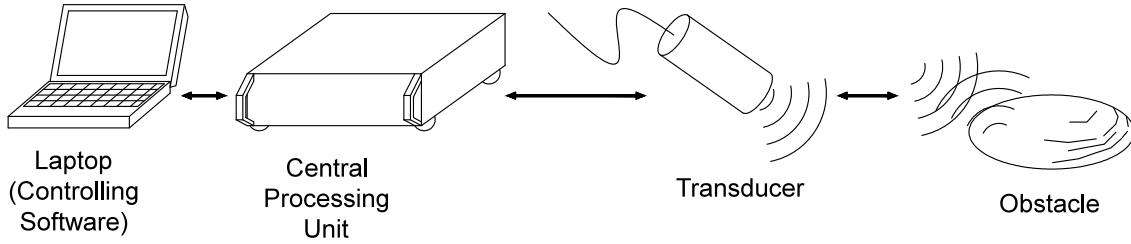


Figure 3.2: Schematic illustration of an UVP system.

The physical principle used for the UVP to estimate the flow velocity is the Doppler Effect. It is the perception of frequency change of a wave (sound) when the sound source approaches or moves away the observer. Serway and Jewett (2014) explain through a boat analogy the basic concept of Doppler Effect as follows. A stationary boat is anchored in the middle of a lake. An observer in the boat reports that waves hit the boat every $5sec$; i.e., the wave period T is $5sec$. Thus, their frequency f is $1/T = 0.2Hz$. If the boat moves in direction of the oncoming waves, the observer will perceive the waves hitting the boat faster than each $5sec$; in other words, the wave period T decreases from the observer's perspective. Therefore, the apparent wave frequency will increase because $f = 1/T$. In case the boat moves away the approaching waves, the wave period will increase from the observer's impression. It would decrease the apparent wave frequency. Therefore, it may be argued that the apparent change of frequency is function of the relative velocity between the waves and the observer.

In this context, three major cases may be encountered: (i) moving observer only, (ii) moving sound source only, and (iii) both observer and sound source are moving. The appar-

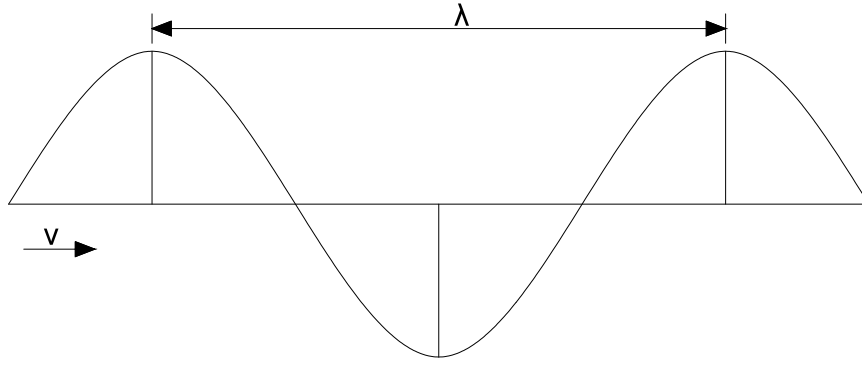


Figure 3.3: Wavelength of a monochromatic wave.

ent frequency will be determined by the relationship between the relative velocity of observer and sound source. Figure 3.4 illustrates an observer and sound source. Consider the case where the sound source is stationary and the observer is moving toward the source (see fig. 3.4a); i.e., $v_s = 0$ and $v_o \neq 0$. The medium (air) is uniform, therefore the waves will propagate uniformly in all directions. If the wavelength produced by the source is λ and the speed of sound is v (see fig. 3.3), the actual wave frequency f becomes:

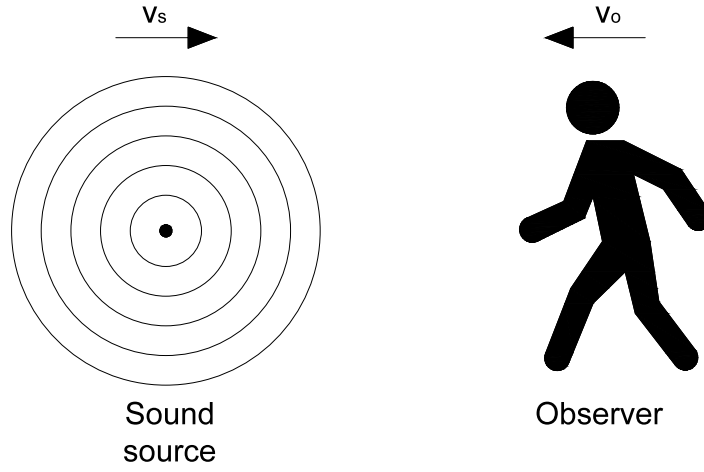
$$f = \frac{v}{\lambda} \quad (3.1)$$

Thus, the observer would receive the waves at a frequency f in case both observer and sound source are stationary. When the observer moves towards the source, the speed of the wave relative to the observer becomes:

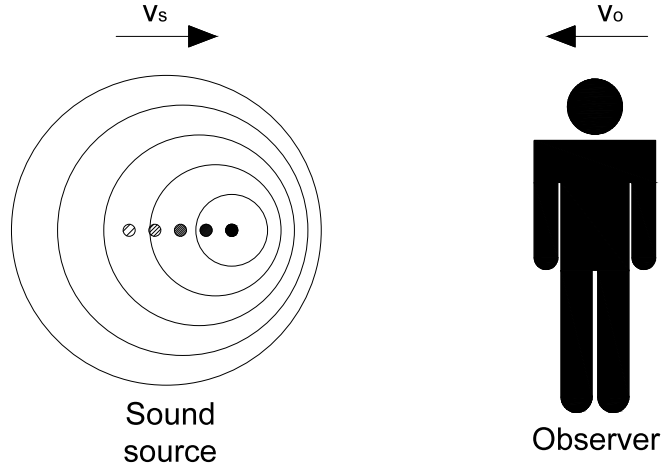
$$v' = v + v_o \quad (3.2)$$

In consequence, the frequency perceived by the observer or apparent frequency f' is:

$$f' = \frac{v'}{\lambda} = \frac{v + v_o}{\lambda} \quad (3.3)$$



(a) Observer is moving with respect to the wave source.



(b) Wave source is moving with respect to observer.

Figure 3.4: Doppler effect as result of moving observer or wave source.

It implies that the frequency increases when the observer moves towards the sound source.

Using equation 3.1, equation 3.3 may be rearranged as follows:

$$f' = \frac{v + v_o}{\lambda} \quad (3.4a)$$

$$f' = \frac{v + v_o}{v/f} \quad (3.4b)$$

$$f' = \left(\frac{v + v_o}{v} \right) f \quad (3.4c)$$

On the other hand, when the observer moves away the source, the relative velocity v' turns into:

$$v' = v - v_o \quad (3.5)$$

Therefore, the apparent frequency f' becomes:

$$f' = \left(\frac{v - v_o}{v} \right) f \quad (3.6)$$

Equation 3.4c may be used in a formal sense when the the observer is moving and the source is stationary. The observer velocity v_o becomes either positive or negative when the observer moves towards or away the source, respectively.

Consider the case where the observer is stationary and the source is moving towards the observer; i.e., $v_o = 0$ and $v_s \neq 0$. Figure 3.4b shows the source approaching the observer to the right. Each new wave front will be produced to the right of the location where the previous wave was produced. It shortens the wavelength from the observer's perspective (see fig. 3.4b). Because the source moves at a velocity v_s and each new wave is produce at a period T , the wavelength is shortened by $\Delta\lambda = v_s T$. Thus, the apparent wavelength λ' becomes:

$$\lambda' = \lambda - \Delta\lambda \quad (3.7a)$$

$$\lambda' = \lambda - v_s T \quad (3.7b)$$

$$\lambda' = \lambda - \frac{v_s}{f} \quad (3.7c)$$

Using equation 3.7c, the apparent wave frequency f' may be stated as follows:

$$f' = \frac{v}{\lambda'} \quad (3.8a)$$

$$f' = \frac{v}{\lambda - v_s/f} \quad (3.8b)$$

$$f' = \frac{v}{v/f - v_s/f} \quad (3.8c)$$

$$f' = \left(\frac{v}{v - v_s} \right) f \quad (3.8d)$$

Equation 3.8d shows that the wave frequency perceived by the observer will increase if the sound source moves towards the observer. By following the same procedure, it may be found the apparent frequency when the source moves away the observer:

$$f' = \left(\frac{v}{v + v_s} \right) f \quad (3.9)$$

Similar to equation 3.4c, equation 3.8d may be used to express both cases where the source moves towards or away the observer. Thus, v_s becomes positive or negative when the source moves towards or away observer, respectively. The general Doppler-shift expression results from combining equation 3.4c and 3.8d:

$$f' = \left(\frac{v + v_o}{v - v_s} \right) f \quad (3.10)$$

UVP is capable of measuring the instantaneous flow velocity along an ultrasound beam. It uses the Doppler Shift of the echoed ultrasound after the beam hits a moving particle. Doppler shift is defined herein as the difference between the emitted and received frequency.

Thus, instantaneous velocity series are determined by means of the variation of the Doppler shift in time.

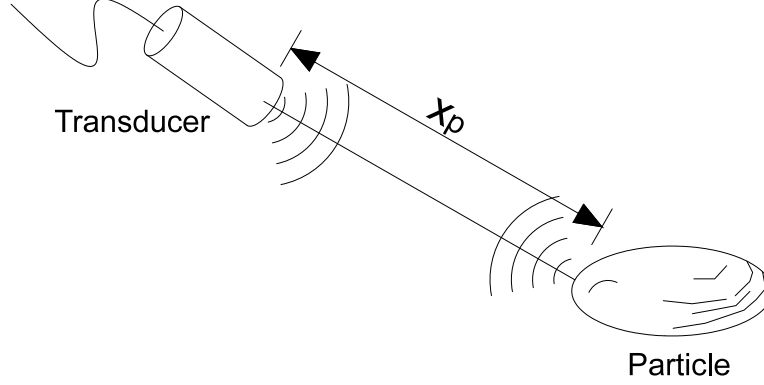


Figure 3.5: Sketch of a traveling ultrasound signal and its echo after it hits a moving particle.

Also, UVP can determine the position of the moving particle. The transducer or probe sends a short ultrasound signal along the measuring axis; then, it turns into a reception mode. Part of the signal dissipates and part echoes back after it hits a moving particle. The same transducer detects the echoed ultrasound and the UVP system records delay time t_p . It is defined as the time elapsed between the signal emission and echo detection. From equation 3.11, the distance between transducer and the particle x_p can be solved. Note that the number 2 shows up since the signal has to travel twice the distance x_p (see fig. 3.5).

$$t_d = \frac{2x_p}{v} \quad (3.11)$$

Where v , is the propagation velocity of sound in the medium. If the particle moves with non-zero velocity, there will be an apparent change of frequency in the echoed signal.

In order to estimate the particle velocity, the UVP goes through two phases. First, it acts as stationary sound source. The first apparent ultrasound frequency may be computed from equation 3.4c as follows:

$$f'_1 = \left(\frac{v + v_p}{v} \right) f \quad (3.12)$$

Where, f'_1 is the first apparent ultrasound frequency, v_p is particle velocity, and f is the original ultrasound frequency. In a second phase, the transducer becomes an stationary observer and the particle turns into a moving source. Thus, a second apparent ultrasound frequency is computed using equation 3.8d:

$$f'_2 = \left(\frac{v}{v - v_p} \right) f'_1 \quad (3.13)$$

Where f'_2 is the second apparent ultrasound frequency. Replacing equation 3.12 into equation 3.13:

$$f'_2 = \left(\frac{v}{v - v_p} \right) \left(\frac{v + v_p}{v} \right) f \quad (3.14a)$$

$$f'_2 = \left(\frac{v + v_p}{v - v_p} \right) f \quad (3.14b)$$

Note that equation 3.14b resembles equation 3.10 when $v_o = v_s = v_p$. Using equation 3.14b, the Doppler shift Δf may be computed as follows:

$$\Delta f = f'_2 - f \quad (3.15a)$$

$$\Delta f = \left(\frac{v + v_p}{v - v_p} \right) f - f \quad (3.15b)$$

$$\Delta f = \left(\frac{v + v_p}{v - v_p} - 1 \right) f \quad (3.15c)$$

$$\Delta f = \left(\frac{2v_p}{v - v_p} \right) f \quad (3.15d)$$

Considering that the ultrasound propagation is significantly larger than the particle velocity

$v \gg v_p$:

$$\Delta f = \frac{2v_p}{v} f \quad (3.15e)$$

Solving for the particle velocity v_p from equation 3.15e:

$$v_p = \frac{\Delta f}{2} \frac{v}{f} \quad (3.16a)$$

Recall that $v = \lambda f$ (see eq. 3.1):

$$v_p = \Delta f \frac{\lambda}{2} \quad (3.16b)$$

Thus, the UVP can compute the velocity and position of a moving particle by detecting the delay time of its echo and Doppler shift. If the particle is small enough, it can be moved with the same velocity as the flow. Therefore, the UVP would be able to measure the instantaneous velocity at any location of the flow. Furthermore, by detection of the Doppler shift's sign, it also provide accurate information of the velocity direction.

3.3.2 Hardware and Software Description of the Ultrasound Velocity Profiler

The Ultrasound Velocity Profiler belongs to the Ven Te Chow Hydrosystem Laboratory and was manufactured by *Met-Flow SA*. This model is a UVP-DUO and it is composed of three major elements: (i) the UVP-DUO unit, (ii) one or more transducers, and (iii) a laptop with the controller software *UVP Monitor*. Met-Flow SA (2002) states that all the measuring components are contained inside the UVP-DUO unit. Transducers produce and do the "listening" of the ultrasound signal. Pre-processing, processing analysis, and setting up is conducted through remote control by the UVP-DUO Monitor software. Furthermore, this model is provided with an integrated multiplexer. It allows the system to generate flow mapping. Integrated multiplexer is a panel with several ports to connect multiple transducers at the same time. Thus, users may arrange various transducers and program

their measuring sequence.

As many electronic devices, internally the UVP-DUO unit incorporates series of connectors that communicate through synchronized signals. The Echo Signal Output is a connector that bridges from the BNC connector (transducers) to the internal oscilloscope. It control the emission/reception dynamic of the ultrasound signal and its echo. Thus, it is possible to monitor the ultrasound signal in order to set up transducer parameter and determine position of boundaries. On the other hand, the Ultrasound Pulse Repetition Frequency Trigger Signal Output is a connector that provides "the timing for an ultrasound pulse emission" (Met-Flow SA, 2002). In order to activate the Ultrasound Pulse Repetition Frequency Trigger Signal Output, the External Trigger Input supports its connection to the BNC connectors. The External Trigger Input sends the signal to start to measures the flow velocity. The BNC connectors are the ports for the transducers. In a UVP-DUO system with integrated multiplexer, there are 20 BNC connectors to hook up transducers of $0.5MHz$ to $8MHz$. The system is controlled remotely through an Ethernet port (LAN). In this project, a router connected to the Ethernet port allowed to control the UVP-DUO system via wifi.

Transducers typically are cylindrical probes of $60mm$ long with diameters raging from $8mm$ to $23mm$ and cased in Delrin (high-resistant engineering thermoplastic). They produce ultrasound signals by converting high-frequency electrical pulses into high-frequency mechanical vibrations. Under receiving mode, transducers perform the reversal process: to transform mechanical vibrations (echo) into electrical signals. They come in working frequencies of $0.5MHz$ to $8MHz$; two transducers of $1MHz$ were used in this study. Transducer frequency determines the spatial resolution of the measured velocity profile: the larger frequency, the finer spatial resolution and the shorter measuring distance. A single probe is connected to the BNC connector through a $4m$ standard 50Ω coaxial cable. It provides an attenuation under $0.1dB/m$ for a $8MHz$ signal (Met-Flow SA, 2002). Because probe and cable are firmly attached, there is no possible to extend the cable.

A transducer probe consists on three main components: (i) Active element, (ii) Back-

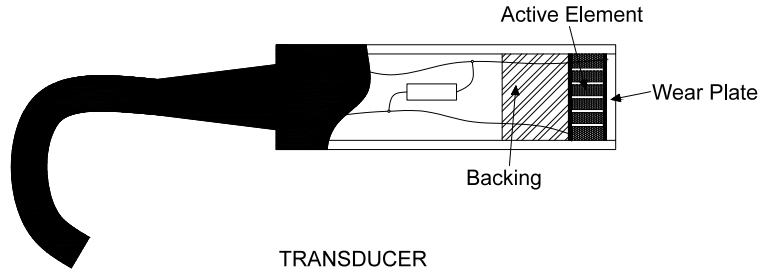


Figure 3.6: Main components of a transducer.

ing, and (iii) Wear plate (see fig. 3.6). Met-Flow SA (2002) points out that the transducer's performance highly depends on the impedance matching between the aforementioned components. The active element is a piezoelectric or ferroelectric material that transforms electric energy into ultrasonic energy. Thus, the active element produces a high-frequency when it is electrically excited. According to Met-Flow SA (2002), the most common material used in UVP transducers is polarised ceramics. Active elements were made of an array of thin ceramic rods surrounded in a polymer matrix. This configuration allows mechanical continuity over the probe face and then along the measuring axial direction. The Backing is a buffer element located behind the active element. Its purpose is to absorb the acoustic energy coming from the back face of the active element. The agility of the transducer to switch between emitting and receiving is function of its impedance matching with the active element. When there is a well matched impedance, backing will absorb the back vibration efficiently. On the other hand, certain degree of mismatching will lead to prolong the active element vibration after the electric signal has been switched off (longer transient). It is because some energy may be reflect back to the active element. Depending on the purpose of the experiment, matching or mismatching impedance might be convenient. For instance, longer transient achieves low temporal resolution because emitting/receiving switch is slow. However, the echo intensity (amplitude) is higher for longer transient because the ultrasonic signal becomes more energetic. Finally, the wear plate provides an impedance transition be-

tween the active element and the medium and protection for internal parts of the probe. The wear plate typically slightly matches the fluid impedance (approximately 10 times smaller than the active element) in order to increase the ultrasound energy output.

UVP Monitor software Version 3 is the interface where users set up all measuring parameters, visualize recorded data in real time, and export the final velocity profiles. Its purpose is to control remotely the UVP-DUO unit through LAN connection. Therefore, the software allows users to specify the initial configuration, such as measuring channel width, measuring window, sound speed, among others. According to Met-Flow SA (2002), this Version is capable of analyzing velocity histogram, auto-correlation, cross-correlation, and power spectrum along the profile. Thus, the software computes turbulence statistics: average, variance, skewness, and kurtosis.

3.3.3 Computation of Velocity Profile

This subsection is devoted to present how a UVP-DUO computes the velocity profile. The analog signal from the echo ultrasound converted into a Doppler shift frequency. Then, the UVP-DUO Monitor Software transforms the raw data into the adequate flow velocity component. A temporal correlation algorithm is used by the software to determine the actual Doppler shift frequency at certain locations along the ultrasound beam. To perform the computations, the system requires information such as transducer orientation, ultrasound signal geometry, and acoustic properties of the medium. The subsection will address the fundamental definitions, measuring limitations, and the actual computation of the velocity profiles.

UVP-DUO discretizes space in one dimension along the ultrasound beam. It divides the measurable space into small volumes (cylinder shape) called channels (see fig. 3.7). The channel width w_{ch} is defined as the length of a measurement volume. Channel width is the same for all channels along the ultrasound beam and specifies the spatial resolution. It is

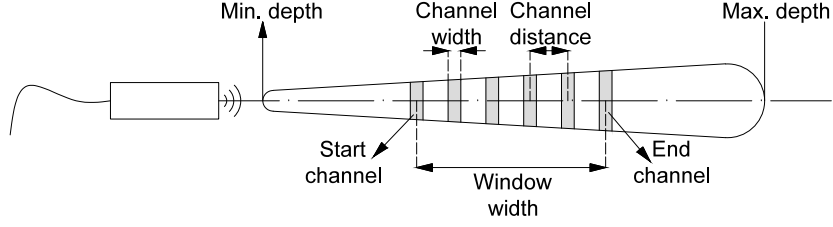


Figure 3.7: Measurement window along a ultrasound beam.

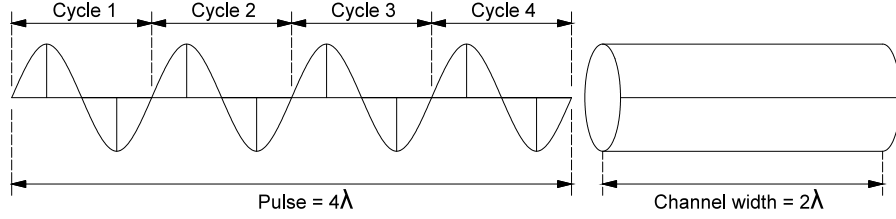


Figure 3.8: Illustration of a pulse (several cycles) passing through a channel (measuring volume).

expressed in terms of the ultrasound properties as follows:

$$w_{ch} = v \frac{n_p}{2f} = \frac{n_p \lambda}{2} \quad (3.17)$$

Where v is the sound velocity, n_p is the number of cycles per pulse, f is the ultrasound frequency, and λ is its wavelength. A pulse becomes the leaving ultrasound signal; it is a burst of cycles that will travel along the beam (see fig: 3.8). Note that the channel width was expressed in terms of the wavelength. According to Met-Flow SA (2002), w_{ch} means to be half the length of a pulse length; it is required that the pulse covers twice the channel width when it reaches one of the channel end faces. The number of pulses n may be set up through the UVP-DUO software interface. The minimum cycles per pulse produced by the unit is 2. However, 4 cycles per pulse was used in these experiments because it is the optimal value recommended by (Met-Flow SA, 2002). The channel distance becomes the separation between the center of two consecutive measurement volumes. This parameter rather than being determined by the signal geometry, is defined by the user. Thus, the channel distance

d_{ch} may or may not be smaller than the channel width w_{ch} . In case $d_{ch} < w_{ch}$, certain percentage of overlapping between two consecutive channels takes place. The UVP-DUO system is capable of capturing channel overlapping. It does not imply improvement on the spatial resolution because the system averages over the overlapped portion. Therefore, overlapping channels produce more smooth velocity profiles. The measuring window is defined as the section of ultrasound beam that accommodates all the channels. Thus, the window distance may be determined as follows:

$$W = (N_{ch} - 1) \times d_{ch} \quad (3.18)$$

Where W is the window distance and N_{ch} is the number of channels. Using equation 3.18, the end position of the window W_{end} becomes:

$$W_{end} = W_{start} + W = W_{start} + (N_{ch} - 1) \times d_{ch} \quad (3.19)$$

Where W_{start} is the start position of the window. This concept introduces the first measurement limitation, the maximum measurable depth P_{max} . The UVP-DUO system constrains the window end position to:

$$W_{end} < P_{max} \quad (3.20a)$$

$$W_{end\ max} = P_{max} - 2 \times d_{ch} \quad (3.20b)$$

Where $W_{end\ max}$ is the maximum window end position.

The objective of a UVP-DUO system is to detect the Doppler shift frequency at every channel along the ultrasound beam; in other words, it must identify precisely the echo signal coming from each measurement volume within the complete echo burst. The UVP-DUO Monitor software uses a time domain algorithm to establish the echo oncoming from each single channel, separately. Herein two measurement limitations show up: maximum

measurable depth P_{max} and maximum measurable velocity range V_{range} . The maximum measurable depth depends on the pulse repetition frequency F_{prf} . The pulse repetition frequency is defined as the frequency at which a UVP-DOU system sends a ultrasound pulse (see fig. 3.8). In principle, the system cannot shoot a new pulse until the echo from the last channel reaches the transducer. Thus, the maximum measurable depth becomes:

$$v = \frac{2P_{max}}{T_{prf}} \quad (3.21a)$$

$$v = 2P_{max}F_{prf} \quad (3.21b)$$

$$P_{max} = \frac{v}{2F_{prf}} \quad (3.21c)$$

Where v is sound velocity and T_{prf} is the time it takes a pulse to reach the last channel in addition to the time it takes its echo to reach the probe. Equation 3.21c shows that the larger pulse repetition frequency F_{prf} allows the system to reach a larger maximum measurable dept P_{max} . On the other hand, the maximum measurable velocity range V_{range} also depends on the pulse repetition frequency. According to the Nyquist sampling theorem, certain sample can be measured at minimum at "twice the highest frequency presented in the signal" in order to not introduce errors (Met-Flow SA, 2002). Thus, UVP-DUO limits the maximum detectable Doppler shift frequency to half of F_{prf} :

$$\Delta f_{max} = F_{prf}/2 \quad (3.22)$$

The maximum velocity range is equivalent to the absolute value of twice the maximum measurable particle velocity:

$$V_{range} = 2|v_{pmax}| \quad (3.23a)$$

$$V_{range} = 2 \left| \frac{v \Delta f_{max}}{2f} \right| \quad (\text{see eq. 3.16a}) \quad (3.23b)$$

$$V_{range} = 2 \left| \frac{v(F_{prf}/2)}{2f} \right| \quad (3.23c)$$

Because F_{prf} , f and v are positive, absolute value may be removed:

$$V_{range} = \frac{v F_{prf}}{2f} \quad (3.23d)$$

Combining equation 3.21c and 3.23d:

$$P_{max} V_{range} = \left(\frac{v}{2F_{prf}} \right) \left(\frac{v F_{prf}}{2f} \right) \quad (3.24a)$$

$$P_{max} V_{range} = \frac{v^2}{4f} \quad (3.24b)$$

$$V_{range} = \frac{v^2}{4f P_{max}} \quad (3.24c)$$

Note that V_{range} is inversely proportional to the emitted ultrasound frequency f and the maximum measurable depth. Furthermore, Met-Flow SA (2002) derives a formulation for velocity resolution ΔV in terms of maximum velocity range; which is defined as the least resolvable difference in velocity. Due to hardware capabilities, a digital signal processor only produces a fixed number of possible velocity values N_{DU} . UVP-DUO system works with 8-bit word digital signal processor. It implies that N_{DU} is equal to 256. Therefore, the velocity resolution ΔV becomes:

$$\Delta V = \frac{V_{range}}{N_{DU}} = \frac{V_{range}}{256} \quad (3.25)$$

In order to achieve more velocity resolution, the maximum velocity range V_{range} may be reduced by increasing the maximum measurable depth P_{max} .

UVP-DUO system computes the flow velocity by means of the Doppler shift frequency, characteristics of the ultrasound signal, and the transducer orientation with respect the flow. It produces continuously series of "raw data" as an internal output for Doppler shift frequency. In order to convert the raw data into actual frequency units, UVP-DUO Monitor software introduces a Doppler coefficient $C_{Doppler}$. Similar to the velocity resolution ΔV , the Doppler coefficient becomes the smallest measurable Doppler frequency difference:

$$C_{Doppler} = \frac{F_{prf}}{N_{DU}} \quad (3.26)$$

Where F_{prf} is pulse repetition frequency and N_{DU} is the number of possible values coming from a digital signal processor. Thus, the Doppler shift frequency Δf is computed as follows:

$$\Delta f = C_{Doppler} \times \text{raw data} \quad (3.27)$$

Further, sound coefficient C_{sound} is brought in to compute the flow velocity along the ultrasound beam. It is expressed in terms of the emitted ultrasound signal as follows:

$$C_{sound} = \frac{v}{2f} = \frac{\lambda}{2} \quad (3.28)$$

Velocity v_p along the beam becomes:

$$v_p = C_{sound} \times \Delta f \quad (3.29)$$

Finally, raw data may be converted into the flow velocity component of interest V (see fig.

3.9) according equation 3.30.

$$V = \text{raw data} \times C_{Doppler} \times C_{sound} \times \frac{1}{\sin \theta} \quad (3.30)$$

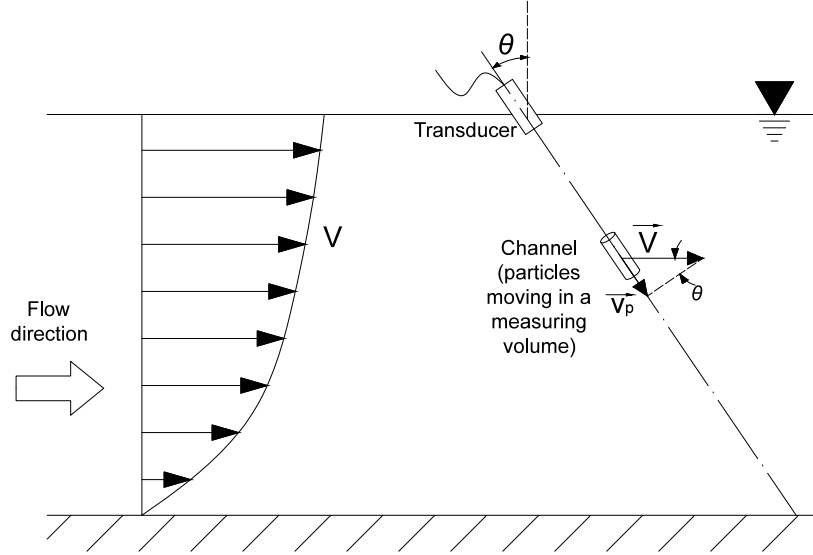


Figure 3.9: Illustration of a UVP-DUO system measuring velocity profiles in an open channel flow.

3.4 Experimental Setup

The objective of this experiment was to measure tangential and radial velocity profiles of flow in an annular flume. Thus, a further comparative analysis between measured data and the aforementioned mathematical formulation could be conducted. As result, conclusions could be developed regarding the applicability of such theoretical formulation on describing the velocity profiles in this flume.

The UVP-DUO system was used to measured the tangential and radial velocity profiles. Instead of using the integrated multiplex component, two $1MHz$ -transducers were attached into a 3D printed holder. The holder covered the sampling hole on the lid of the flume in order to bring continuity along the lid surface (see fig. 3.10). Also, the holder kept both

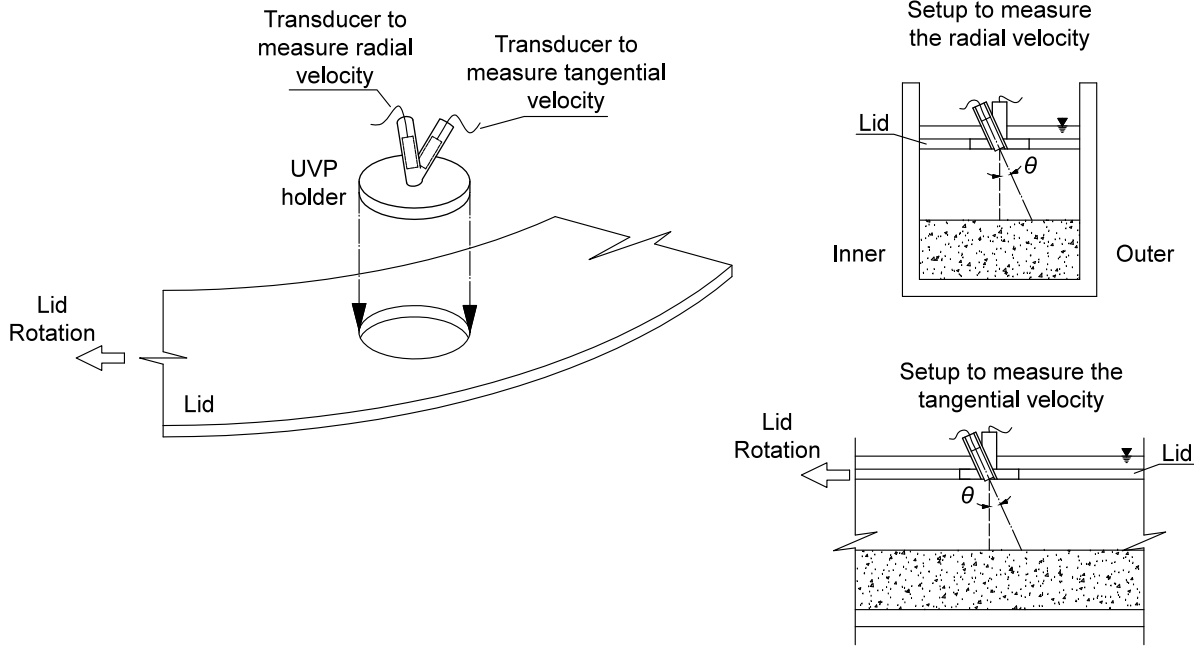


Figure 3.10: Ensemble of the UVP holder into the lid and transducer arrangements for measuring radial and tangential velocity profiles.

probes fixed and placed orthogonal between each other. One probe was placed to measure the tangential component of the flow, whilst the other measured the radial component. The angle θ for both transducers was 10° . The UVP-DUO unit was placed at the top wooden plate attached to the lid supporting frame. Because of the lid rotation, the UVP-DUO unit was conveniently connected to the remote control laptop via wifi. Thus, the unit and a router were fastened to the wooden plate with hook-and-loop fasteners and fabric buckle belts. In order to achieve flow depths shallower than 20cm (minimum depth of the annular flume), the bottom of the flume was raised, 15cm approximately, with ground walnut shells. Therefore, it was possible to set up 5cm of flow depth. Ground walnut shells had a mean grain size of 1.49mm . It would increase significantly the equivalent roughness height of the bottom; it was found to be smooth according to Waterman and Garcia (2014). Some minor bedload transport took place along the experiments. Even though no bedforms appeared, particular

precaution was taken on making flat the bottom periodically when it was necessary. Figure 3.11 presents the sketch of the experimental setup.

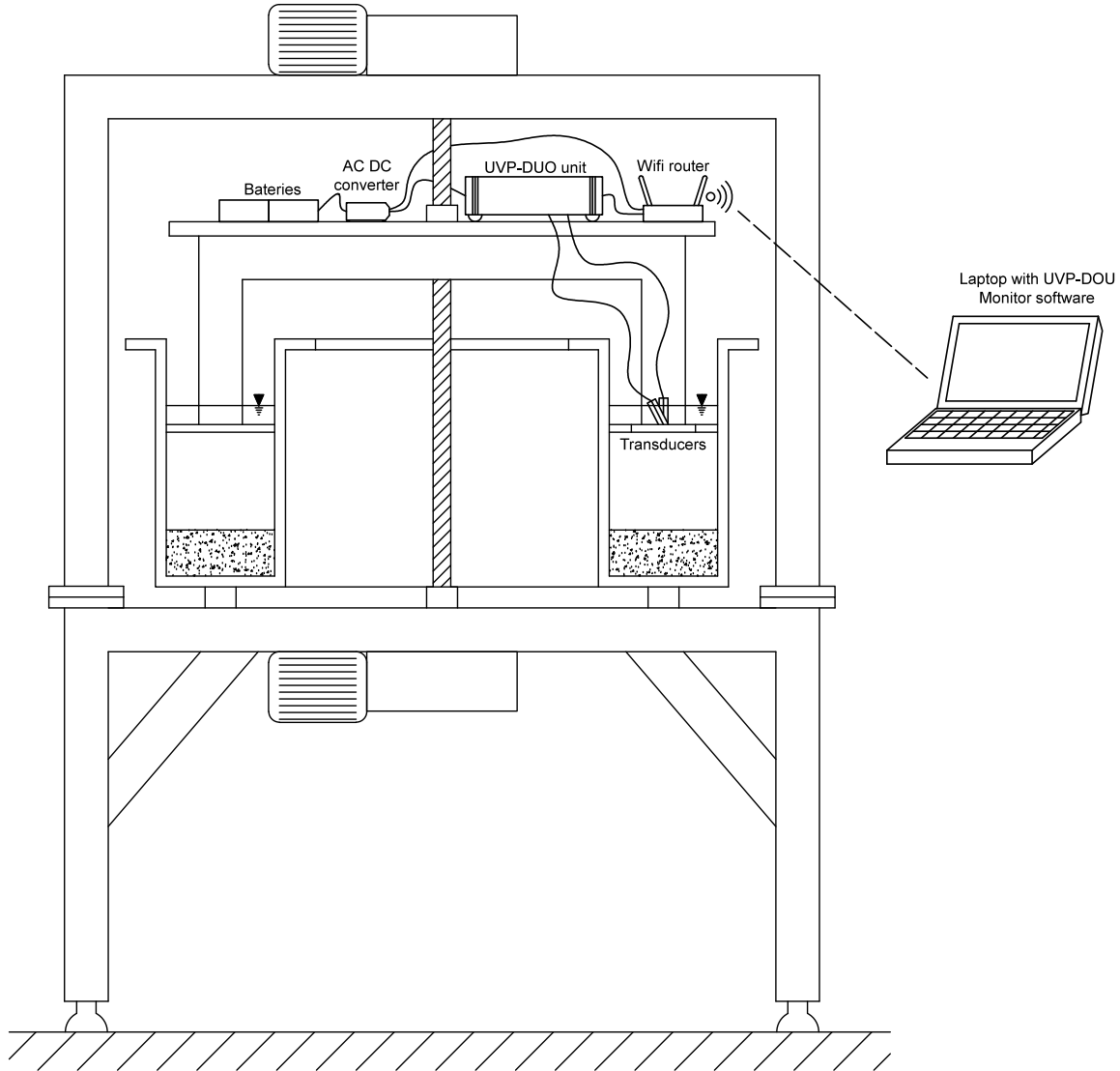


Figure 3.11: Sketch of the experimental setup.

This experiment assessed the tangential and radial velocity profiles under three water depth conditions (cases) and four speed of lid rotation (runs). In all cases the tank stayed stationary in order to compare the velocity profiles with the (Engelund, 1975) formulation. Annular flumes reach steady-state and uniform conditions fairly quick. In consequence, the

flow was considered uniform in the tangential direction ($\partial/\partial\theta = 0$). Therefore, a waiting period from 2 to 3 *min* took place after changing the lid rotation speed to let the flow reach equilibrium. 2,500 velocity profiles were measured for every single run for each velocity component; they were recorded at 58.82*Hz* frequency (every 17*ms*). The spatial resolution was $\Delta z = 1.465\text{mm}$; thus, 35, 69, and 103 points were measured along the water column for depths $h = 5\text{cm}$, 10*cm*, and 15*cm*, respectively. Tangential and radial velocity profiles were not measured simultaneously since the integrated multiplex component was not used. Table 3.1 presents the cases assessed in this experiment.

Table 3.1: Evaluated cases in the annular flume at Ven Te Chow Hydrosystem Laboratoy.

Case	Run	Water depth (cm)	Tank rotation (rpm)	Lid rotation (rpm)
1	A	5.0	0.0	0.5
	B	5.0	0.0	1.0
	C	5.0	0.0	2.0
	D	5.0	0.0	3.0
	E	5.0	0.0	4.0
2	A	10.0	0.0	0.5
	B	10.0	0.0	1.0
	C	10.0	0.0	2.0
	D	10.0	0.0	3.0
	E	10.0	0.0	4.0
3	A	15.0	0.0	0.5
	B	15.0	0.0	1.0
	C	15.0	0.0	2.0
	D	15.0	0.0	3.0
	E	15.0	0.0	4.0

3.5 Data Processing and Analysis

The purpose of this section is to present the data processing methodology used to obtain instantaneous velocity profiles from UVP-DUO raw data and hydrodynamic characteristics in the annular flume. A Matlab code was used to manage the binary file from the UVP-DUO. In order to describe the hydrodynamic behavior of the annular flume some turbulence statistics

were computed. Also, the methodology to compare the Engelund (1975) formulation with the measured profiles is presented.

3.5.1 Processing of raw data

To obtain more flexibility to manage the data from the UVP-DUO, a Matlab code was employed to convert the raw data into instantaneous velocities. Pedocchi (2005) provided, as an appendix in his Master's thesis, a script to read the UVP-DUO files and compute the velocity profiles. The code was slightly adapted to fit the needs of this experiment. For instance, equation 3.15e was changed considering that the transducer is no longer stationary for measurements of tangential velocity. Recalling that the UVP-DUO goes through two stages to detect the Doppler shift frequency. First, it plays the role of sound source emitting the ultrasound beam. Then, it changes into "listening" mode to detect the echo ultrasound from the moving particles. Velocity computation for tangential velocity profiles were adapted as follows:

$$f'_1 = \left(\frac{v + v_p}{v - v_t} \right) f \quad (3.31)$$

Where f is the emitting ultrasonic frequency, f'_1 is apparent Doppler frequency, v is sound velocity, v_p is particle velocity, and v_t is source velocity. Equation 3.31 expresses that the apparent frequency at the first stage will consider that the particle is the observer and the transducer and sound source. Thus, it is moving towards (positive sign) or away (negative sign) the observer with velocity v_t . At the listening stage, the transducer and the particle become the observer and the source, respectively. Therefore, the second apparent Doppler frequency f'_2 turns into:

$$f'_2 = \left(\frac{v + v_t}{v - v_p} \right) f'_1 \quad (3.32)$$

Replacing equation 3.31 into equation 3.32:

$$f'_2 = \left[\left(\frac{v + v_t}{v - v_p} \right) \left(\frac{v + v_p}{v - v_t} \right) \right] f \quad (3.33a)$$

$$f'_2 = \left[\left(\frac{v + v_t}{v - v_t} \right) \left(\frac{v + v_p}{v - v_p} \right) \right] f \quad (3.33b)$$

The UVP-DUO system defines and measures the Doppler shift frequency as the differences between the emitted ultrasound frequency and the detected echo frequency f'_2 . Thus, the adapted Doppler shift frequency becomes:

$$\Delta f = f'_2 - f \quad (3.34a)$$

$$\Delta f = \left[\left(\frac{v + v_t}{v - v_t} \right) \left(\frac{v + v_p}{v - v_p} \right) \right] f - f \quad (3.34b)$$

$$\Delta f = f \left[\frac{2v(v_t + v_p)}{(v - v_s)(v - v_p)} \right] \quad (3.34c)$$

Since sound velocity is significantly larger than particle and transducer velocity, both may be neglected from the denominator in equation 3.34c:

$$\Delta f = f \left[\frac{2v(v_t + v_p)}{v^2} \right] \quad (3.34d)$$

$$\Delta f = f \left[\frac{2(v_t + v_p)}{v} \right] \quad (3.34e)$$

Recall that the UVP-DUO system assumes that the transducer is stationary. Thus, it computes the Doppler shift frequency as follows (see eq. 3.15e):

$$\Delta f = \frac{2v_p}{v} f \quad (3.35)$$

Note that the system will detect an apparent particle velocity $v'_p = v_t + v_p$ when the transducer is moving with the lid:

$$\Delta f = \frac{2v'_p}{v} f = f \left[\frac{2(v_t + v_p)}{v} \right] \quad (3.36)$$

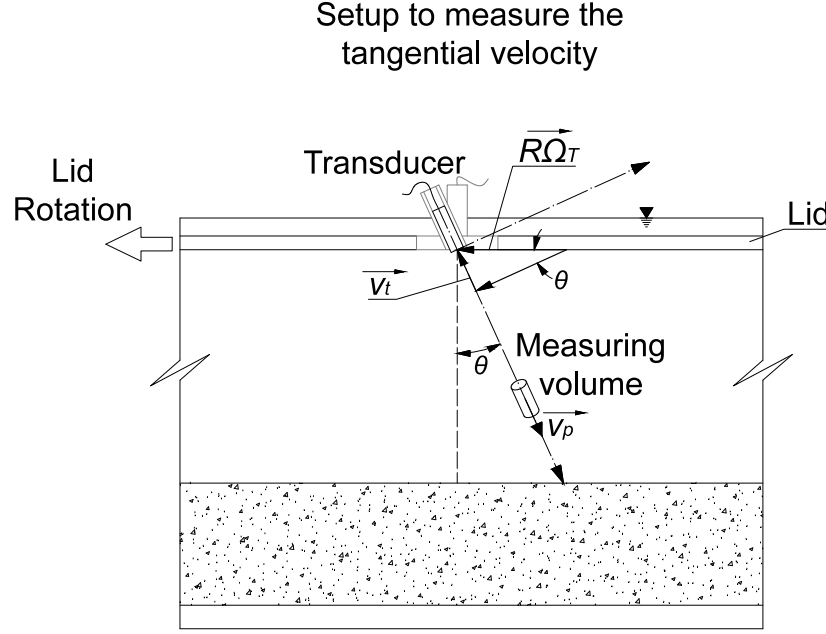


Figure 3.12: Velocity decomposition of moving transducer for tangential velocity measurements.

According to figure 3.12 the transducer will be moving away from the measuring volume. It implies that the apparent particle velocity v'_p is:

$$v'_p = v_p - v_t \quad (3.37)$$

Figure 3.12 also shows that transducer velocity with respect to the beam axis turns into:

$$v_t = R\Omega_T \cos \theta \quad (3.38)$$

Where R is the radial location of the transducer. On the other hand, no adaptation was

required for the radial velocity computations. It may be argued that the transducer moves with respect to the measuring volume. However, it may be considered stationary with respect to the velocity component of interest. The transducer velocity with respect to the measuring volume will be:

$$v_t = \frac{2(R\Omega_T)^2}{v} \quad (3.39)$$

Because the sound velocity is significantly larger than the lid rotation velocity $R\Omega_T \ll v$, the transducer velocity v_t may be neglected for radial velocity measurements.

3.5.2 Engelund's Formulation

Engelund (1975) proposed a mathematical formulation to compute directly the tangential and radial velocity profiles when the flow depth and lid rotation velocity are known. Because the secondary flow is a consequence of the centrifugal acceleration, it can be expected to be a function of tangential velocity magnitude. Therefore, Engelund's formulation claims that radial component of the flow is function of the computed tangential velocities.

Tangential Velocity Profile

The tangential velocity profile follows a logarithmic distribution and is computed according to the following equation (Engelund, 1975),

$$\frac{v_\theta}{u_*} = \frac{1}{\kappa} \ln \frac{\zeta}{1 - \zeta} + \frac{1}{\kappa} \ln \frac{30h}{k_B} \quad (3.40)$$

Where v_θ is tangential velocity, u_* is shear velocity, κ is Von Karman constant, h is flow depth, ζ is z/h , and k_B is equivalent roughness height of the bottom. Since the walnut shells used to rise the bottom of the flume were 1.49mm mean grain size, k_B was assumed to be equal to $2 \times 1.49mm = 2.98mm$.

Shear velocity was estimated following two methodologies: (i) fitting a log-law (see eq.

3.41a) to the lower 2 to 3cm of the measured tangential velocity profile, (ii) using the Engelund's formulation itself. From measured data, the vertical elevation z was graphed in a semi-logarithmic plot. Thus, the inverse of slope of a linear regression times the Von Karman constant became the shear velocity (see eq. 3.41c).

$$\frac{v_\theta}{u_*} = \frac{1}{\kappa} \ln \left(\frac{z}{z_0} \right) \quad (3.41a)$$

$$\frac{\kappa}{u_*} v_\theta = \ln(z) - \ln(z_0) \quad (3.41b)$$

$$\ln(z) = \frac{\kappa}{u_*} v_\theta + \ln(z_0) \quad (3.41c)$$

On the other hand, Engelund (1975) states that shear velocity can be computed directly when the lid rotation and its roughness are known:

$$\frac{r\Omega_T}{u_*} = \frac{1}{\kappa} \left(\ln \frac{30h}{k_T} + \ln \frac{30h}{k_B} \right) \quad (3.42)$$

Where Ω_T is the lid rotation velocity and k_T is the equivalent roughness height of the lid.

Radial Velocity Profile

Engelund (1975) pointed out that through equation 2.15 shear velocity and bed shear stress can be estimated by means of the tangential velocity. Equation 3.40 becomes:

$$f(\zeta) = \frac{v_\theta}{u_*} \quad (3.43)$$

Thus, the equation to compute the radial component of the flow is:

$$\frac{\kappa v_r}{u_*^2} = -\frac{h}{r} F(\zeta) - \frac{gh}{u_*^2} \frac{dh}{dr} \ln(1 - \zeta) + \frac{Ch}{u_*^2} \ln \frac{\zeta}{1 - \zeta} + C_1 \quad (3.44)$$

Where C_1 is an integration constant and F becomes:

$$F(\zeta) = \int_0^\zeta \frac{d\xi}{\xi(1-\xi)} \int_0^\xi f^2 d\xi \quad (3.45)$$

C and C_1 are defined by the boundary conditions:

$$C_1 = \frac{Ch}{u_*^2} \ln \frac{30h}{k_B} \quad (3.46a)$$

$$C = \frac{u_*^2}{r} \int_0^1 f^2(\zeta) d\zeta - g \frac{dh}{dr} \quad (3.46b)$$

Finally, the unknown piezometric gradient dh/dr was determined by Engelund (1975) assuming that the net radial flow at a certain r -location is zero:

$$\int_0^1 v_r d\zeta = 0 \quad (3.47)$$

For computational purposes, all integrals were solve numerically using the trapezoidal method. Also, Excel Solver was used to find the piezometric gradient that results on satisfying equation 3.47.

Chapter 4

Results and Discussions

4.1 Introduction

Mathematical models become an efficient tool to describe the behavior of systems in nature. Contrary to numerical models, the earlier provides direct solutions using either boundary or initial conditions. Thus, the variation in time and/or space of a physical property can be known through a single equation or a system of them. The purpose of this chapter is to compute radial and tangential velocity profiles using the Engelund's formulation (Engelund, 1975) and to compare them with profiles measured in the Ven Te Chow Annular Flume. It is intended to identify differences in order to validate the use of Engelud's formulation as a suitable model to represent the flow field in the Ven Te Chow Annular Flume. Because shear velocity is associated with bed shear stress, it becomes an important parameter for erosion and deposition experiments. Thus, shear velocity was estimated by fitting the lower part of the tangential profiles to a logarithmic distribution. Since Engelund's formulation provides a direct way to compute the shear velocity as function of the lid rotation velocity, they were compared with those estimated via the log-law. The chapter is organized in two sections: (i) the first one is devoted to analyze the measured and modeled tangential velocity profiles, and (ii) a second section will present the measured and computed velocity profiles in the radial direction.

4.2 Tangential Velocity Distribution

This section is divided into two major parts: (i) measured data, and (ii) Engelund's formulation. With the purpose of understanding the hydraulic behavior of the tangential velocity profiles in the Ven Te Chow Annular Flume, the first part will describe the measured velocity profiles. Then, the second part will contrast the measured data with the tangential velocity profiles from the Engelund's formulation. Some other parameters such as depth-averaged mean velocity and shear velocity will be addressed for measured and modeled values as well.

4.2.1 Measured Data

This subsection presents the measured mean velocity profiles of the tangential component. Results will be presented in three plots, one for each flow depth (cases). Therefore, every single graph will contain five mean velocity profiles, one for each lid rotation velocity. Also, shear velocity will be estimated by fitting the lower part of the profiles to a logarithmic distribution. Finally, other parameters such as Reynolds number and depth-averaged velocity are showed as function of the lid rotation velocity. The objective of this analysis is to understand the velocity distribution in the annular flume as function of flow depth and lid rotation.

Flow Depth $h = 5cm$

1. *Mean Velocity Profile*

Figure 4.1 presents the tangential mean velocity distribution for case 1 (flow depth equal to $5cm$). In general, all the profiles showed a common behavior. Within the first $5mm$, there is a monotonic increasing behavior. Then, a strong distortion appears in the profile at $z = 1cm$, approximately. The tangential mean velocity remains fairly uniform with slight increments up to the top. Since the velocity profiles remain uniform along the upper $4cm$, they became quite parallel by an offset equivalent to the difference

in lid rotation velocity. However, velocity profiles of $0.5rpm$ and $1rpm$ merge along the first centimeter. This significant distortion of the mean velocity profile may be due to the effect of the secondary flow and/or walls. Wall effects are reduced when the ratio flow depth to width is significantly smaller than one $h/B \ll 1$. In this case, $h = 5cm$ and $B = 20cm$; it yield a depth-to-width ratio of 0.25. Also, the hydraulic radius may indicate the strength of wall effects. For very wide channels, the hydraulic radius R_h tends to equal the flow depth h . However, the hydraulic radius in this case is $3.33cm$. So that, it differs by 33.4% from h . Falcon (1984) explains that when the secondary current is strong enough, it may interact with the velocity along the main flow. Also, he pointed out that for strong curved channels convective secondary velocity may play an important role. The ratio width-to-radius B/R may be a measured of the channel curvature. Weakly curved channels presents B/R significantly smaller than one. The Ven Te Chow annular flume has $B = 20cm$ and $R = 65cm$; it yields $B/R = 0.31$. Therefore, it can be argued that secondary flow may have a major influence on the velocity distribution of the tangential component.

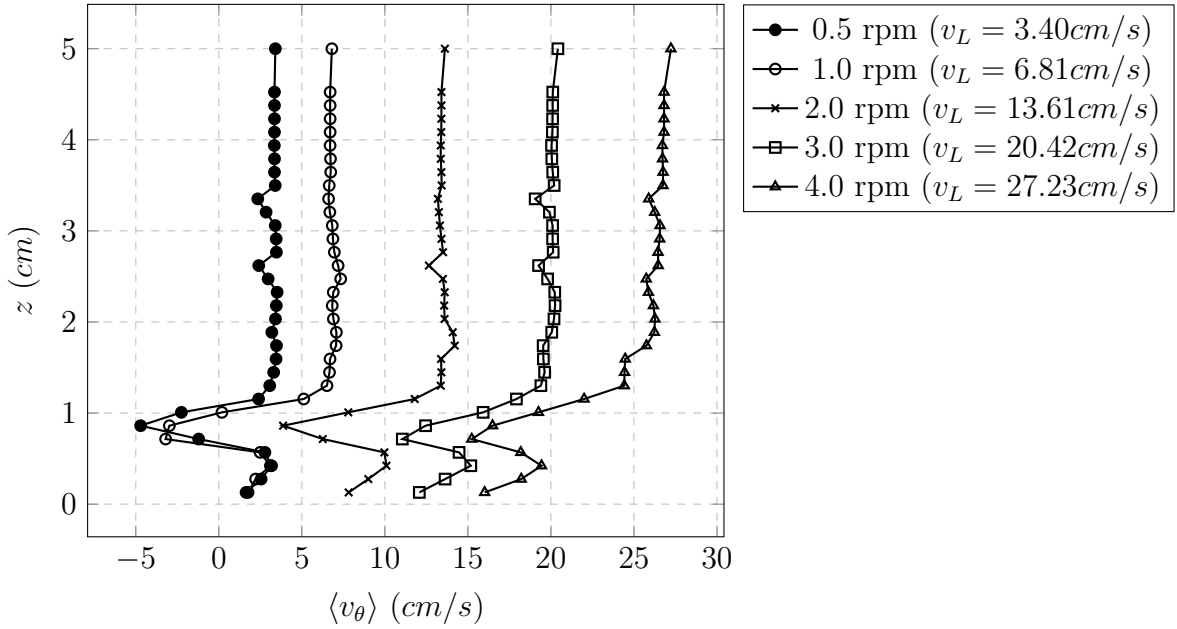


Figure 4.1: Mean tangential velocity profiles for flow depth $h = 5cm$.

2. Shear Velocity and Depth-averaged Mean Velocity

Shear velocity was estimated by fitting a logarithmic distribution along first centimeter of the velocity profile. According to M. Garcia (2008), the log-law distribution may be encountered over the lower 20% of the flow depth. The bias on the lower part of the velocity profile was ignore to fit the logarithmic distribution. There exists an apparent continuity of the velocity profile below and above the distortion in all flow conditions. Therefore, few points of the above-distortion profile were used to extend the logarithmic trend line. Figure 4.2 presents the variation of the shear velocity as function of the lid rotation velocity. Also, the same figure shows the power function that best fits the data; parameter R^2 was equal to 0.78. The shear velocity data looks more scattered for slow lid rotation than for faster revolutions. It may be argued that at slow lid rotation the net bulk momentum in the tangential direction can be easily affected by the secondary flow. On the other hand, figure 4.3 shows the variation of the depth-averaged mean velocity as function of lid rotation velocity as well. These values follow a more consistent monotonic tendency. A power function is also presented in the same figure.

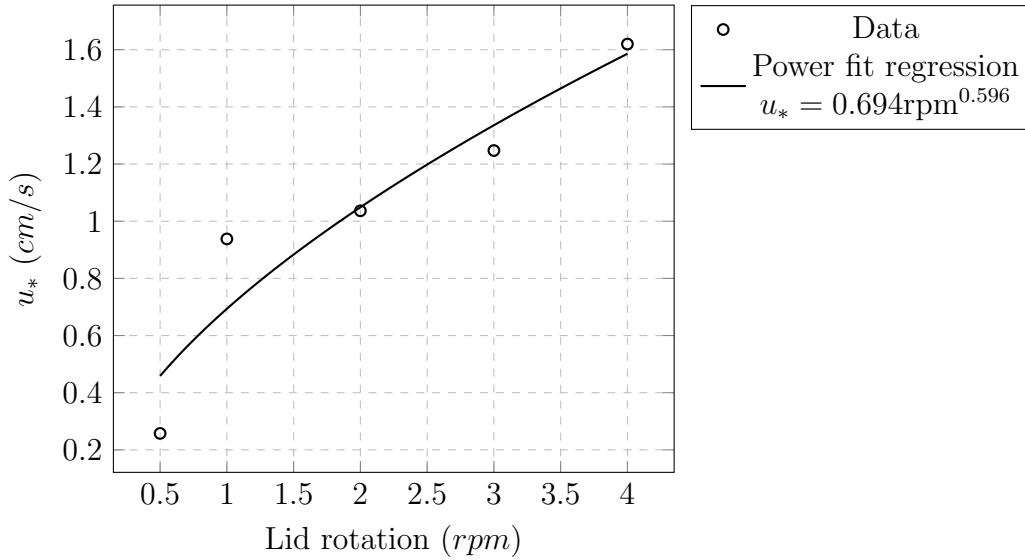


Figure 4.2: Shear velocity variation as function of lid rotation velocity for $h = 5cm$.

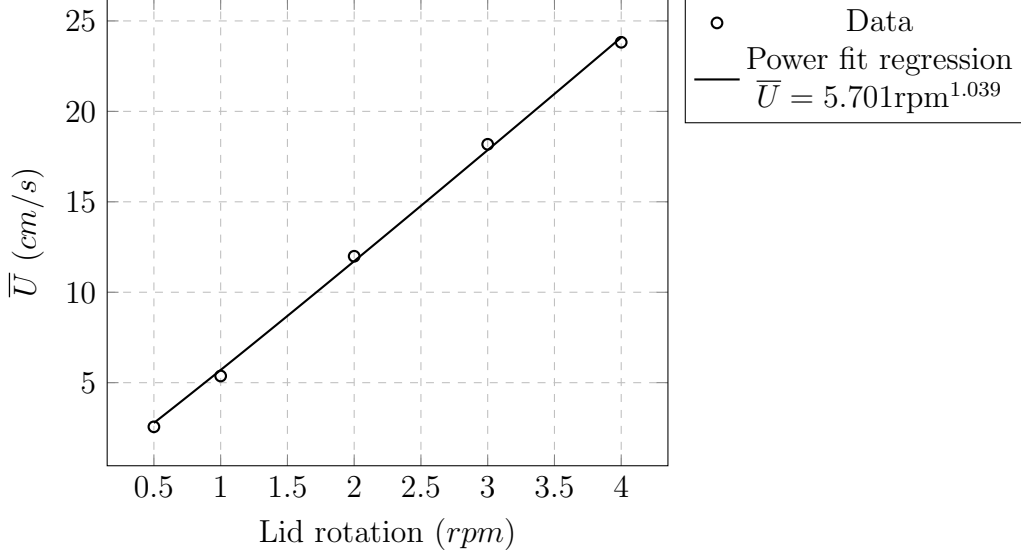


Figure 4.3: Depth-averaged mean velocity variation as function of lid rotation velocity for $h = 5cm$.

Flow Depth $h = 10cm$

1. Mean Velocity Profile

The structure of the mean velocity profiles for flow depth equal to $10cm$ were significantly different than those for flow depth equal to $5cm$ (see fig. 4.4). The earlier did not present any defined tendency. It suggests an important effect of the convective effects of the secondary currents on the main flow. Even though the profiles does not show a well-defined profile, a large deformation of the profile can be highlighted along $z = 1cm$ and $z = 6cm$. James et al. (1996), in a numerical and experimental study, stated that the interaction of secondary flow cells with the flow can be identified on tangential velocity distribution. Thus, it may be argued that the cell structure of the secondary flow for flow depth equal $10cm$ has a significant strength between $z = 6cm$ and $z = 1cm$. In addition to the secondary flow, wall effects in this case became more important than in the later. It was found that the hydraulic radius of this condition was equal to $5cm$; i.e. 50% of the actual flow depth. Lateral boundaries interacts with the main flow. Their effect becomes more notable over the middle section of the profile

because the top and lower boundaries have less influence.

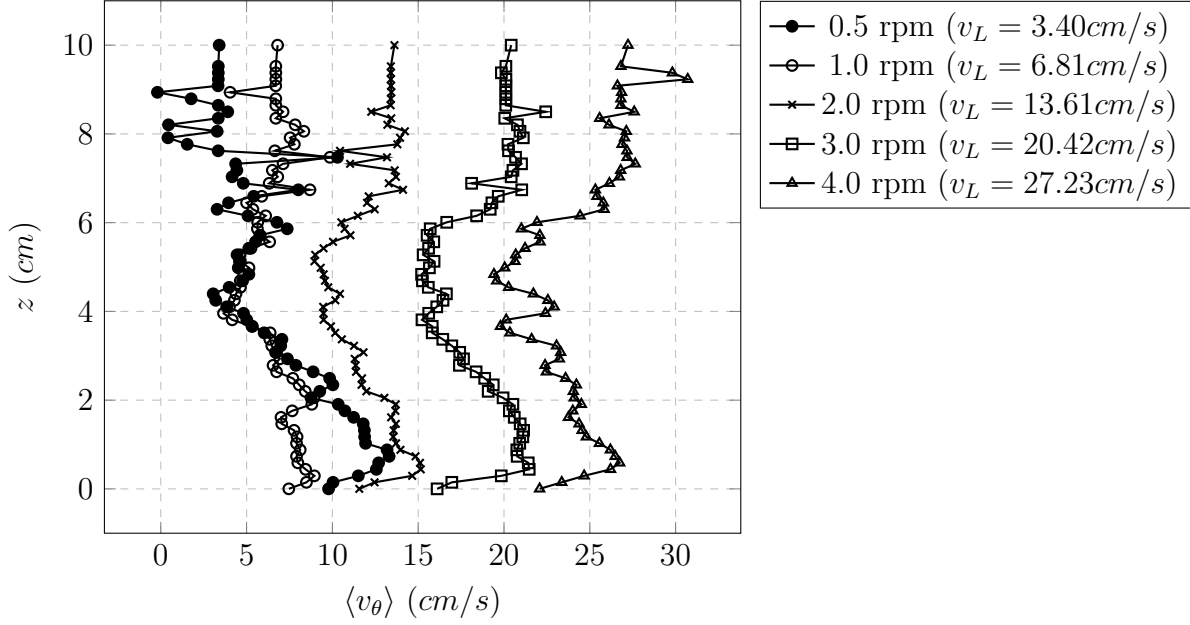


Figure 4.4: Mean tangential velocity profiles for flow depth $h = 10\text{cm}$.

2. Shear Velocity and Depth-averaged Mean Velocity

Figure 4.5 presents the variation of shear velocity as function of lid rotation when flow depth was equal to 10cm . In general, it illustrates that shear velocity increases with lid revolutions per minute. This behavior is expected because the faster the lid moves, the more momentum is transferred into the bottom through the water column. Different than the 5cm case, shear velocity data is considerably more scattered. Because of the great deformation of the mean velocity profile, it was difficult to define a neat logarithmic distribution even over the first centimeter. It was found that the u_* value was very sensitive to the number of data points used to fit the logarithmic distribution. Figure 4.5 also presents the best power function that fitted the series. It was found that R^2 was equal to 0.51. On the other hand, figure 4.6 shows the variation the depth-averaged mean velocity as function of lid rotation. The power function that fits this data set is presented in the same figure. Unlike the shear velocity series, the depth-averaged mean velocity shows a well-defined monotonic behavior. It also

increases with the lid rotation. Because the general shape of the mean velocity profile of the $0.5rpm$ -condition differs slightly from the rest of profiles, some scatter appear at lid rotation equal to $0.5rpm$.

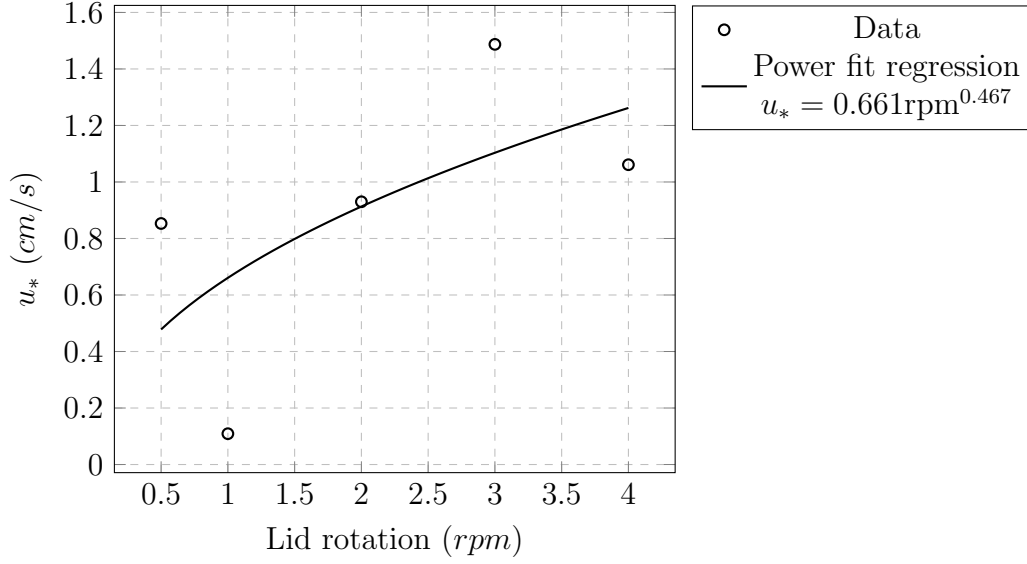


Figure 4.5: Shear velocity variation as function of lid rotation velocity for $h = 10cm$.

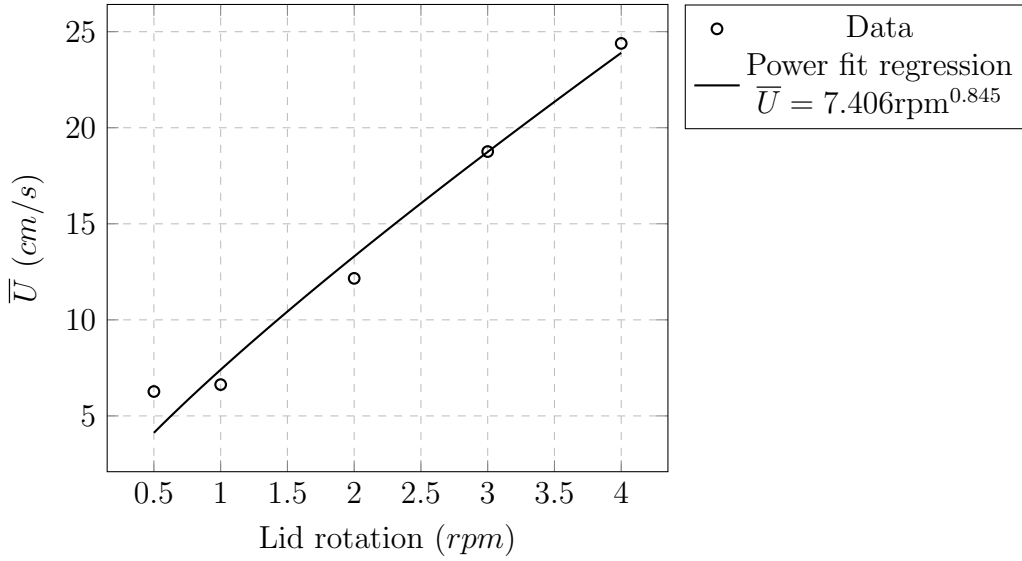


Figure 4.6: Depth-averaged mean velocity variation as function of lid rotation velocity for $h = 10cm$.

Flow Depth $h = 15cm$

1. *Mean Velocity Profile*

Mean velocity profiles are presented in figure 4.7. They show similar velocity distributions. In general, the lower part of the profiles presents a peak that is larger than the lid rotation velocity v_L . In a typical Couette flow, the maximum velocity is located at the moving plate. However, all the velocity profiles show that the maximum velocity is located at $z = 1cm$, approximately. Since the same peak was slightly perceived for flow depth equal to $10cm$ and not identified for a flow depth of $5cm$. It may be argued that the velocity structure of the profiles in figure 4.7 was better developed with the flow depth. Thus, the velocity profiles at $h = 10cm$ became a transitional stage between the profiles at $h = 5cm$ and $h = 15cm$. Note that a mirror behavior is presented at the upper part of the velocity profiles. It may be argued that it is due to the local effect of the vortex formed when the outward (downward) secondary flow at the top (along the outer wall) meets the outer wall (bottom); i.e. it may be caused by the change of flow direction at the corners of the cross section (see fig. 2.2a when the tank is stationary). Because the direction of the secondary flow along the top and bottom has opposite directions their convective effect on the main velocity profile is the opposite as well. Therefore, the convective effect of the secondary flow damps the tangential velocity at the top and increases the tangential velocity at the bottom. The behavior of the tangential velocity profiles agreed with those measured by Krishnappan (1993).

2. *Shear Velocity and Depth-averaged Mean Velocity*

Shear velocities of lid rotation for flow depth equal to $15cm$ are presented in figure 4.8. Because of the well-defined logarithmic distribution over the first centimeter of the velocity profiles, figure 4.8 illustrates a less scattered data set. There is increasing tendency of the series as function of the lid rotation. The same figure presents the best

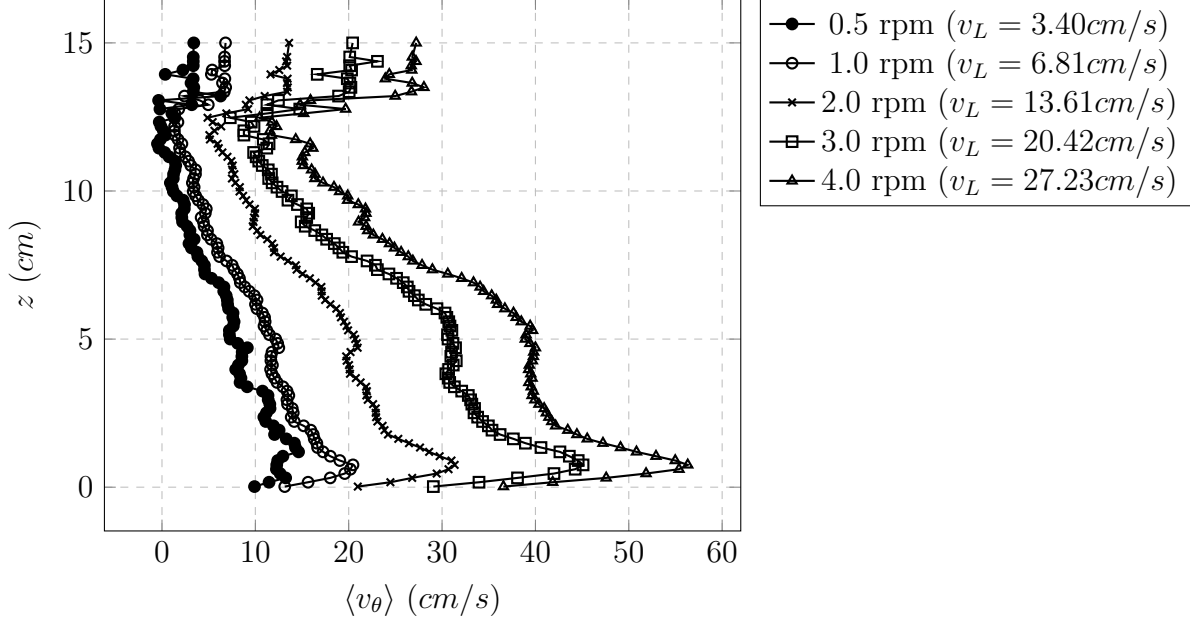


Figure 4.7: Mean tangential velocity profiles for flow depth $h = 15\text{cm}$.

power function that fits the estimated shear velocity. It was found that R^2 parameter was equal to 0.81. Similarly, it was found that depth-averaged mean velocity follows a power-law distribution without any significant scatter (see fig. 4.9). Note that \bar{U} becomes slightly larger than v_L in all lid rotation when flow depth is equal to 15cm . It may be argued that momentum transfer from the secondary flow into the main flow becomes significant.

In order to summarize the hydraulic parameters of the measured velocity distribution, figures 4.10 contrasts the shear velocity, depth-averaged mean velocity and Reynolds number, respectively, as functions of lid rotation velocity.

4.2.2 Engelund's formulation

This part will present the tangential velocity profiles computed using the Engelund's formulation. Measured and modeled values will be compared by means of their shear velocities and the complete velocity profiles. First, the shear velocity estimated by a logarithmic distribution and Engelund's formulation will be presented in a single plot as function of lid

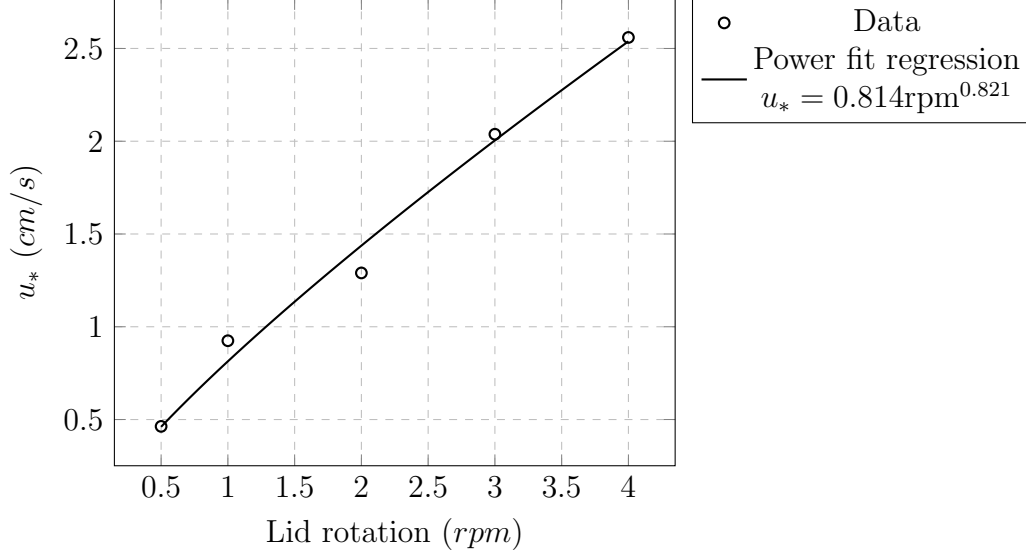


Figure 4.8: Shear velocity variation as function of lid rotation velocity for $h = 15cm$.

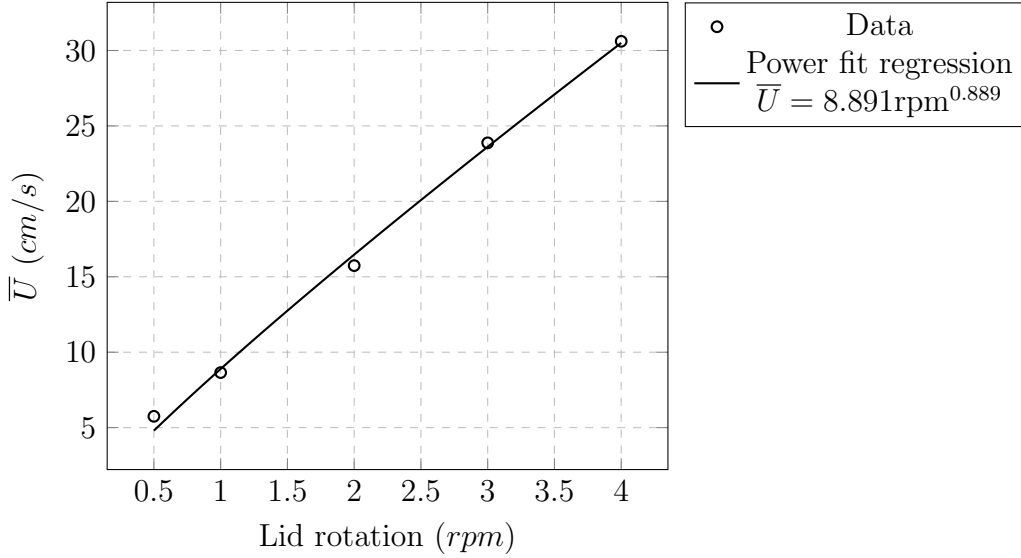
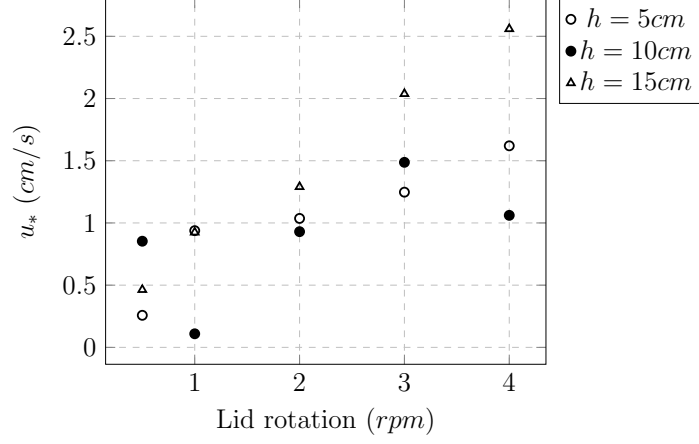
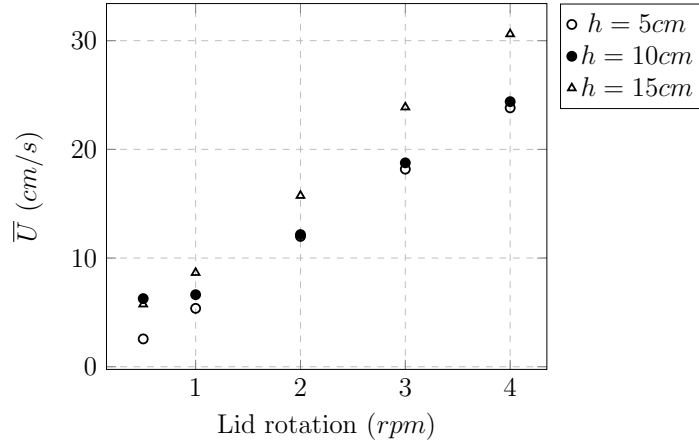


Figure 4.9: Depth-averaged mean velocity variation as function of lid rotation velocity for $h = 15cm$.

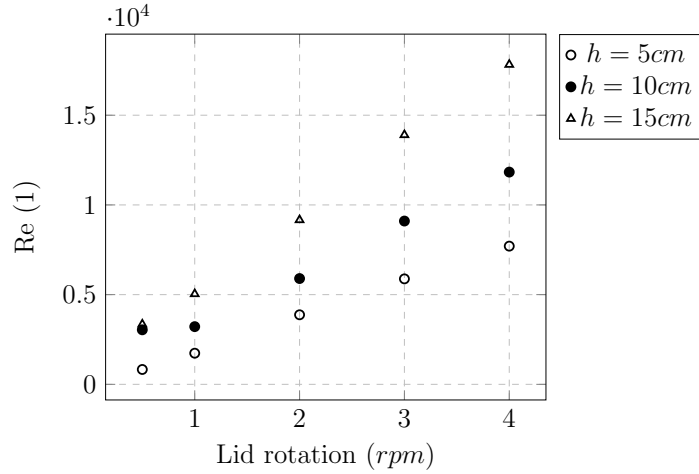
rotation and flow depth. Then, the complete set of 15 plots (one for each lid rotation and depth flow) will display the measured data along with modeled profiles. The Engelund's formulation is significantly sensible to the shear velocity. Therefore, a final analysis will show the measured and computed velocity profiles when the shear velocity was adjusted to obtain the best fit between them.



(a) Shear velocity as function of lid rotation for all flow depths.



(b) Depth-averaged mean velocity as function of lid rotation for all flow depths.



(c) Reynolds number as function of lid rotation for all flow depths.

Figure 4.10: Summary of hydraulic parameters of tangential velocity profiles as function of lid rotation for all flow depths.

Shear Velocity

Engelund (1975) provides a method to determine the shear velocity u_* directly. When the roughness of the lid and bottom are known, equation 4.1 is used to solve for u_* .

$$\frac{\Omega_L R}{u_*} = \frac{1}{\kappa} \left[\ln \left(\frac{30h}{k_L} \right) + \ln \left(\frac{30h}{k_T} \right) \right] \quad (4.1)$$

Where Ω_L is the angular velocity of the lid, R is the mean radius, κ is the Von Karman constant (0.41), h is flow depth, and k_L and k_T are the equivalent roughness height of the lid and bottom, respectively. Note that the flow is considered hydraulically rough at the lid and bottom. Herein k_L and k_T were assumed equal to twice D_{65} (M. Garcia, 2008). The characteristic grain size of the walnut shell was $1.49mm$. The lid did not have any granular surface; on the other hand, it was covered with square pieces of $4mm$ -thick foam in a staggered array in a previous study. As a rough approximation, k_L was assumed to be $2 \times 4mm = 8mm$.

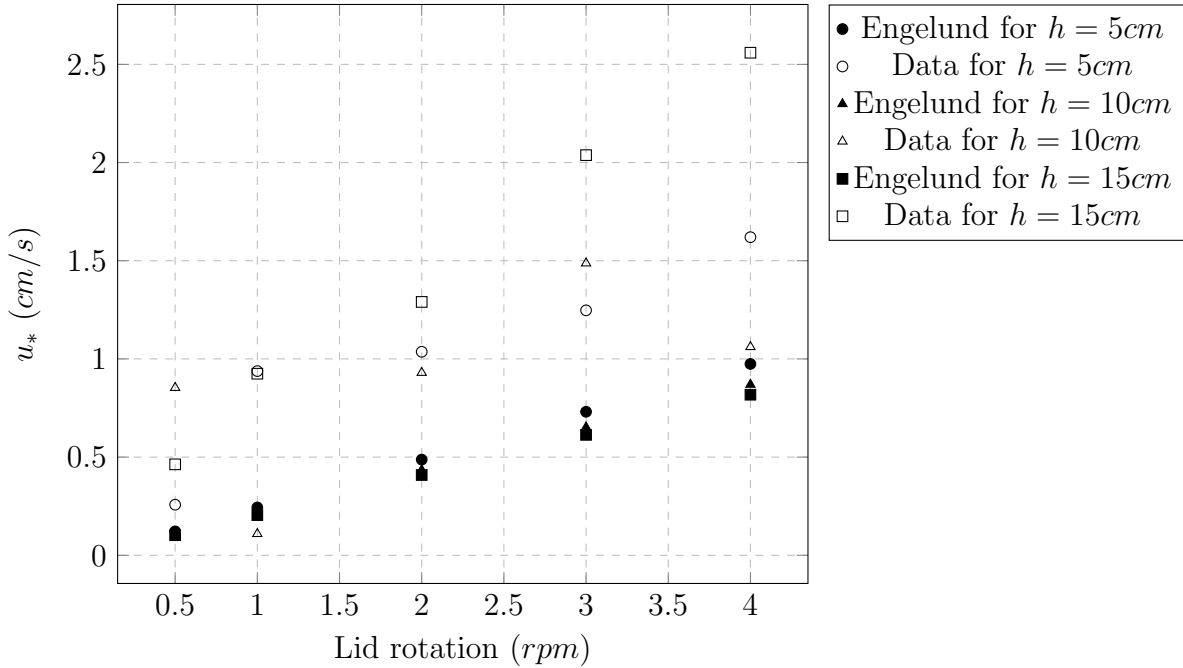


Figure 4.11: Shear velocity u_* estimated from data (log-law distribution) and according to Engelund (1975) formulation.

To assess the applicability of the Engelund's formulation in the Ven Te Chow Annular Flume, the shear velocity was computed for all measured cases using equation 4.1. Then, they were compared with those estimated from measured data. Shear velocity becomes an important parameter to evaluate because it is associated with the capacity transport of the flow. Figure 4.11 presents the values of shear velocity computed with equation 4.1, labeled as "Engelund", and those estimated by fitting a logarithmic distribution to the measured data.

Shear velocity obtained from Engelund's formulation increases with lid rotation velocity and decreases with flow depth. Typically, shear velocity is proportional to the characteristic velocity of the flow. For instance, it becomes proportional to the depth-averaged mean velocity. Because lid rotation is the driving mechanism of the flow, it is expected to obtain a proportional relationship between shear velocity and lid rotation velocity. Engelund (1975) also explains that the shear stress applied by the lid is transferred through the water column without change. Bed shear stress is associated with the square of shear velocity by the fluid density. Thus, shear velocity through a direct proportionality to the lid rotation velocity. The inverse behavior of shear velocity with respect to flow depth may be understood through the definition of shear stress as well. For Newtonian fluids, shear stress is proportional to the vertical velocity gradient $\partial v_\theta / \partial z$ through the dynamic viscosity μ or the eddy viscosity ε . When velocity boundary conditions remains ($v_\theta(0) = 0$ and $v_\theta(h) = \Omega_L R$) but flow depth increases, the vertical velocity gradients decreases. If $\partial v_\theta / \partial z$ becomes smaller, the shear stress would decrease as well. Therefore, Engelund's formulation computes larger shear velocity with shallower flow depth.

Two major differences were found comparing shear velocity from measured data with those computed with Engelund's formulation: (i) all measured values are larger than those from Engelund's; and (ii) shear velocity estimated from measured data showed an increase with flow depth. Tangential flow is significantly affected by the radial component of the velocity. Falcon (1984) stresses that channel curvature determines the interaction of main

and secondary flow. According to him, the Ven Te Chow Annular Flume may be classified as a strong curved flume because the ration width-to-radius is not much smaller than one. It implies that convective terms, neglected in the simplified dynamic equation, in the full Navier-Stokes equations become important. In other words, the transfer of momentum from the secondary velocities turn to be important and cannot be neglected. Unlike the shear velocity from Engelund's formulation, measured shear velocity increases with water depth. It may be argued that the secondary flow becomes stronger for a larger flow depth because it provides more length to develop the flow. Thus, its interaction with the main flow would be more significant for deeper flows. Booij (1994) found the secondary flow became stronger with larger flow depths. His objective was to minimize the secondary flow intensity by rotating the tank. Booij (1994) pointed out that the ration lid rotation velocity to tank rotation velocity was larger for shallower flow depths.

Mean Velocity Profiles

The objective of this part is to analyze the Engelund's formulation by comparing its mean velocity estimations with measured data. Therefore, measured data will be contrasted with mean velocity profiles computed with Engelund's formulation. To obtain a better agreement between measured values and estimated velocity profiles, a minimum square error adjustment was conducted by changing the shear velocity. Then, a discussion is presented comparing the new velocity profiles and shear velocity with the measured ones.

1. *Using shear velocity from Engelund's formulation*

Figure 4.12 shows the measured velocity profiles along with those estimated using Engelund's formulation. It was found that the Engelund's formulation underestimates the mean velocity profile in all cases. In general, the tangential velocity is notable underestimated over the water column for flow depths equal to 5cm and 10cm. In cases of $h = 15cm$, there is overestimation of the profile over the upper 5cm. Engelund's formulation is sensitive to values of shear velocity. Also, it was found that measured

shear velocities differ largely with shear velocity estimated using Engelund's formulation. Equivalent roughness height k_L and k_T are unknowns to be calibrated. However, Engelund (1975) stated that the velocity profile is not significantly sensible to those values because of the slow variation rate of the logarithmic profile at the boundaries. This behavior supports the idea that the tangential velocity in the Ven Te Chow Annular Flume is highly affected by the secondary flow. Therefore, Engelund's formulation does not represent correctly its tangential velocity profiles. However, some similarity with few measured cases can be observed.

Flow depth that better followed the Engelund's formulation was $h = 5cm$. One of the assumptions of this formulation is that the ratio flow depth to channel width must be significantly smaller than 1. It is clear that such conditions is not satisfied with $h = 5cm$, but it yields the smallest depth-to-width ratio. It is notable that all cases with of $h = 5cm$ show some similarity with the velocity profiles computed using Engelund's formulation. Even though the formulation underestimates the velocity values, the general structure of the profile slightly agrees with the measured data. It shows that Engelund's formulation potentially may represent tangential velocity profiles in laboratory facilities when its assumptions are considered in the experimental setup. In contrast, when $h = 10cm$ and $h = 15cm$ the velocity structure was completely different than the "S"-shape curve describe by the Engelund's formulation. Measured data shows how the secondary flow influence increases with lid rotation velocity and flow depth. For instance, velocity profiles at $h = 10cm$ can be seen as a transition between the well-defined velocity structures at $h = 5cm$ and $h = 10cm$. Despite some negative values of velocity at $h = 5cm$ and lid rotation velocity equal to $0.5rpm$, this case is the best profile that follows the Engelund's formulation.

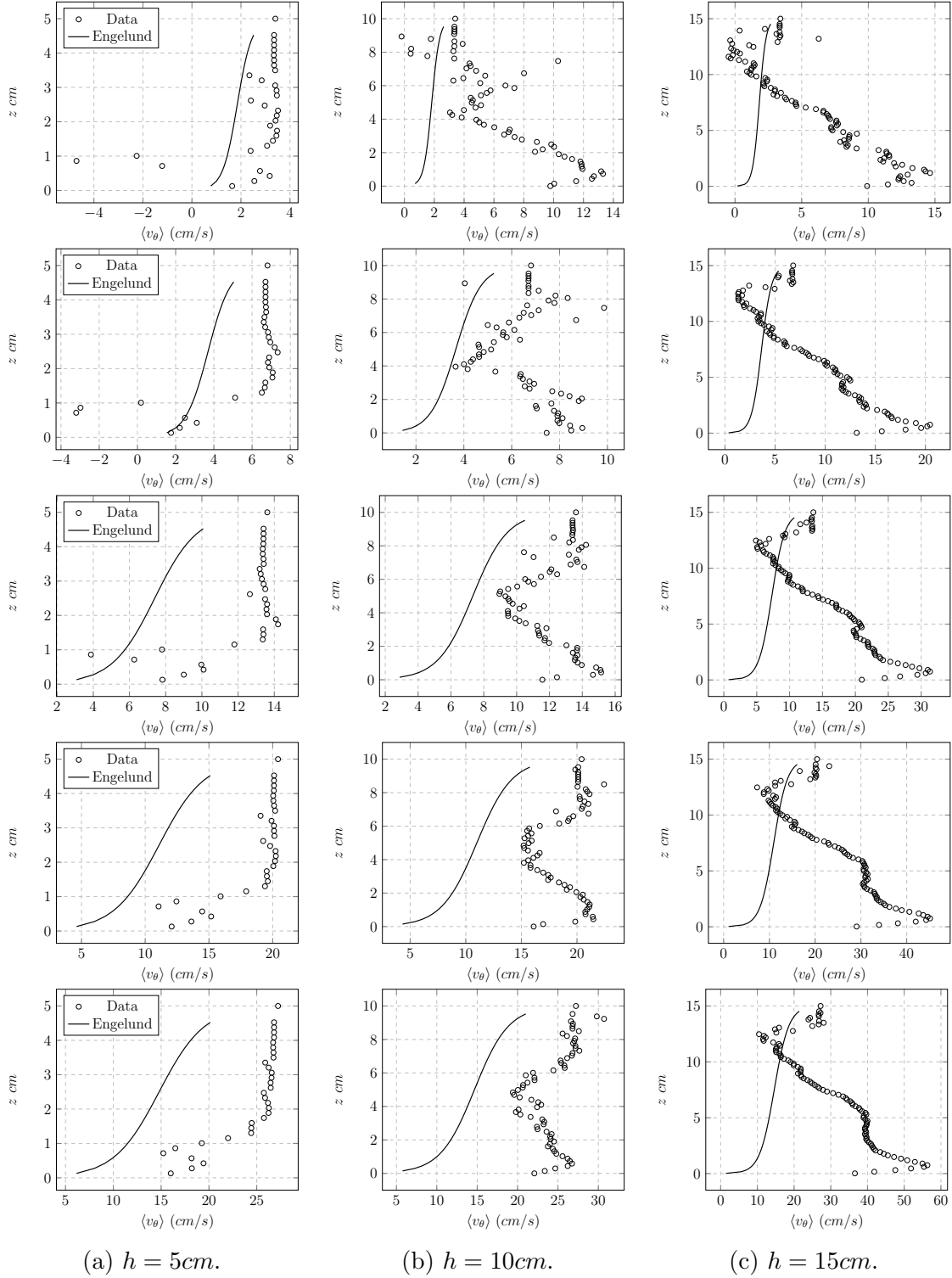


Figure 4.12: Modeled and measured tangential velocity profiles for all flow conditions. Cases (flow depth) were organized by columns and lid rotation velocity were 0.5, 1, 2, 3, and 4 rpm from top to bottom.

Table 4.1: Shear velocity from measured data, Engelund’s formulation, and adjusted by minimum squared error.

Lid Rotation	5 cm			10 cm			15 cm		
rpm	u_* Data [cm/s]	u_* Eng. [cm/s]	u_* Adj. [cm/s]	u_* Data [cm/s]	u_* Eng. [cm/s]	u_* Adj. [cm/s]	u_* Data [cm/s]	u_* Eng. [cm/s]	u_* Adj. [cm/s]
0.5	0.26	0.12	0.18	0.85	0.11	0.33	0.46	0.10	0.27
1	0.94	0.24	0.37	0.11	0.22	0.37	0.92	0.20	0.42
2	1.04	0.49	0.81	0.93	0.43	0.69	1.29	0.41	0.78
3	1.25	0.73	1.23	1.49	0.65	1.08	2.04	0.61	1.20
4	1.62	0.97	1.61	1.06	0.87	1.41	2.56	0.82	1.55

2. Adjusting shear velocity from Engelund’s formulation

With the purpose of obtaining a better fitting between the Engelund’s formulation and the measured data, the shear velocity was varied to minimize their sum of squared errors. Thus, both series may be contrasted in order to understand the effect of shear velocity on their agreement. Table 4.1 presents the shear velocity estimated from data (u_* Data), those computed from equation 4.1 (u_* Eng.), and the adjusted ones (u_* Adj.). All adjusted shear velocities became larger than those originally computed with Engelund’s formulation. They are more similar to those estimated from measured data. However, adjusted shear velocities are still lower than the measured ones. It was found that this adjustment resulted on unrealistic values of equivalent roughness height k_L .

Because of the similarity of the measured data for $h = 5\text{cm}$ with Engelund’s formulation, figure 4.13 shows the data along with the Engelund’s profiles using the new adjusted shear velocities. In general, all profiles present a better agreement with the data than those computed using the originally shear velocities. They tend to fit the data better over the lower part of the profile; the upper part of the profiles is overestimated by the Engelund’s formulation. It is because data points along the upper part follows a quite uniform behavior rather than a logarithmic trend. It may be argued that even though the new shear velocities are more similar to the those estimated from

measured data, Engelund's formulation still cannot represent the tangential velocity profile completely.

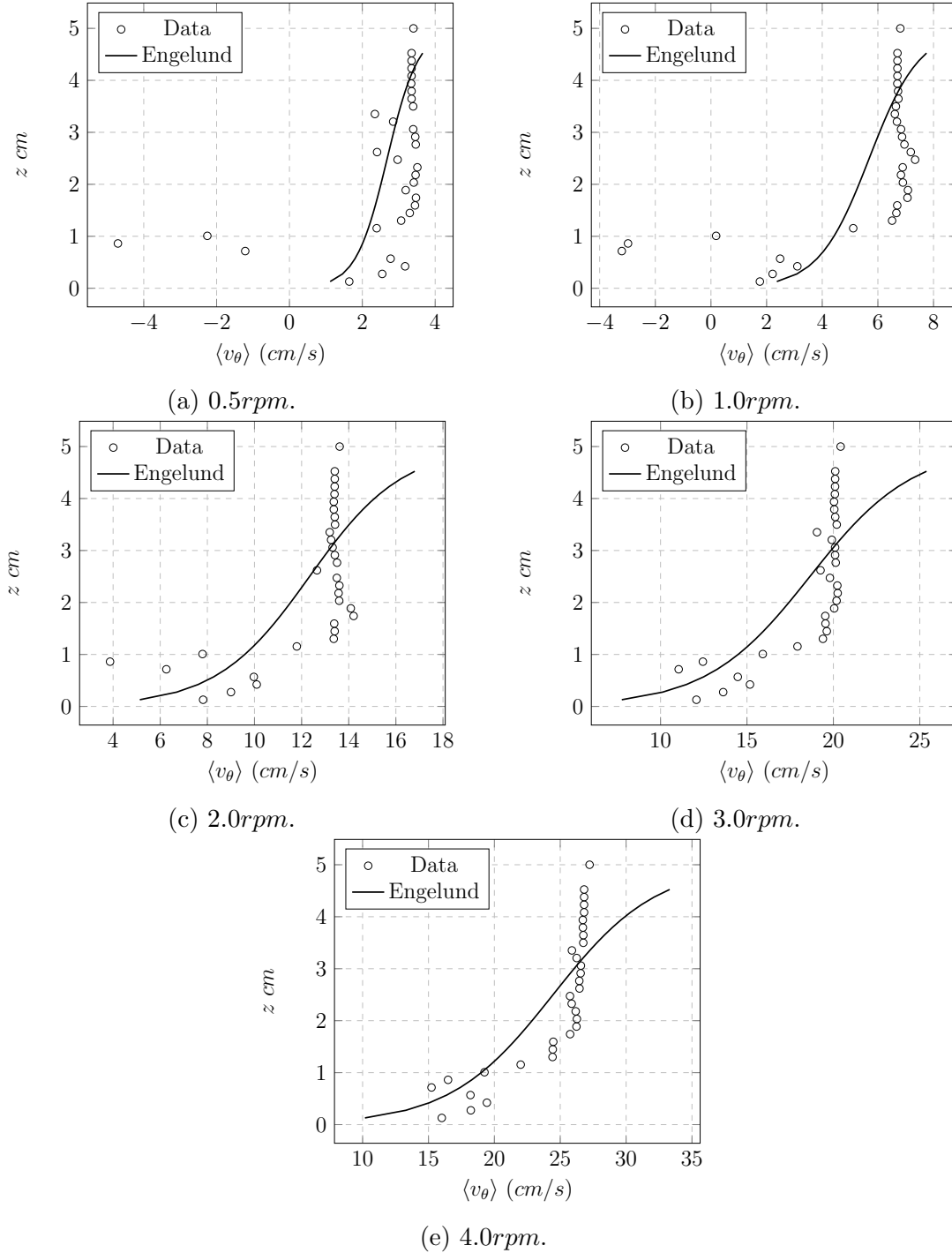


Figure 4.13: Measured data along with tangential velocity profiles using Engelund's formulation and adjusted shear velocity $h = 5cm$.

4.3 Radial Velocity Distribution

This section is divided also into two major parts: (i) measured data, and (ii) Engelund's formulation. They will address the measured and computed radial profiles. The radial component along with the vertical component of the flow constitute the so called secondary flow. Ideally, the vertical component would be significantly smaller compared with radial velocity at the center r -location of a very wide and weakly curved flow. Since Engelund's formulation solves for the tangential and radial component of the flow, radial measurements were taken with the UVP-DUO. The objective of this section was to conduct a comparative analysis of the radial velocity profiles computed with Engelund's formulation and the measured data in the Ven Te Chow Annular Flume.

4.3.1 Measured Data

This part will present the measured mean velocity profiles of the radial component. Because of the shape of the velocity profiles, it was not possible to present all the 5 profiles for each flow depth in a single plot. Therefore, the measured data for each lid rotation and flow depth are presented in individual graphs. Unlike the tangential profiles, no shear velocity could be estimated from measured data.

Flow depth $h = 5cm$

Figure 4.14 presents the measured velocity profiles for lid rotation velocity equals to $0.5rpm$ to $4.0rpm$ and flow depth $h = 5cm$. According to the transducer orientation, negative velocity indicates that the flow goes towards the inner wall of the flume. Figure 4.14 shows that the radial velocity becomes more negative as the profile approaches the bottom. In general, the velocity magnitude enlarges with depth; i.e. the secondary flow becomes stronger close to the bottom. It is expected to observe positive values of radial velocity at the upper part of the profile and negative values at the lower part. However, that was not entirely

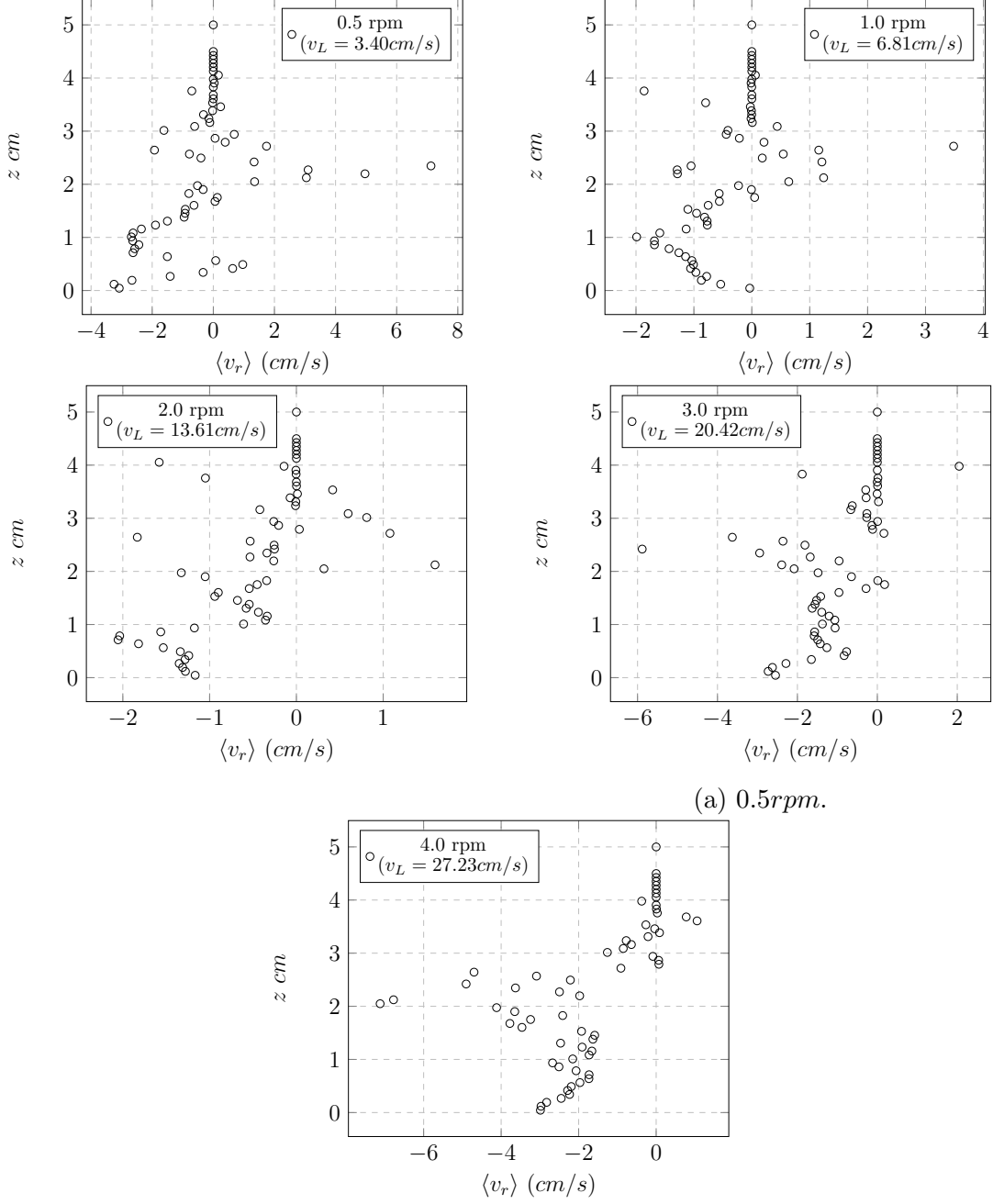


Figure 4.14: Mean radial velocity profiles for flow depth $h = 5\text{ cm}$.

the behavior showed in figure 4.14. Studies like Krishnappan and Engel (2004) have shown that at low rotation velocity of the tank the cell formed by the lid tends to be located asymmetrically to the outer part of the cross section for a similar h/B ratio. It may be argued that the center of the secondary cell is not located at the center of the cross section

(where the transducers were placed). The same study showed that the extension of the cell over the cross section depends on the magnitude and relative rotation of the lid and tank. Also, it may be argued that the dominant direction of the flow at the upper part of the profile was vertically upwards; recall that the secondary flow is formed by a vertical and radial components (Falcon, 1984) and only the radial component was measured. Centrifugal acceleration is proportional to the tangential velocity. Thus, it may be argued that a slower lid rotation velocity produces a weaker centrifugal acceleration. Once the secondary flow is established, it will encounter more resistance to convey water inwards proportionally to the flow depth (by means of the pressure force). It causes the center of the cell to be located at the outer part of the cross-section if the secondary flow is not strong enough to overcome the pressure force over the inner part of the cross section.

Flow depth $h = 10cm$

Figure 4.15 presents the radial velocity profiles when the flow depth was $10cm$. Unlike the cases of $h = 5cm$, radial velocity became positive in almost all the cases of $h = 10cm$. Only, the velocity profile with lid velocity rotation equal to $4.0rpm$ showed negative values at the lower part of the profile and a significant reduction of the largest positive velocity. They may be seen as a progressive evolution of the secondary flow as the lid rotation velocity became faster. In general, the largest radial velocity is found at $z = 8cm$ and it decreases with vertical elevation. It was found that the largest velocity of each profile also increases with lid rotation velocity. However, it was found that the velocity near the bottom decreased proportionally inverse with lid rotation velocity. It suggests that the secondary cell is capable to influence further inwards in the flow as the lid velocity becomes faster. It means that the cell formed by the secondary flow became more extended over the cross-section of the flume than in the cases when $h = 5cm$. Since the center of the secondary cell takes place in the outer part of the cross section, its influence further inwards is observed as the radial velocity turns into more negative values as the lid rotation velocity increases. Thus, the

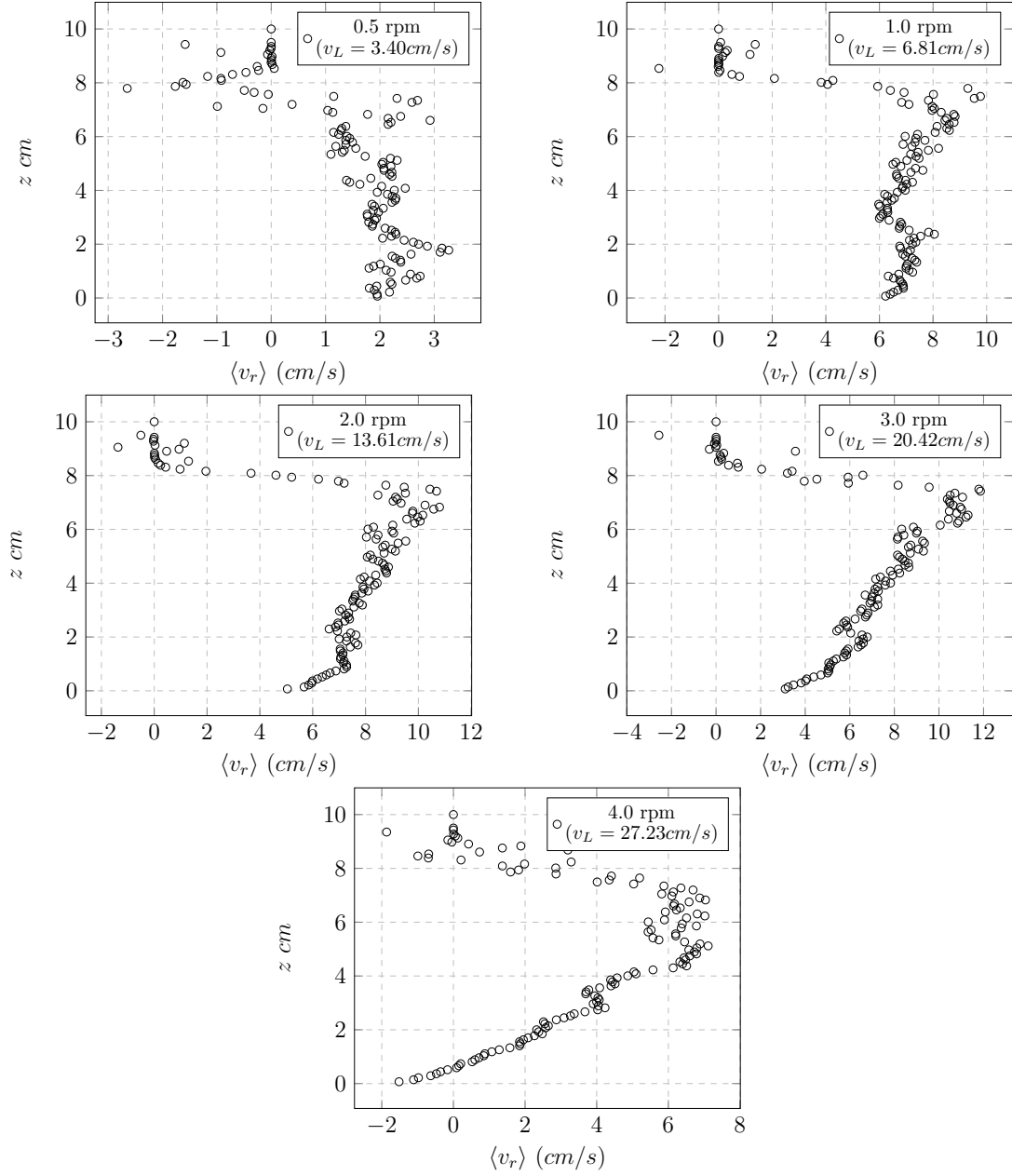


Figure 4.15: Mean radial velocity profiles for flow depth $h = 10$ cm.

radial profile at 4.0 rpm showed two structures for a typical secondary flow in a curved flow: outward velocities at the upper part and inward velocities at the lower part.

Flow depth $h = 15cm$

Radial velocity profiles of $h = 15cm$ are found in figure 4.15. Velocity profiles of $1.0rpm$ to $4.0rpm$ showed a well-defined velocity profile. The $0.5rpm$ -case was more scattered than the rest of profiles. However, a similar tendency can be vaguely identified with the rest of the profiles: the largest positive velocity is located near the lid and it decreases with elevation. It was the same pattern shown in all cases of $h = 10cm$. It is remarkable that most of the velocity values and their distribution are similar to those with $h = 10cm$. Thus, these velocity profiles support the idea that the secondary cell becomes more extended over the cross section as the lid rotation velocity increases. Note that the flow structure turns into outward at the upper profile and inward at the lower part at lid rotation equal to $4.0rpm$, similar to the same case but with $h = 10cm$.

4.3.2 Engelund's formulation

Figure 4.17 presents measured data along with the radial velocity profile estimated with Engelund's formulation. In general, it was found that the velocity profiles computed with Engelund's formulation fitted better the measured data for $h = 5cm$. However, the formulation overestimated positive (outward) part of the secondary flow. Regarding the rest of flow conditions, there was not a consistent over or underestimation pattern. For instance, the positive part of the profile is underestimated for lid rotation velocity $0.5rpm$ to $3.0rpm$ when $h = 10cm$. However, it is overestimated for $4.0rpm$ when $h = 10cm$. The Engelund's formulation considers that the cell is well extended over the entire cross section. Thus, it assumes that the net flow at a certain r -location is zero. However, this is not the case when the secondary cell is located towards the outer part of the cross section. Because the Ven Te Chow Annular Flume is a strong curved channel and its flow depth to width ratio was not significantly smaller than one, there is a strong interaction between the main and secondary flow. On the other hand, deeper flow depths may impose more resistance to the

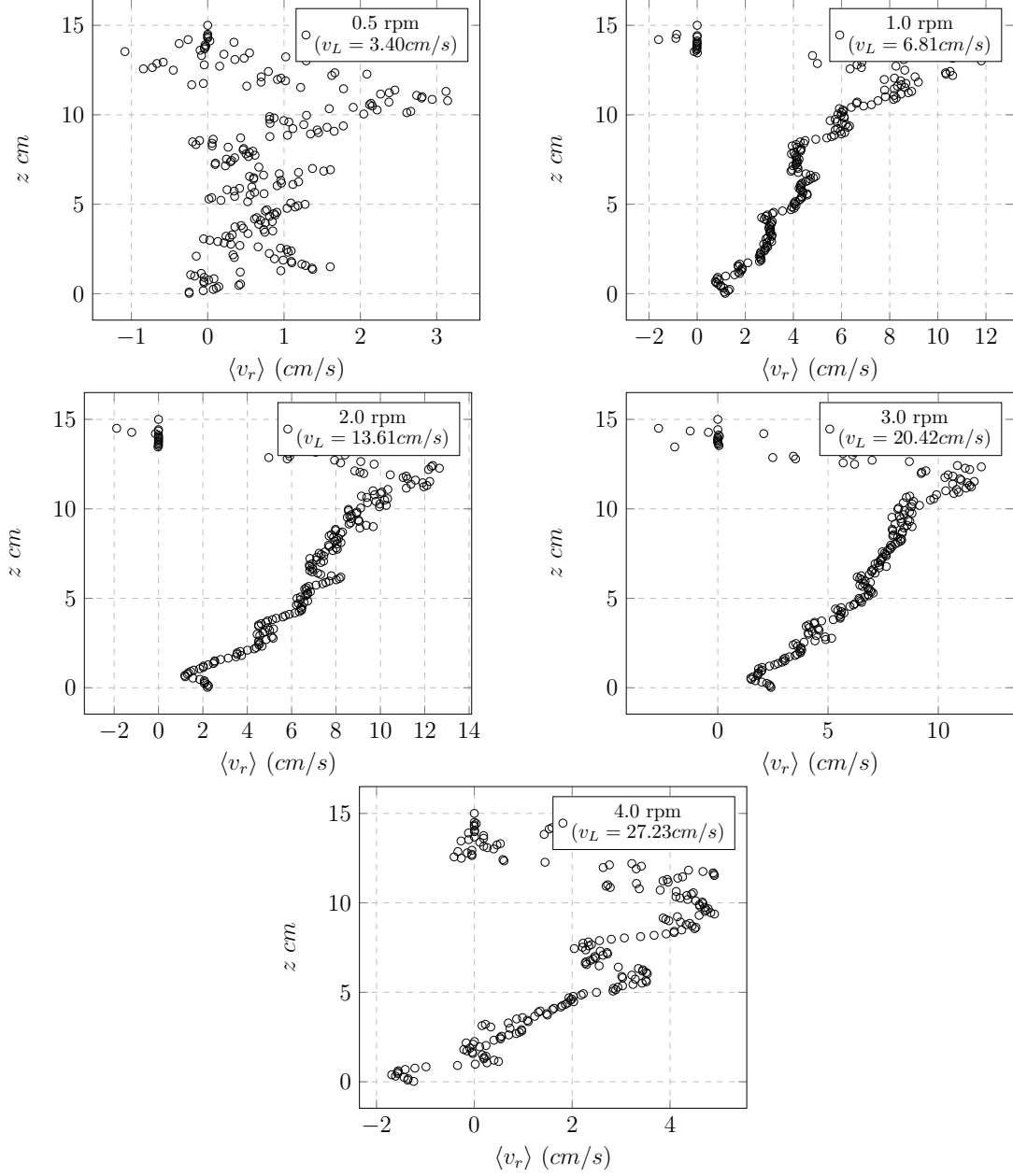


Figure 4.16: Mean radial velocity profiles for flow depth $h = 15\text{ cm}$.

centripetal acceleration to form a secondary flow. Also, it provides the flow with a longer characteristic length to be developed. Therefore, it suggests that there exists a complex interaction between the momentum transferred by the moving lid and the pressure force imposed by the flow depth.

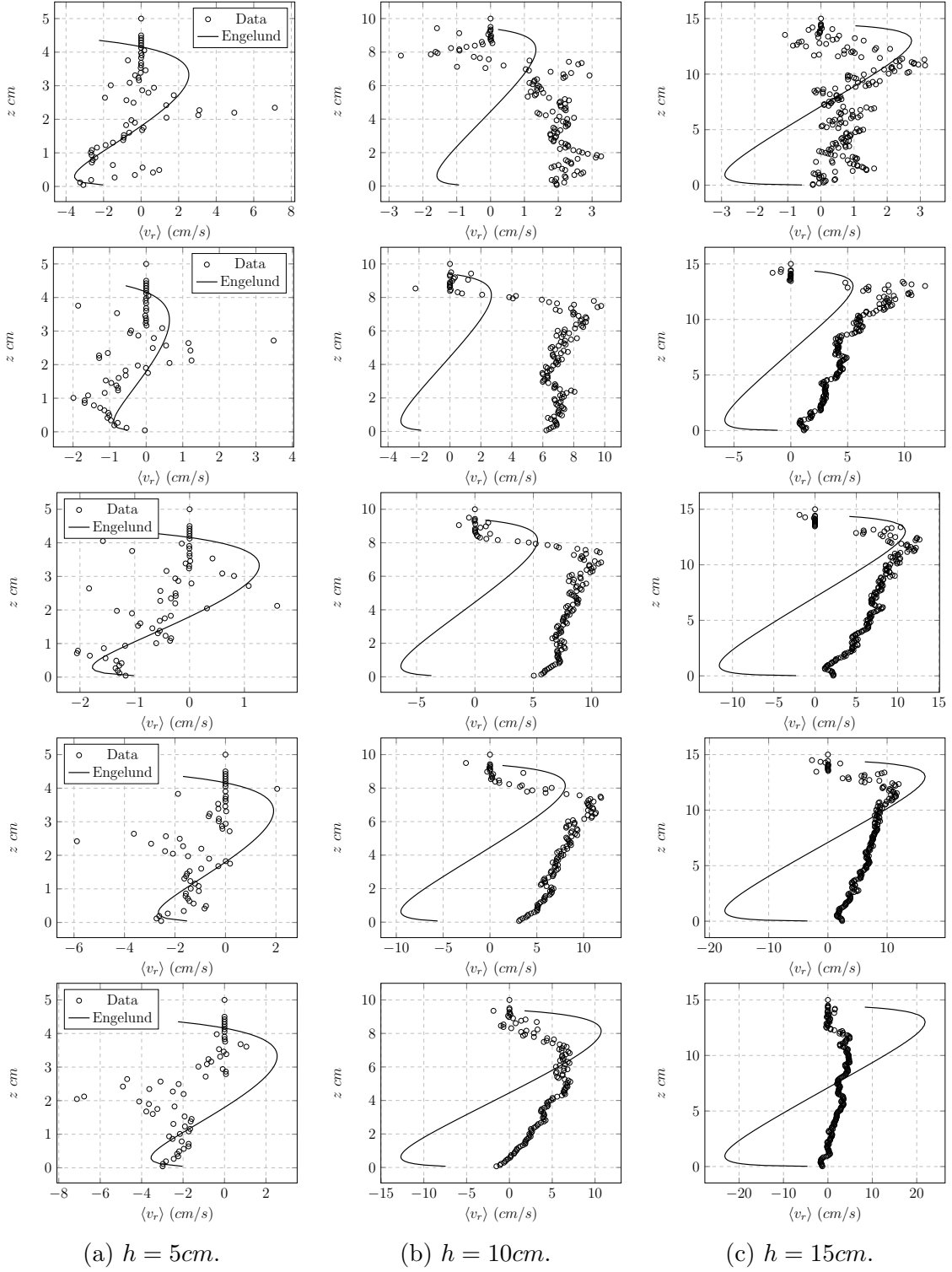


Figure 4.17: Modeled and measured radial velocity profiles for all flow conditions. Cases (flow depth) were organized by columns and lid rotation velocity were 0.5, 1, 2, 3, and 4rpm from top to bottom.

Chapter 5

Final Remarks

The purpose of this study was to assess the applicability of the Engelund's formulation in the tangential and radial flow of the Ven Te Chow Annular Flume. Therefore, radial and tangential velocity profiles were taken with an Ultrasound Velocity Profiler (UVP) and compared with those computed using the Engelund's formulation. It was intended to understand the hydraulic behavior of this facility at the University of Illinois Urbana-Champaign. Despite some similarities of the measured tangential profile with the computed using the Engelund's formulation, it was found that the formulation is not suitable for the Ven Te Chow Annular Flume. The strong curvature of the flume and the large depth-to-width ratio played a major role on defining the interaction of the secondary flow with the tangential velocity profile.

Engelund's formulation does not represent correctly the tangential and radial velocity profiles in the Ven Te Chow Annular Flume. The formulation has two important assumptions that are satisfied in this facility. First, the flow must be weakly curved in order to guarantee that the secondary flow does not interact significantly with the tangential flow. Falcon (1984) explains that strong curved channels convective terms of the momentum of governing radial equations becomes important and affects the tangential profile. In order to avoid a strong interaction between tangential and secondary flow, Falcon (1984) recommends that width-to-radius ratio must be significantly smaller than one. It was not the case for the Ven Te Chow Annular Flume. The width-to-radius became $B/R = 0.31$. On the other hand, Engelund's formulation holds that it is valid for wide channels. It means that the flow depth-to-width ratio must be significantly smaller than one. Three flow depth were assessed in this study: $5cm$, $10cm$, and $15cm$; such flow conditions yield depth-to-width ratios of

0.25, 0.5, and 0.75, respectively. Thus, the misrepresentation of the tangential and radial velocity profiles by the Engelund's formulation are attributed to geometry configurations of the flume. However, viscous effects could also be playing a role. Engelund's theory assumes that the flow is fully turbulent, and viscous effects are negligible.

Even though Engelund's formulation does not represent correctly the tangential profiles in the Ven Te Chow Annular Flume, it is notable some similarity with few measured cases. When flow depth was equal to 5cm , the measured the general structure of the modeled profiles slightly agreed with the measured data. Even though the depth-to-width ratio of this case was not significantly smaller than one, it yielded the smallest valued among all the assessed cases. It shows that Engelund's formulation potentially may represent tangential velocity profiles in laboratory facilities when its assumptions are considered in the experimental setup.

Engelund's formulation underestimated the shear velocity in all cases. All measured profiles followed a logarithmic distribution along the lower 3cm of the profile. Thus, shear velocities were estimated from measured data and compared with those computed with Engelund's formulation. It was found that the equations (tangential and radial) were sensitive to the value of shear stress. Therefore, the formulation underestimated the measured tangential profiles as well. Measured shear velocity increased with lid rotation velocity and flow depth. On the other hand, shear velocity estimated with the formulation increases with lid rotation but decreases with lid velocity rotation. Such differences were attributed to the interaction between the secondary flow and the tangential flow.

Furthermore, important distortion on the tangential velocity profile increased with flow depth. Since the secondary flow was more developed as the flow depth increased, its effect on the tangential profile became stronger with flow depth as well. For instance, the lower part of the $h = 15\text{cm}$ profiles presented a peak at the lower profile that was larger than the lid rotation velocity v_L . The maximum velocity of a typical Couette flow is located at the upper moving plate. Since the same peak was slightly perceived for flow depth equal to

10cm and no identified for flow depth of 5cm. It may be argued that the velocity structure of these profiles develop with the flow depth. Therefore, it suggested that convective velocities from the secondary flow may influence the tangential flow as the depth flow becomes larger. Also, it was found that measured shear velocity and depth-averaged mean velocity followed a family of power-law equations as function of flow depth.

Engelund's formulation did not represent the radial component of the flow because it assumes that the secondary flow covers completely the cross section. This assumption became possible when the curvature of the flow is weak and the cross section is sufficiently larger than the flow depth. Also, Engelund's formulation states that the net radial flow is zero. It means that the radially outward mass flux at near the lid is proportional to the inward flow at the bottom of the cross section. However, it was found outward and inward flow were not balanced in the measured radial velocities. In general, the positive velocity (outward flow near the lid) increased with flow depth. Studies like Krishnappan and Engel (2004) showed that at low rotation velocity of the tank the cell formed by the lid tends to be located asymmetrical to the outer part of the cross section. It may be argued that the center of the secondary cell was not located at the center of the cross section (where the transducers were placed) in all cases. The radial flow will encounter more resistance to convey water inwards proportionally to the flow depth (by means of the pressure force). It causes the center of the cell to be located at the outer part of the cross-section if the secondary flow is not strong enough to overcome the pressure force over the inner part of the cross section. Also, it was found that the radial velocity profiles increased with lid rotation velocity. Because centrifugal acceleration is proportional to the tangential velocity, it may be argued that a slower lid rotation velocity produces a weaker centrifugal acceleration. It was notable that velocity near the bottom became more negative (inward radial flow) proportionally with lid rotation velocity. It suggests that the secondary cell is capable of reaching further inwards into the flow as the lid velocity becomes faster. Therefore, it suggests that there exists a complex interaction between the momentum transferred by the moving lid and the pressure

force imposed by the flow depth.

Finally, this work can be extended into measurements of the secondary flow field in the radial and vertical direction considering part of the flow takes place through the bed. Future studies should be focused on measuring the secondary flow (radial and vertical velocity field) in the cross section of the Ven Te Chow Annular Flume. Optical techniques such as LDV measurements have been proven to be suitable tools to measure the secondary flow. Also, some effort should be put on characterizing experimentally the turbulence parameters in the Ven Te Chow Annular Flumes. Since this experimental setup used granular sediments to rise the bottom, UVP-DUO may be used to measure the continuity of the secondary flow into the porous media. UVP-DUO can be measured through a porous media as well as particles can move through the granular sediments.

References

- Amos, C., Bergamasco, A., Umgiesser, G., Cappucci, S., Cloutier, D., DeNat, L., ... Cristante, S. (2004). The stability of tidal flats in venice lagoonthe results of in-situ measurements using two benthic, annular flumes. *Journal of Marine Systems*, 51(1), 211–241.
- Amos, C., Daborn, G., Christian, H., Atkinson, A., & Robertson, A. (1992a). In situ erosion measurements on fine-grained sediments from the bay of fundy. *Marine Geology*, 108(2), 175–196.
- Amos, C., Grant, J., Daborn, G., & Black, K. (1992b). Sea carousela benthic, annular flume. *Estuarine, Coastal and Shelf Science*, 34(6), 557–577.
- Booij, R. (1994). *Measurements of the flow field in a rotating annular flume* (Tech. Rep.). TU Delft.
- Booij, R., Visser, P. J., & Melis, H. (1993). Laser doppler measurements in a rotating annular flume. In *Laser anemometry: Advances and applications–fifth international conference* (pp. 409–416).
- Briskin, B. J., Cantero, M. I., & Garcia, M. H. (2002). In-situ measurements of sediment oxygen demand by suspended biosolids. In *Hydraulic measurements and experimental methods* (pp. 1–10).
- Cantero, M., Mangini, S., Pedocchi, F., Nino, Y., & Garcia, M. (2004). *Analysis of flow characteristics in an annular flume: Implications for erosion and deposition of cohesive sediments*. ASCE.
- Cloutier, D., Hill, P. R., Amos, C. L., & Lee, K. (2003). Annular flume experiments on oil - mineral aggregates: an oil spill countermeasure on low energy shorelines. In *2nd international symposium on contaminated sediments: Characterization, evaluation, mitigation/restoration, management strategy performance*.
- Cloutier, D., LeCouturier, M. N., Amos, C. L., & Hill, P. R. (2006). The effects of suspended sediment concentration on turbulence in an annular flume. *Aquatic Ecology*, 40(4), 555–565.
- Cofalla, C., Hudjetz, S., Roger, S., Brinkmann, M., Frings, R., Wölz, J., ... others (2012). A combined hydraulic and toxicological approach to assess re-suspended sediments during simulated flood eventspart ii: an interdisciplinary experimental methodology. *Journal of Soils and Sediments*, 12(3), 429–442.
- Cofalla, C., Roger, S., Brinkmann, M., Hudjetz, S., Schüttrumpf, H., & Hollert, H. (2010).

- Floodsearch-hydrotoxic investigations of contaminated sediment in an annular flume. In *Proceedings of the piano mmx congress, liverpool*.
- Corney, R. K., Peakall, J., Parsons, D. R., Elliott, L., Amos, K. J., Best, J. L., ... Ingham, D. B. (2006). The orientation of helical flow in curved channels. *Sedimentology*, 53(2), 249–257.
- Engelund, F. (1975). Instability of flow in a curved alluvial channel. *J. Fluid Mech.*, 72(1), 145–160.
- Falcon, M. (1979). *Analysis of flow in alluvial channel bends*. (Unpublished doctoral dissertation). The University of Iowa.
- Falcon, M. (1984). Secondary flow in curved open channels. *Annual review of fluid mechanics*, 16(1), 179–193.
- Garcia, M. (2008). *Sedimentation engineering: Processes, measurements, modeling, and practice, chapter 2: Sediment transport and morphodynamics* (Tech. Rep.). American Society of Civil Engineers.
- Garcia, M. H. (1996). *Hidrodinamica ambiental*. Buenos Aires: Universidad Nacional del Litoral.
- Gibson, R., & Cook, A. (1974). The stability of curved channel flow. *The Quarterly Journal of Mechanics and Applied Mathematics*, 27(2), 149–160.
- Graham, D., James, P., Jones, T., Davies, J., & Delo, E. (1992). Measurement and prediction of surface shear stress in annular flume. *Journal of Hydraulic Engineering*, 118(9), 1270–1286.
- Hillebrand, G., & Olsen, N. R. B. (2010). Hydraulic characteristics of the open annular flume—experiment and numerical simulation. In *1st conference of the european section of the iahr, edinburgh, scotland*.
- Huang, J., Ge, X., & Wang, D. (2012a). Distribution of heavy metals in the water column, suspended particulate matters and the sediment under hydrodynamic conditions using an annular flume. *Journal of Environmental Sciences*, 24(12), 2051–2059.
- Huang, J., Ge, X., Yang, X., Zheng, B., & Wang, D. (2012b). Remobilization of heavy metals during the resuspension of liangshui river sediments using an annular flume. *Chinese Science Bulletin*, 57(27), 3567–3572.
- James, P., Jones, T., & Stewart, D. (1996). Numerical and experimental studies of annular flume flow. *Applied mathematical modelling*, 20(3), 225–231.
- Kantha, L., Phillips, O., & Azad, R. (1977). On turbulent entrainment at a stable density interface. *Journal of Fluid Mechanics*, 79(04), 753–768.
- Kato, H., & Phillips, O. (1969). On the penetration of a turbulent layer into stratified fluid. *Journal of Fluid Mechanics*, 37(04), 643–655.
- Kikkawa, H., Kitagawa, A., & Ikeda, S. (1976). Flow and bed topography in curved open channels. *Journal of the Hydraulics Division*, 102(9), 1327–1342.
- Krishnappan, B. G. (1993). Rotating circular flume. *Journal of Hydraulic Engineering*, 119(6), 758–767.
- Krishnappan, B. G., & Engel, P. (2004). Distribution of bed shear stress in rotating circular flume. *Journal of Hydraulic Engineering*, 130(4), 324–331.
- Kuenen, P. H. (1966). Experimental turbidite lamination in a circular flume. *The Journal of Geology*, 523–545.

- Maa, J.-Y., Wright, L., Lee, C.-H., & Shannon, T. (1993). Vims sea carousel: A field instrument for studying sediment transport. *Marine Geology*, 115(3), 271–287.
- Mehta, A. J., & Partheniades, E. (1982). Resuspension of deposited cohesive sediment beds. In *18th conference on coastal engineering* (pp. 1569–1588).
- Neumeier, U., Lucas, C. H., & Collins, M. (2006). Erodibility and erosion patterns of mudflat sediments investigated using an annular flume. *Aquatic Ecology*, 40(4), 543–554.
- Partheniades, E., Kennedy, J. F., Etter, R., & Hoyer, R. P. (1966). *Investigations of the depositional behavior of fine cohesive sediments in an annular rotating channel* (Tech. Rep.).
- Partheniades, E., & Mehta, A. J. (1971). *Deposition of fine sediments in turbulent flows* (Tech. Rep.).
- Pedocchi, F. M. (2005). *Evaluation of a laser diffraction instrument and an annular flume for cohesive sediment studies* (Unpublished master's thesis). University of Illinois - Urbana Champaign, Urbana, IL.
- Petersen, O., & Krishnappan, B. (1994). Measurement and analysis of flow characteristics in a rotating circular flume. *Journal of Hydraulic Research*, 32(4), 483–494.
- Pope, N., Widdows, J., & Brinsley, M. (2006). Estimation of bed shear stress using the turbulent kinetic energy approach: a comparison of annular flume and field data. *Continental Shelf Research*, 26(8), 959–970.
- Reichardt, H. (1959). *Gesetzmiissigkeitend er geradlinigen turbulenten couettestromung* (Tech. Rep.). Max-Planck-Inst. fur Stromungsforschung aerodynamischen Versuchsanstalt Gottingen.
- Rozovskii, I. (1957). Flow of water in bends of open channels acad. *Sci. Ukraine SSR*.
- Serway, R., & Jewett, J. W. J. (2014). *Physics for scientists and engineers* (Ninth ed.) [Print]. Belmont: Brooks/Cole.
- Sheng, Y. P. (1989). Consideration of flow in rotating annul for sediment erosion and deposition studies. *Journal of Coastal Research*, 207–216.
- Spork, V., Ruland, P., Schneider, B., & Rouvé, G. (1994). A new rotating annular flume for investigations on sediment transport. *International Journal of Sediment Research*, 9(3), 141–147.
- Spurk, J. H., & Aksel, N. (2008). *Fluid mechanics* (Second ed.) [Online]. Berlin: Springer-Link.
- Tait, S., Ashley, R., Verhoeven, R., Clemens, F., & Aanen, L. (2003). Sewer sediment transport studies using an environmentally controlled annular flume. *Water Science and Technology*, 47(4), 51–60.
- Te Slaa, S. (2012). *Calibration report annular flume: At the faculty of coastal engineering, zhejiang university* (Tech. Rep.). TU Delft-Section Hydraulic Engineering.
- Met-Flow SA. (2002). Uvp monitor model uvp-dup with software version 3: Users guide [Computer software manual].
- Villaret, C., & Paulic, M. (1986). Experiments on the erosion of deposited and placed cohesive sediments in an annular flume and a rocking flume. *Report to Coastal and Oceanographic Engineering Department, University of Florida, Gainesville*.
- Waterman, D., & Garcia, M. (2014). *Laboratory tests of oil-particle interactions in a freshwater riverine environment with cold lake blend weathered bitumen (draft)* (Tech. Rep.).

University of Illinois at Urbana-Champaign.

- Widdows, J., Brinsley, M., Bowley, N., & Barrett, C. (1998a). A benthic annular flume for in situ measurement of suspension feeding/biodeposition rates and erosion potential of intertidal cohesive sediments. *Estuarine, Coastal and Shelf Science*, 46(1), 27–38.
- Widdows, J., Brinsley, M. D., Salkeld, P. N., & Elliott, M. (1998b). Use of annular flumes to determine the influence of current velocity and bivalves on material flux at the sediment-water interface. *Estuaries*, 21(4), 552–559.
- Yang, Z., Baptista, A., & Darland, J. (2000). Numerical modeling of flow characteristics in a rotating annular flume. *Dynamics of Atmospheres and Oceans*, 31(1), 271–294.
- Yunwei, W., Qian, Y., & Shu, G. (2011). Relationship between bed shear stress and suspended sediment concentration: annular flume experiments. *International journal of sediment research*, 26(4), 513–523.